Mercury Telluride Nanowires for Topological Quantum Transport

Dissertation

zur Erlangung des naturwissenschaftlichen Doktorgrades
der Julius-Maximilians-Universität Würzburg

vorgelegt von

Jan Hajer

aus Traunstein

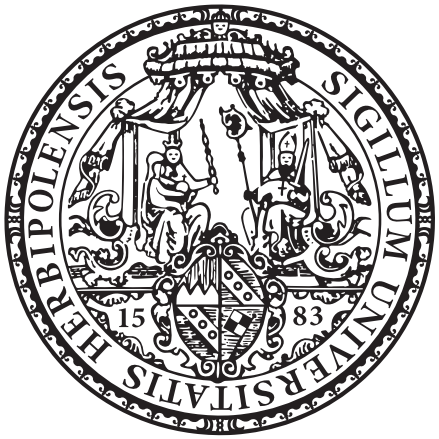

Würzburg, 2021

Eingereicht am: 26.07.2021
bei der Fakultät für Physik und Astronomie

1. Gutachter: Prof. Dr. Hartmut Buhmann
2. Gutachter: Prof. Dr. Friedrich Reinert
3. Gutachter: Prof. Dr. Erik P. A. M. Bakkers
der Dissertation

Vorsitzende(r): Prof. Dr. Haye Hinrichsen

1. Prüfer: Prof. Dr. Hartmut Buhmann
2. Prüfer: Prof. Dr. Friedrich Reinert
3. Prüfer: Prof. Dr. Giorgio Sangiovanni
im Promotionskolloquium

Tag des Promotionskolloquiums: 16.09.2022

Doktorurkunde ausgehändigt am:

Contents

Introduction

The stunning success story of nanotechnology began in December 1959 when R. P. Feynman sketched the extensive opportunities it might offer in his famous lecture "*There's Plenty of Room at the Bottom: An Invitation to Enter a New Field of Physics*". [1] Many remarkable technical achievements followed over the subsequent years and decades in areas such as thinfilm deposition, microscopy, and microlithography, [2,3] which contributed to achieve the miniaturization of engineered structures down to the nanoscale. This opened the avenue to design quantum systems where spatial confinement leads to the emergence of size effects. Quantum wells, quantum wires, and quantum dots – which are nanostructures created by confinement in one or more spatial dimensions – have since then become increasingly important and are nowadays a key ingredient of condensed matter physics. In these systems, the quantization of the electron energy becomes relevant, which affects the electrical and optical properties of matter in a fundamental way. [4]

The concept of topology is considered another central aspect of modern condensed matter physics. [5] In its broadest sense, topology discusses properties of an object that do not change continuously, the so–called topological invariants. An instructive geometrical example is the genus, i.e, the number of open holes through an object. In condensed matter physics, topology is utilized to study whether or not the Hamiltonians of two systems can be continuously transformed into each other. This allows to classify different topological phases of matter based on shared properties such as symmetries, which proved to be a particularly successful approach to explain the occurrence of phenomena beyond the basic quantum mechanical band theory of electric conduction. [6] A prominent representative is the topological insulator [7] – a bulk-insulating material that is topologically distinct from a conventional insulator by an inverted band order. The inverted band structure merges continuously into the conventional case at the interface to a trivial insulator or vacuum, which implies a band crossing and the associated formation of localized conductive states. These surface states inherit exciting nontrivial properties such as the helical locking of electron spin and momentum, as well as a linear energy dispersion close to the crossing point that resembles the solid-state realization of a massless Dirac fermion. [8]

This work is an experimental study placed in the intersection of these two conceptual fields. The goal is to create a reliable and flexible platform that allows to probe the electrical properties of a topological insulator nanowire. A quasi-one-dimensional topological insulator, compared to its three-dimensional counterpart, shows a quantization of the surface state spectrum along the perimeter, which opens a gap in the energy dispersion that periodically closes and reopens with the magnetic flux that is enclosed by the tubular surface state. [9] Combined with induced superconducting correlations, this peculiar modulation of the band structure has exciting potential application in the design of localized quasiparticle excitations that resemble Majorana fermions in a solid-state system. [10] Studying Majorana physics, i.e., the properties of particles that are their own antiparticle, is by itself a great prospect for basic research. Beyond that, Majorana bound states are regarded as a promising building block to achieve fault tolerant quantum computation – nowadays considered as one of the future key technologies. [11]

The central material system investigated in this work is mercury telluride, a prototypical three- [12] and two-dimensional [13] topological insulator with high-mobility surface states, which can be fabricated with high crystal quality and negligible bulk conductivity by molecular beam epitaxy. In order to realize the quasi-one-dimensional nanowire geometry, this work builds upon a preceding study [14] where the conceptual implementation was achieved by the epitaxial overgrowth of insulating CdTe nanowires, grown self-organized by the vapor–liquid–solid technique, [15] with a tubular layer of HgTe. This core–shell approach not only circumvents the impracticability of direct HgTe nanowire growth to achieve single crystalline free-standing structures, [16] but allows also to induce elastic strain into the HgTe lattice, [17] which is known to open an insulating bulk bandgap in the otherwise semimetallic three-dimensional HgTe. [18] Further, the bottom–up fabrication has the benefit of a typically higher crystal quality compared to a top–down process, where the ablation of material often causes damage in the remaining crystal. However, the narrow growth temperature window of CdTe nanowires with sufficiently high quality posed a severe limitation for optimization so far. [19] Here, the core–shell approach to HgTe nanowires is developed further. The main focus lies on the improvement of morphological and crystalline properties as well as the reliability of the growth process for the nanowire core in order to achieve a thorough optimization of the HgTe shell for charge transport studies. In addition, transport experiments in two key areas are discussed – the analysis of magnetoconductance oscillations as a manifestation of the quantum size effect, and the investigation of proximity superconductivity probing the effect of superconducting pairing induced into the electronic states of the HgTe nanowires.

This thesis is organized in seven chapters, which are grouped into two main parts. Part I focuses on nanowire growth, whereas Part II contains the chapters related to charge transport.

For the first part, a basic understanding of molecular beam epitaxy and its related areas is presumed as covered by standard textbooks. [20,21] On that basis, Chapter 1 introduces the main concepts specific to nanowire growth and summarizes the current state of research. Chapter 2 evaluates the potential of self-organized CdTe nanowires as the core for HgTe core–shell heterostructures. Temperature is the key parameter for the vapor–liquid–solid growth of CdTe nanowires; thus, an advanced thermometry technique based on the spectroscopic detection of thermal shifts in the absorption band edge of the substrate is adapted in order to enhance the control over the fabrication process. Despite the significant improvement in thermometry precision and the concomitant advances in growth, some of the envisaged quality improvements are still not reached. Hence, Chapter 3 explores ZnTe nanowire arrays as an alternative core material. For this purpose, a selective area growth process is developed that allows full control over the position and diameter of individual nanowires, which has not been reported before for II-VI materials aside from oxides. [22] A thorough investigation of the growth kinetics allows to study different growth regimes, which helps to optimize the nanowire morphology for radial overgrowth with a HgTe shell. CdTe is an ideal substrate for HgTe epitaxy due to its similar lattice constant. Hence, radial overgrowth of the ZnTe nanowires, the focus of Chapter 4, begins with a CdTe buffer that efficiently reduces the dislocation density at the interface to the HgTe. The subsequent HgTe shell shows a distinct nucleation behavior on the different types of side facets of the nanowire core, which is strongly affected by temperature. Fine-tuning the growth temperature thus allows to optimize the HgTe overgrowth. The morphology of the resulting nanowires is assessed by scanning electron microscopy. Further, a complementary transmission electron microscopy study is used to characterize the crystal quality and strain in the core–shell heterostructures.

Part II of this work characterizes the low-temperature charge transport through individual nanowires. The nanowire core, consisting of the widegap semiconductors ZnTe and CdTe, is insulating at cryogenic temperatures. Thus, charge transport takes place in the tubular HgTe shell. Generally speaking, the electrical conductivity of a material is governed by its band structure. Hence, Chapter 5 gives a brief introduction on how quantum size effects as a result of the quasi-one-dimensional nanowire geometry are expected to influence the typical band structure of a topological insulator, and summarizes the previous charge transport studies in HgTe-based core–shell nanowires. The experimental focus of Part II lies on two major topics: On the one hand, Chapter 6 addresses the concept of quantum size effects that emerge as quantum oscillations in the magnetoconductance. Aharonov–

Bohm oscillations, in particular, arise when magnetic flux is enclosed by a tubular electronic state in a clean sample with a low defect density and a large phase coherence length, which makes it a valuable indicator to assess the quality of the HgTe shell for charge transport. Beyond that, a more thorough investigation of the Aharonov–Bohm effect is conducted in order to gather a more detailed picture of the conductive modes that contribute to the magnetotransport. Chapter 7, on the other hand, studies charge transport with superconducting contact electrodes at millikelvin temperature. This allows to probe the effect of induced superconducting correlations in the system, which affects the voltage–current characteristic as well as the dynamic conductance of a direct current biased junction. From this, one can infer important characteristic quantities such as the critical current, the excess current and the superconducting energy gap. Further, the relation between the current and the superconducting phase drop across the junction is probed by the dynamic excitation with a microwave signal for signs of a contribution of the topological surface states. Overall, the charge transport experiments discussed in this part are intended as a basic characterization to advance the design of future studies of topological charge transport in the quasi–one–dimensional limit, which is now in reach due to the significant advances in the nanowire fabrication.

The main findings of Part I and II are recapitulated in an overview at the end of each part, and a comprehensive summary and outlook are given in the Conclusion.

Part I

Growth and structural characterization of HgTe-based core–shell nanowires

Chapter 1

Introduction to HgTe nanowire heterostructures

Nanowires are elongated one-dimensional nanostructures with material properties that are strongly influenced by quantum confinement. Over the recent years, the synthesis of nanowires advanced from fundamental materials science to an increasingly application-oriented versatile research platform. Despite the complex self-assembled growth from individual atoms or molecules, bottom–up fabrication techniques are successfully used to realize sophisticated nanowire heterostructures with an excellent crystal quality.

This chapter provides an introduction to the fabrication of nanowire heterostructures that contain the topological insulator HgTe. For this purpose, we highlight the fundamental differences of nanowire growth as compared to the more common fabrication of epitaxial thinfilms. Further, we discuss how the reduced dimensionality affects the elastic and plastic relaxation of lattice mismatch induced stress in nanowire heterostructures. Due to the low vapor pressure of Hg, the direct synthesis of HgTe nanowires is very challenging; thus, the state–of–the–art is the templated growth of tubular HgTe shells on CdTe nanowires reported in »M. Kessel, J. H. *et al.*, Phys. Rev. Materials **1**, 023401, (2017)«. *We review the status quo of this approach and discuss its advantages and disadvantages, as well as the main routes towards improving the quality of the nanowires for the charge transport investigation presented in Part II of this work.*

1.1 Nanowire synthesis by the vapor–liquid–solid technique

Epitaxial growth techniques have gained widespread use in the fabrication of semiconductor thinfilms not only for research purposes but increasingly also for industrial applications. [21] Among these, molecular beam epitaxy (MBE) delivers an outstanding degree of control over the growth conditions, especially with respect to the crystal quality and doping. [20] The focus of this thesis lies on the growth of HgTe nanowires for charge transport investigation. Defects in the crystal lattice as well as unintended background doping can significantly impair the transport characteristics, thus MBE is the ideal technique to fabricate the nanowires with the desired high crystal quality.

Molecular beam epitaxy relies on the interplay of adsorption, diffusion, incorporation and desorption of adatoms on the surface of a substrate crystal as sketched in Fig. 1.1. [20] The most important parameter to tune the kinetics of the surface processes is the substrate temperature, which has to be controlled precisely in order to achieve defect-free single crystalline growth. In order to minimize the impurity doping, the background pressure of the process chamber is kept as low as possible. The required ultra-high vacuum conditions result in a large mean free path in the vapor phase leading to a beam-like propagation of the material flux. The setup of a typical MBE chamber as well as the adaptations required for the growth of Hg-containing materials are described, e.g., by P. Leubner and C. Ames. [23, 24]

Bottom-up synthesis of nanowires has first been reported by R. S. Wagner and W. C. Ellis in 1964, [15] who found that Au droplets can catalyze the vertical growth of Si nanowires and referred to this as the vapor–liquid–solid (VLS) process. Since then a variety of refinements of this fundamental growth technique has been demonstrated, including, i.a., the self-catalyzed growth seeded by liquid droplets of one of the supplied materials [25, 26] and the vapor–solid–solid (VSS) mechanism based on solid instead of liquid particles as growth catalyst. [27, 28] However, the high versatility of the VLS technique makes it still one of the most successful and widely used methods.

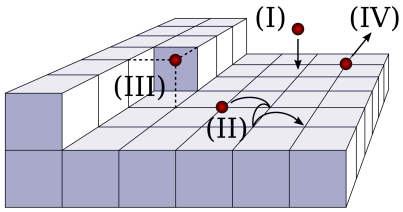

Figure 1.1: Illustration of adatom (red dots) processes on a crystal lattice (grid) during molecular beam epitaxy: (I) adsorption, (II) diffusion, (III) incorporation and (IV) desorption.

Generally, nanowire growth is achieved by a locally enhanced nucleation probability. For this purpose, the VLS method uses liquid metallic droplets distributed over the substrate surface. The substrate temperature is chosen significantly higher compared to thinfilm epitaxy in order to suppress crystal growth on the bare substrate surface and to enhance adatom diffusion. The droplets collect the diffusing material supplied from the vapor phase and direct it to the growth front at the liquid–solid interface as schematically depicted in Fig. 1.2: The liquid phase of the droplets and their three-dimensional shape result in an efficient accumulation of adsorbates even at high substrate temperature [Fig. 1.2(a)]. If the growth parameters are adjusted correctly, the material concentration in the droplets increases until the solubility limit is reached and stable nucleae form spontaneously [Fig. 1.2(b)]. For most material systems, this occurs at the triple phase boundary between vapor, droplet and crystal where the nucleation energy is typically the lowest. [29,30] The step edge of the nucleus is the preferred condensation point for further crystallization of material dissolved in the droplet, which results in the formation of a monolayer on the crystal surface [Fig. 1.2(c)]. Once the monolayer covers the entire liquid–solid interface the process repeats, and a nanowire grows with a diameter defined by the droplet size [Fig. 1.2(d)].

This fundamental growth technique can be applied to a wide range of material systems. The combination of different materials further allows to fabricate nanowire heterostructures with an enhanced functionality. Due to the reduced lateral size of the quasi-one-dimensional geometry, lattice mismatch in crystalline nanowire heterostructures is distributed differently compared to thinfilm heterostructures. Thus, the basics of strain in axial and radial nanowire heterostructures is discussed in the following. Then, we summarize the status of research at the beginning of this work on the bottom-up synthesis of HgTe nanowires, a material system that comes with significant challenges for the bottom–up synthesis by the VLS method. At the end of this chapter we evaluate the current approach, which is the radial overgrowth of VLS-grown CdTe nanowires with HgTe, in order to point out approaches for improvement and to set the focus of this growth study.

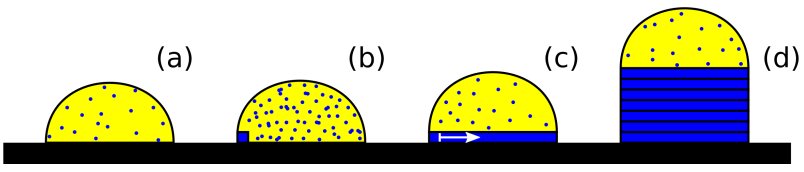

Figure 1.2: Schematic stages of VLS growth: (a) droplets (yellow) accumulate material (dots), (b) spontaneous nucleation (blue) at the triple phase line, (c) completion of a monolayer and further material accumulation. (d) A nanowire forms below the droplet.

1.2 Lattice mismatch in nanowire heterostructures

The combination of differently composed epilayers allows to tailor the electronic band structure of a heterostructure in order to tune its electrical and optical properties. However, mismatch of the crystal lattices at a heterointerface can give rise to an elastic relaxation by strain, and a plastic relaxation via lattice defects and dislocations, and can thus be seen as the most severe limitation of heteroepitaxy. While strain in some cases can be utilized to influence and enhance the properties of a semiconductor in a controlled way, plastic relaxation is typically not intended as it gives rise to interface defects which can propagate far into the crystal and alter the local electronic band structure. This often leads to a degradation of electrical and optical properties. In thinfilms, the quasi-infinite geometry in the substrate plane allows for an elastic relaxation of lattice mismatch only along the direction perpendicular to the substrate surface. Reducing the in-plane dimensionality of the crystal opens up the possibility of elastic relaxation also in the lateral direction. Especially efficient defect-free heteroepitaxy can be achieved in nanowires with a large aspect ratio, where a small diameter of several tens to few hundreds of nanometers ensures a small footprint on the substrate. [31] In the following, we discuss how the nanowire geometry helps to accommodate for lattice mismatch that can originate both from the substrate (axial mismatch) and from shell overgrowth (radial mismatch).

Nanowires on lattice mismatched substrates

Strain in free-standing nanowires can be efficiently released in the lateral direction. Depending on their diameter, nanowires of arbitrary length can be grown without the formation of misfit dislocations at the interface to a lattice mismatched substrate. F. Glas [32] provided a formalism to calculate the critical radius of an axial nanowire heterostructure consisting of two lattice mismatched segments of the same diameter and semi-infinite length: Comparing the elastic energy of the dislocation-free heterointerface with the energy of the system at the onset of plastic relaxation, one can derive an implicit equation for the critical nanowire radius r_c

$$\frac{2\pi}{A}\left(\frac{\alpha^2 b_\mathrm{eff}^2}{4} - \alpha b_\mathrm{eff}\varepsilon_0 r_\mathrm{c}\right) + C\left(\ln\left(\frac{\beta r_\mathrm{c}}{b}\right) + 1\right) = 0. \quad [32] \tag{1.1}$$

Here, ε_0 denotes the relative difference of the lattice parameter (i.e., the lattice mismatch), and $\alpha = 4/\pi$, $\beta = 2/\pi$ are geometrical coefficients. The factor A considers the geometry of the system with a value of 27.4 to describe a cylindrical axial heterostructure and 15.0 in case of a nanowire on top of a rigid semi-infinite substrate plane. [31] The coefficient $C = (1-\nu\cos^2\theta)b^2/[2\pi(1+\nu)]$ with the Poisson ratio $\nu = 1/3$ and b taken as the core cutoff radius for the calculation of the elastic energy. Under the assumption of strain release via

60° dislocations, the angle θ between the dislocation line and its Burgers vector is $\pi/3$ and the edge component of the Burgers vector $b_{\text{eff}} = b/2$. [31]

Following the evaluation of the critical dimensions by V. G. Dubrovskii [31] we compare experimental data from VLS-grown III-V nanowires on different lattice mismatched substrates with the theoretical description given by Eq. 1.1. Figure 1.3 summarizes the results. The black and red data points in Fig. 1.3 represent the critical radius obtained for nanowires grown by MBE [33] and metalorganic chemical vapor deposition (MOCVD), [34] respectively. Despite of the fundamentally different growth techniques the experimental results correspond well. This indicates, that the critical radius is mostly determined by general energetic aspects rather than the growth kinetics, which are likely to be quite different for MBE and MOCVD. Thus, it is likely that from these results conclusions can be drawn also for the II-VI semiconductors which are discussed in the following chapters. To do so, we use Eq. 1.1 to model the experimental data. Taking $A = 15$ and $b = 1.0\,\text{nm}$, we derive a relation between r_c and ε_0 that fits the data well (blue curve in Fig. 1.3). The blue-shaded area below the curve indicates the parameter range where dislocation-free growth is expected, while above plastic relaxation sets in.

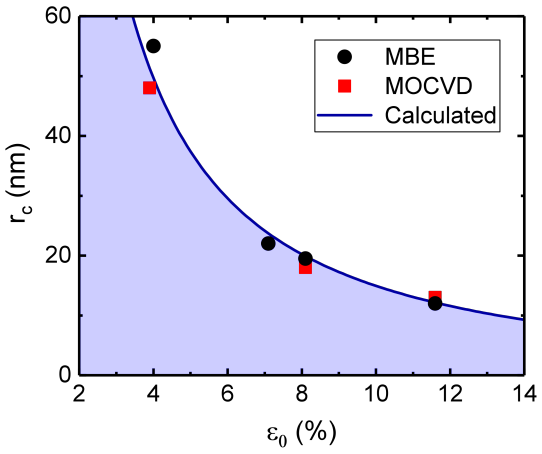

Figure 1.3: Critical nanowire radius r_c for the dislocation-free growth of nanowires depending on the lattice mismatch ε_0 to the substrate. The data points are experimentally determined values from MBE- (black circles) [33] and MOCVD-grown III-V nanowires (red squares) [34]. The solid line is a fit to the data computed from Eq. 1.1. The blue-shaded area indicates the parameter range where growth is expected to be free of misfit dislocations.

Radial nanowire heterostructures

Overgrowth of nanowires with an epitaxial layer allows to fabricate radial core–shell heterostructures. For these, a significantly enhanced critical shell thickness for coherent growth is observed compared to the case of planar thinfilm growth. [35] In order to understand the enhanced elastic relaxation of stress, we qualitatively discuss in the following the fundamental difference between planar thinfilm heterostructures and the core–shell geometry as sketched in Fig. 1.4.

First, we consider a planar thinfilm grown onto a semi-infinite substrate. In this case, an elastic relaxation of lattice mismatch can only occur in the direction perpendicular to the substrate surface [cf. red arrow in Fig. 1.4(a)], whereas the in-plane lattice constant has to be matched. The elastic energy in the system scales thereby linearly with the epilayer thickness h. As a consequence, the total amount of strain in the system accumulates with increasing h, which implies that above a certain critical epilayer thickness the energy barrier to plastic relaxation would always be crossed. This is entirely different in the cylindrical core–shell geometry. There, a tangential displacement [cf. black arrow in Fig. 1.4(b)] can occur along with a radial displacement (red arrow) in a way that both accommodate for lattice mismatch, contrary to the planar case where the lateral lattice constant is fixed by the substrate.

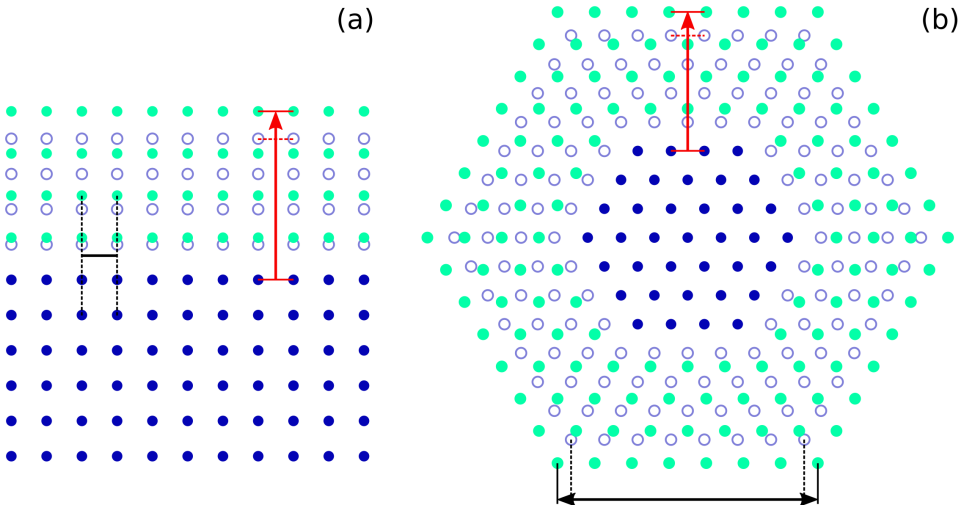

Figure 1.4: Qualitative comparison of in-plane/tangential (black arrows) and out-of-plane/radial displacement (red arrows) in (a) planar thinfilms and (b) core–shell heterostructures. Blue and turquoise filled dots represent lattices with a smaller and larger lattice constant, respectively. Empty dots indicate the continuation of the blue lattice. For simplicity, the substrate (blue dots) is assumed to be entirely rigid in both cases.

This schematically explains the high efficiency of elastic strain relaxation in core–shell nanowires. From a theoretical analysis of the displacement field in the cylindrical core–shell geometry one can derive an elastic stress relaxation that scales with $1/h^2$. [31] Further, the total elastic energy saturates for large shell thickness with an asymptotic value that depends on the thickness of the core nanowire r_c and on the lattice mismatch ε_0 between core and shell, which might be smaller or larger than the energy of a dislocated interface. This leads to the existence of a critical set of parameters for ε_0 and r_c below which plastic relaxation is fully suppressed for arbitrarily large shell thickness. The elastic stress is mostly localized near the interface and is already significantly reduced when the shell thickness reaches the order of the core radius. [31] This is particularly important later on for the discussion of strain effects in the HgTe-based core–shell nanowires.

1.3 CdTe–HgTe core–shell nanowires – a review of the status quo

The MBE growth of HgTe is challenged by the relatively low typical growth temperatures ($\lesssim 200\,^{\circ}\mathrm{C}$) and a high re–evaporation rate of Hg. This prevents the growth of HgTe nanowires by a metal-catalyzed VLS or VSS process. Further, for thinfilm growth it was shown that especially on the Te-terminated (111)B surface – the typical growth facet for most compound semiconductor nanowires [36] – an oversaturation with Hg quickly suppresses the nucleation of HgTe, [37] which poses significant challenges also for the self-catalyzed nanowire growth. Experimental efforts based on the preferred condensation of Hg at spots with an enhanced surface roughness were reported, however the obtained HgTe nanowires did not show an epitaxial relation to the substrate and were polycrystalline [38] or included segments of pure Te. [16]

Thus, the fabrication of core–shell heterostructures was investigated as an alternative approach towards a quasi-one-dimensional realization of the topological insulator HgTe. [14] Not only allows the templated growth of HgTe onto a nanowire of different material to resort on the reliable VLS mechanism, but it also opens the possibility to influence the electronic band structure of the heterostructure in a desired way. The HgTe nanowires are intended for charge transport investigations, thus it is important that the nanowire core is insulating at cryogenic temperatures, which is the case for many II-VI compounds. Further, even though the core–shell geometry provides an efficient elastic relaxation of strain (cf. Section 1.2), a large lattice mismatch should be avoided in order to allow dislocation-free epitaxial overgrowth. HgTe thinfilms can be grown with a high crystal quality on CdTe substrate. [39] There, the relative lattice mismatch of 0.3% results in a critical epilayer thickness of around 140 nm [23, 40] which can be safely assumed to be significantly larger in the core–shell geometry. Strain is known to open a bulk bandgap in HgTe. [12, 41] Thus, charge transport in strained three-dimensional HgTe at cryogenic temperature is governed by the topological surface states. This makes CdTe nanowires a promising template for HgTe shell overgrowth.

Based on pioneering work on the MBE growth of group II telluride nanowires at the Polish Academy of Sciences in the 2000s, [42–44] a growth method for the self-organized fabrication of CdTe nanowires on ZnTe stubs was developed by M. Kessel *et al.* [19] The nanowires are seeded from self-organized liquid Au–Ga droplets by the vapor–liquid–solid mechanism discussed in Section 1.1. The main challenge for the VLS-growth of CdTe nanowires is the extraordinarily narrow temperature window for long and straight single crystalline growth, which requires a more precise temperature control than provided by the standard thermocouple that measures the temperature of the backside of the sample mount. Inferring the correct substrate temperature from the emergence of nanowire-specific facets in the reflection

high-energy electron diffraction (RHEED) pattern increases the reliability of growth to a large extent, which allowed to investigate the basic growth conditions for the CdTe nanowires. [19] The nanowires obtained were subsequently overgrown with a HgTe shell. A crystallographic characterization of the core–shell nanowire ensembles with electron and X-ray diffraction techniques suggests an overall high crystal quality of the nanowire ensemble, an epitaxial relation to the substrate and residual strain in the heterostructures. [17]

A novel growth method for CdTe–HgTe core–shell nanowires

In the following, we summarize the key points in the state–of–the–art growth process for the fabrication of CdTe–HgTe core–shell nanowires, which is described in detail by M. Kessel and J. H. [14,45] We use Si-doped GaAs wafers as substrate for the nanowire growth process that is schematically depicted in Fig. 1.5. The typical growth direction of most zinc blende compound semiconductor nanowires is [111]B; [36] thus, a (111)B surface orientation is typically chosen to achieve nanowire growth perpendicular to the substrate surface, which is especially important for subsequent overgrowth with a shell that covers all sides of the nanowire homogeneously. Other surface orientations such as (110) or (001) provide one or more ⟨111⟩B directions that are tilted with respect to the substrate normal, which can be utilized for the fabrication of semi-shells covering only one side facet of the nanowires, [19] or for nanowire crossings. [46]

The substrate is glued with liquid In onto a molybdenum sample holder and loaded into the ultra-high vacuum cluster, which connects, amongst others, a metal deposition chamber and three separate growth chambers for the molecular beam epitaxy of III-V semiconductors, widegap II-VI compounds, and Hg-containing II-VI materials. The native oxide is thermally removed in the III-V chamber, followed by the deposition of 1 nm of Au [Fig. 1.5(a)]. Heating the substrate to 450–480 °C in the widegap II-VI chamber induces the thermally activated solid state diffusion of Ga from the GaAs substrate into the Au, which results in the dewetting of the Au layer into

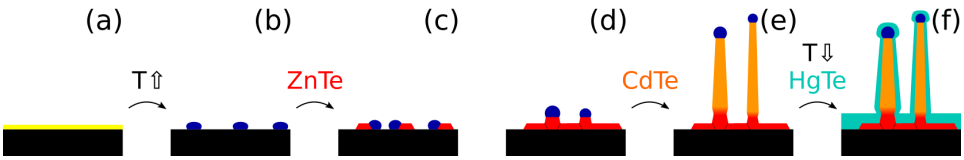

Figure 1.5: Schematic process steps of the growth procedure for CdTe–HgTe core–shell nanowires: (a) Au deposition, (b) dewetting at an elevated temperature, (c) ZnTe nucleation, (d) lateral redistribution, (e) axial CdTe growth, and (f) radial HgTe overgrowth at a reduced substrate temperature.

liquid eutectic Au–Ga droplets [Fig. 1.5(b)]. These liquid metallic droplets have a relatively low melting point of about 350 °C and are subsequently used to seed the nanowire growth.

Nanowire growth starts with the synthesis of short ZnTe stubs. Therefore the substrate temperature is set to 400 °C, and material fluxes of Zn and Te are supplied with a Zn : Te ratio of 0.6 at beam equivalent pressures in the range of 1–2 $\times$ 10^{-6} mbar. The Au–Ga droplets catalyze the formation of ZnTe structures, which initially grow parallel to the substrate surface resulting in a lateral relocalization of the droplets [Fig. 1.5(c)]. This can possibly be explained by the large lattice mismatch of 7.6% [47] between ZnTe and GaAs, for which one can infer from Fig. 1.3 (Section 1.2) an estimated critical nanowire radius for dislocation-free growth of only about 20 nm. Within few minutes of growth, the laterally moving droplets eventually merge and get localized by the ZnTe structures. Once the lateral direction is blocked, growth continues in the vertical [111]B direction [Fig. 1.5(d)]. At this point (after $\sim$ 2 min), the Zn flux is replaced with Cd at a Cd : Te ratio of 1.2. At 400 °C, the VLS growth of CdTe is fully suppressed. The substrate temperature is then slowly reduced while the surface morphology is monitored by RHEED until a slight change in the diffraction pattern – the beginning of a broadening of the diffraction spots parallel to the substrate surface – indicates that CdTe nanowire growth has begun. In order to maintain optimal conditions at the growth front, the substrate temperature has to be continuously increased with a non-monotonic temperature ramp that has to be empirically deduced from previous growth runs. Over a growth time of 6–8 h, straight and free-standing CdTe nanowires with a length of about 2 µm can be achieved [Fig. 1.5(e)]. However, a slight deviation from the correct substrate temperature by only few degrees Celsius towards higher temperature already results in the suppression of growth, or in the formation of kinks towards lower. This makes the substrate temperature the most crucial parameter for successful CdTe nanowire growth.

Subsequently, the CdTe nanowires are overgrown with an epitaxial HgTe shell [Fig. 1.5(f)]. The sample is therefore transferred to the Hg-containing MBE chamber and heated to a substrate temperature of 185 °C. At this temperature, nucleation can occur on the entire substrate while the adatom diffusion length is still sufficiently high as required for single crystalline MBE overgrowth. Due to its low condensation coefficient, the Hg flux has to be supplied with a relatively high beam equivalent pressure of about 4×10^{-4} mbar. Overgrowth with a closed shell on all nanowire sides was achieved with a Hg : Te ratio of 200.

Structural properties of the CdTe–HgTe core–shell nanowires and starting point for the following investigation

The morphology and crystal structure of the core–shell nanowires obtained by this growth technique was investigated by scanning electron microscopy (SEM) as well as by electron and X-ray diffraction. In the following, we summarize the key aspects from the structural analysis presented in Refs. [14,17,19]. Based on these findings we set out possible approaches for improvement, which are covered later on in this work.

Figure 1.6 shows electron micrographs of a successfully grown ensemble of CdTe–HgTe core–shell nanowires obtained by the RHEED-controlled growth method. The extensive application of RHEED for the VLS growth of CdTe nanowires made it possible to achieve nanowires with sufficient quality to employ them as substrate for epitaxial HgTe overgrowth. However, maintaining the correct thermal conditions at the growth front throughout the entire process is extremely challenging, because changes in the nanowire morphology large enough to be observable in the RHEED pattern have often already altered the growth irreversibly. Thus, the implementation of a more precise thermometry technique which gives a direct feedback of the substrate temperature during growth is the first important aspect in order to increase the reliability and reproducibility of CdTe nanowire synthesis.

The second aspect is the geometrical morphology of the nanowire core. In general, the nanowires shown in Fig. 1.6 appear uniform but with a clear variation in shape and length that is likely a result of the self-organized formation and the subsequent lateral redistribution of the growth seeds. Both effects contribute to a variation in the Au–Ga droplet size, which affects not only the nanowire diameter but also the axial growth rate. On average, the CdTe nanowires reach lengths of about 2 µm and have a diameter ranging from ~ 50 nm in the upper part to ~ 200 nm close to the base. While the

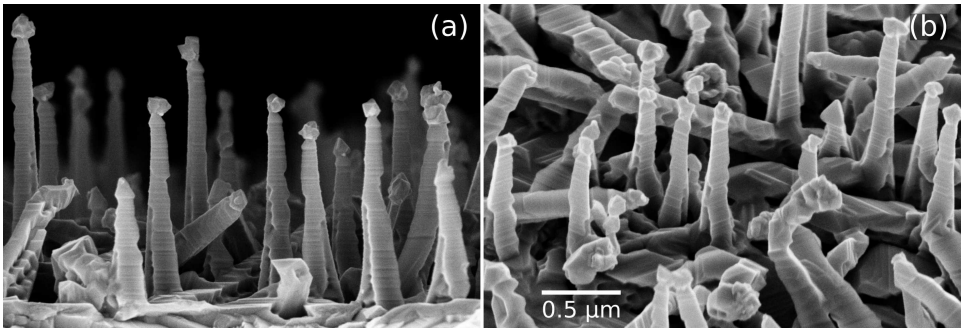

Figure 1.6: Electron micrographs of CdTe–HgTe core–shell nanowires under a viewing angle of (a) 90° and (b) 45° from the substrate normal, taken from M. Kessel. [14]

nanowire length is sufficient for the integration into electrical circuits, the diameter variation due to the tapered shape can obscure the observation of quantum size effects that depend on the nanowire cross-section. It is thus important to explore methods in order to achieve core nanowires with a constant diameter over the entire length as a template for an untapered tubular HgTe shell.

The third major aspect for improvement concerns the HgTe shell. It can be seen from the electron micrographs shown in Fig. 1.6 that the nanowire sides are stepped. The formation of these pronounced "scales" can be explained by the preferred formation of microscopic stable $\{11\bar{1}\}$A facets on the $\{11\bar{2}\}$A sides of the CdTe core. [14] Further, most nanowires exhibit gaps in the HgTe shell on the B-terminated side facets, especially close to the base. Thus, the growth conditions for HgTe on the side facets of a CdTe nanowire need to be optimized. Finding the ideal growth parameters, however, relies on a reliable and reproducible fabrication of core nanowires.

Chapter 2

Self-organized CdTe nanowires

CdTe–HgTe core–shell nanowires offer the possibility to investigate charge transport through HgTe in a tubular quasi-one-dimensional geometry. It turns out that the exceptionally narrow temperature window for the VLS-growth of long and straight CdTe nanowires is the main obstacle during fabrication of these heterostructures. Thus, the research presented in this chapter focuses on improving the reliability of CdTe nanowire growth. A well controlled growth process for the nanowire core is not only beneficial per se*, but impacts also the quality of the HgTe shell because an efficient and precise optimization of radial overgrowth is only feasible with a consistent quality of the core.*

A precise contactless measurement of the substrate temperature during MBE growth can be achieved by optical thermometry. In contrast to the most common optical temperature sensors that detect the thermal emission of radiation from a sample, thermometry based on the temperature dependent change of the band edge absorption spectrum allows to determine the substrate temperature of a semiconductor substrate even at low temperatures. This makes band edge thermometry a promising technique to improve the VLS growth of CdTe nanowires.

In this chapter, we first implement band edge thermometry to the growth of CdTe nanowires and discuss its advantages over the commonly used thermocouple. Its precision and reliability make it an important basis also for further growth developments presented in subsequent chapters. This is followed by a structural study to investigate the morphological properties of the resulting CdTe nanowires on a macroscopic scale as well as their crystal structure. Parts of this chapter are published in »R. Schlereth, J. H. *et al.*, J. Cryst. Growth **537**, 125602, (2020)«.

2.1 Improving growth with band edge thermometry

Temperature can be measured based on a variety of physical effects. One of the most widely used temperature sensors is the thermocouple, where a thermovoltage is measured across a junction between two different conductors. A reliable temperature feedback requires good and reproducible physical contact between thermocouple and the sample, which can be difficult to achieve especially in MBE systems with a rotating sample holder. Contactless optical thermometry is less sensitive to the thermal coupling of the sample, which makes it in principle better suited for temperature sensitive processes. However, most optical techniques such as pyrometry and blackbody thermometry measure the thermal emission of the sample. The total amount of emitted radiation – described by the Stefan-Boltzmann equation – increases steeply ($\propto T^4$) with temperature T; hence, emission-based thermometry techniques have a low efficiency at the relatively low typical growth temperatures of compounds in the (Hg,Cd,Zn)Te material system.

The Au-catalyzed MBE growth of CdTe nanowires requires thermometry with a high accuracy and reliability due to the very narrow growth temperature window. The substrate temperature has so far been measured by a thermocouple pressed at the backside of the rotating sample holder as sketched on the lefthand side of Fig. 2.1(a). For CdTe nanowires grown with this thermometry technique we observe that the thermocouple signal has to be continuously increased in order to maintain optimal conditions for

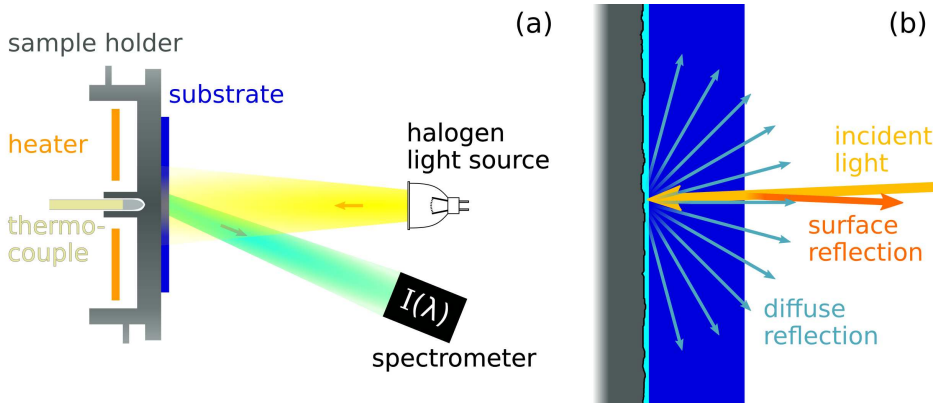

Figure 2.1: (a) Schematic band edge thermometry setup. The band edge signal is obtained with both the light source and the spectrometer facing the sample surface, and the thermocouple is placed close to the substrate heater at the backside of the rotating sample holder. (b) Illustration of direct reflection of incident light at the sample surface and diffuse reflection at the rough interface to the sample holder.

wire growth. [19] Also, the absolute growth temperature varies from sample to sample by several Kelvin. Further inconsistencies between thermocouple measurement and the apparent temperature at the growth front are reported by R. Schlereth *et al.* [48,49] for the growth of (Hg,Cd)Te thinfilms. These observations all together suggest that for materials with a very narrow growth temperature window the temperature at the substrate surface is not sufficiently well represented by a backside thermocouple measurement. Hence, we explore in the following band edge thermometry as a method to improve the reliability and reproducibility of CdTe VLS-MBE, a contactless technique that utilizes the temperature dependence of the absorption band edge of a semiconductor for thermometry rather than the thermal emission and thus is feasible also for low temperatures.

Band edge thermometry

The energy gap E_g of a semiconductor depends on its temperature and can be approximated for many materials by the Varshni equation [50]

$$E_g(T) = E_0 - \frac{\alpha T^2}{T + \beta}. \tag{2.1}$$

The gap energy E_0 at $T = 0\,\mathrm{K}$ and the material specific constants α and β are well known for most materials. For pure GaAs, e.g., E_g decreases with increasing temperature as pointed out by the black curve in Fig. 2.2. Photons

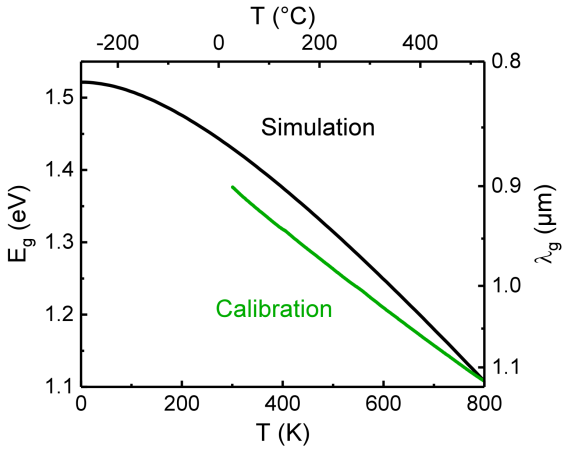

Figure 2.2: Temperature dependence of the energy gap of GaAs. The black curve is simulated with Equation 2.1 using the material parameters $E_0 = 1.5216\,\mathrm{eV}$, $\alpha = 8.871 \times 10^{-4}\,\mathrm{eV/K}$, and $\beta = 572\,\mathrm{K}$. [50] The green curve is the the calibration used for the calculation of the substrate temperature from the band edge fit, provided by k-Space Associates, Inc.

with a wavelength λ corresponding to an energy value larger than the band gap can be absorbed in the semiconductor. This results in a distinct edge in the absorption spectrum which lies typically in the visible or near-infrared range. [51] Exemplary absorption spectra for GaAs at different temperatures are shown in Fig. 2.3. Hence, spectroscopy of the band edge wavelength can be used as a signal for monitoring the temperature of a semiconductor. It combines the advantages of a contactless optical measurement with the high sensitivity even at low growth temperatures. However, doping affects the size of the band gap. [52] Thus, band edge based thermometry requires calibration to compensate the influence of substrate doping, which can lead to a deviation from the expected dependence (cf. green curve in Fig. 2.2). A high reproducibility can be achieved with a low sample-to-sample variation of the substrate doping concentration, which is typically fulfilled for wafers cut from the same ingot. Band edge thermometry has already been successfully implemented for the growth of, e.g., GaN on SiC, [53] low-temperature GaAs, [54] and CdTe thin films. [55] In the following we investigate whether it is beneficial also for the growth of CdTe nanowires.

The geometry of the used measurement setup (»kSA BandiT« from k-Space Associates, Inc.) is sketched in Fig. 2.1(a). Both light source and spectrometer are facing the front of the sample while the thermocouple is pressed to the backside of the molybdenum sample holder. Direct heat transfer from the heater to the thermocouple is reduced by a shielding around the measurement spot, thus the measured signal T_{TC} is mostly governed by the temperature of the sample holder. The band edge signal T_{BE} detected by the spectrometer consists mostly of light that traverses the sample and is

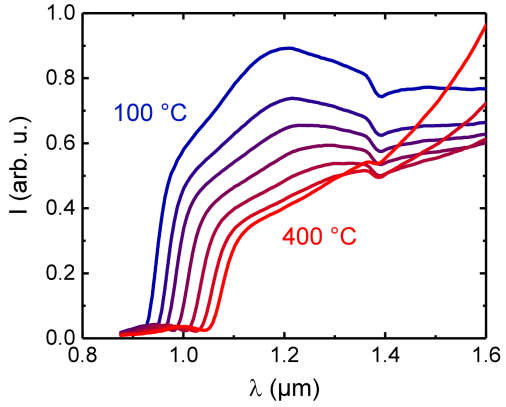

Figure 2.3: Absorption spectrum of a Si-doped (111)B GaAs wafer at substrate temperatures in the range of 100 °C (blue) to 400 °C (red) in steps of 50 °C.

reflected diffusively at the rough interface between sample and sample holder [cf. Fig. 2.1(b)]. Thus, T_{BE} resembles the average absorption spectrum across the entire sample height. The spectrometer is positioned off-axis in order to avoid the detection of light that is reflected back directly from the substrate surface, which carries no information about the band edge and thus only increases the background signal. However, strong surface roughness can cause direct reflection in random directions already from the sample surface. This can gradually reduce the reliability of the band edge signal, especially during the growth of nanowires.

Application to the growth of CdTe nanowires

In the following, we test if band edge thermometry is suited to improve the state–of–the–art fabrication process of CdTe nanowires described in Chapter 1. Figure 2.4 depicts the growth sequence that has been optimized for straight and vertical nanowire growth: First, ZnTe stubs are grown at $T_{\mathrm{TC}} = 420\,^{\circ}\mathrm{C}$ for about 2 min (I). In a second step, Zn flux is replaced by Cd and the

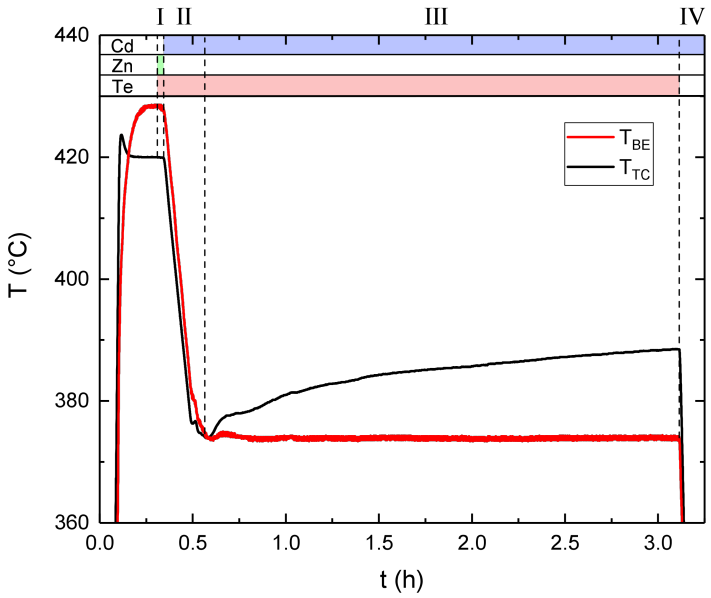

Figure 2.4: Comparison of T_{BE} and T_{TC} during the growth of CdTe nanowires. Horizontal bars represent the material supply. Roman numbers indicate the different growth steps: (I) ZnTe stubs; (II) cooldown in Cd and Te flux; (III) CdTe nanowires; (IV) final cooldown, for $T > 240\,^{\circ}\mathrm{C}$ in Cd flux.

substrate temperature is gradually lowered until CdTe nanowires start to grow (II). In order to maintain optimal conditions at the growth front, T_{TC} has to be continuously increased (III). The narrow temperature window for the growth of CdTe nanowires makes it very challenging to match both the correct substrate temperature where nanowire growth starts and the time dependent increase. With the thermocouple as the only temperature sensor, the start of CdTe growth is inferred from the appearing of nanowire-specific facets in the electron diffraction pattern. [19] This method of controlling the growth temperature, however, comes with a delay of several minutes until crystal facets grow large enough to cause an observable change in the RHEED pattern. The temperature ramp that is required to maintain straight nanowire growth cannot be determined directly with the thermocouple and has to be empirically deduced from previous growth runs.

We now compare the thermocouple temperature with the band edge signal. In order to ensure a reliable measurement of the band edge, the increase of the background signal related to the increasing surface roughness during nanowire growth has to be avoided. We achieve this by probing a spot on the substrate without nanowires, which is prepared with a shadow mask during the formation of the nanowire growth seeds. From a thermocouple controlled growth run we realized that the surface temperature monitored by the band edge signal remains approximately constant. Therefore we perform the band edge controlled growth sequence by keeping T_{BE} constant during CdTe nanowire growth. The increasing difference between T_{TC} (black line) and T_{BE} (red line) during step III (Fig. 2.4) indicates that an increasing temperature gradient develops between the backside of the sample holder and the growth front, i.e., additional heating is required to compensate for energy losses at the sample surface.

To investigate the origin of these losses, we monitor the surface temperature of a bare GaAs wafer without nanowire seeds at a constant heating power during the exposure to either pure Zn, Cd, or Te flux. The result is shown in Fig. 2.5(a). We find that T_{BE} remains approximately constant for Zn or Cd, while for Te it decreases similarly to the observation during nanowire growth. From this we can conclude, that the temperature loss during the growth of the nanowires is mostly related to the supply of Te. When a sample is exposed to Te for a second time, the substrate temperature remains constant [cf. curves I and II in Fig. 2.5(b)]. Altering the surface properties, e.g., by covering the surface of the sample holder with a thin layer of In, resets the Te-induced change and a decrease in T_{BE} is again observed [cf. curve III in Fig. 2.5(b)]. Thus, a possible explanation for this observation is that the exposure to Te causes a permanent change of the thermal emissivity of the sample holder, which gradually increases the loss of energy on the exposed side throughout the growth of CdTe nanowires. This observation is important to consider for the thermometry during subsequent growth steps:

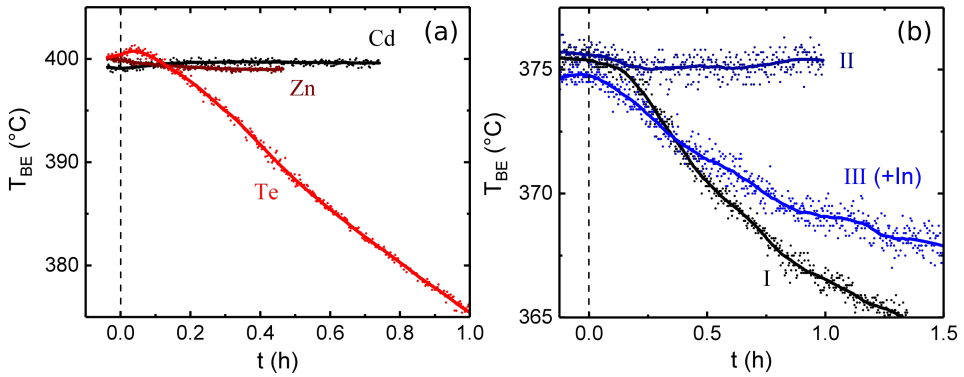

Figure 2.5: (a) Band edge signal obtained on a bare GaAs wafer exposed to either pure Cd, Zn, or Te flux at a constant heating power. (b) Repeated exposure of a GaAs wafer to Te flux; I: first run, II: second run, III: third run after In glue was spread on the sample holder. The data points are overlaid with an averaged curve for clarity.

After the initial nanowire growth, the relation between surface temperature and the thermocouple signal can be expected to be stable over time when the sample has been exposed to Te for more than about 3 h. This is especially crucial for the subsequent radial overgrowth with HgTe, because due to the small bandgap of HgTe the band edge signal degrades throughout overgrowth of the sample and after some time is not reliable enough for thermometry anymore. [48] However, knowing the initial offset between T_{TC} and T_{BE} the thermocouple can then be used to keep the substrate temperature sufficiently constant.

Figure 2.6(a) shows electron micrographs of CdTe nanowires which were grown at different values of T_{BE}. For 374 °C (central image) we find straight and vertical nanowires with a high reproducibility. When the substrate temperature is set by 1 °C higher, the axial growth rate reduces and pyramidal structures develop. For even higher temperature [377 °C, Fig. 2.6(a)] vertical growth is almost entirely suppressed. Already 1 °C below the optimal temperature the nanowires start to kink and grow in higher-indexed directions, which becomes even more pronounced at lower temperatures [371 °C, Fig. 2.6(a)]. By keeping the substrate temperature constant for several hours at 374 °C, we reproducibly achieve long and straight nanowires as shown in Fig. 2.6(b). This demonstrates, that band edge thermometry can indeed be used successfully for the growth of CdTe nanowires and gives precise feedback about the actual substrate temperature. However, it is important to note that the absolute value of the band edge signal T_{BE} can shift due to a difference in the substrate doping level. Thus, a precise calibration of the

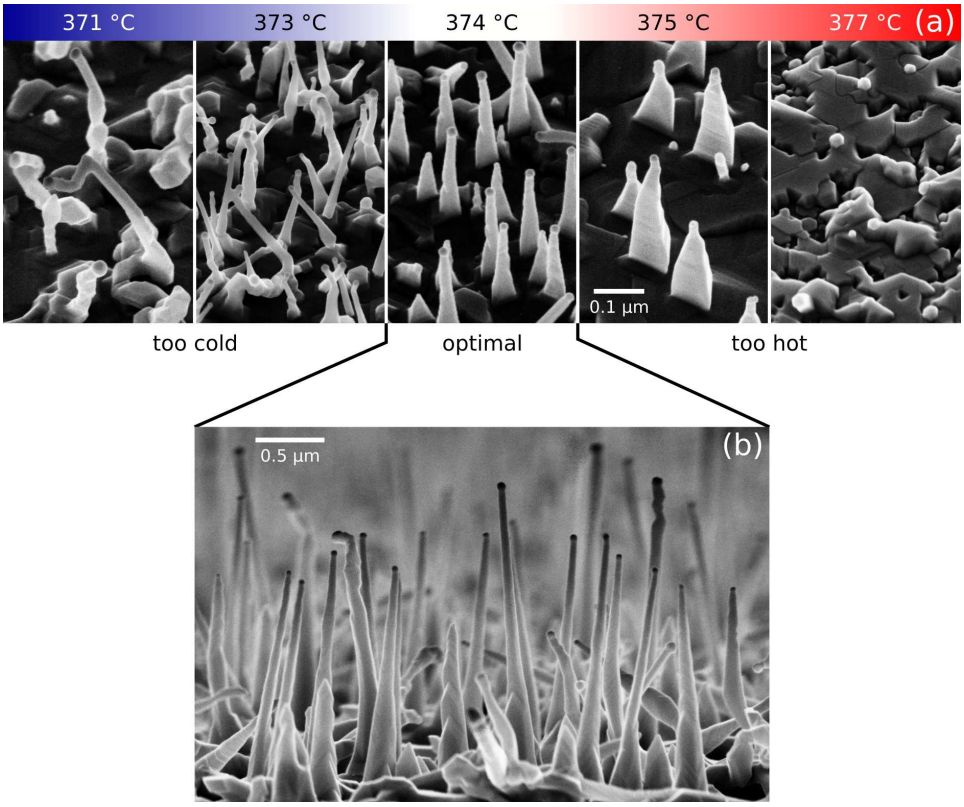

Figure 2.6: (a) A series of electron micrographs of CdTe nanowires grown on (111)B GaAs at different values of T_{BE}. (b) Nanowires grown at 374 °C for a longer time.

substrate temperature between different growth series is crucial, which is best achieved by determining the onset of CdTe growth from the emergence of nanowire-specific facets with RHEED while gradually lowering the substrate temperature, as described by Kessel *et al.* [19] With this, band edge thermometry provides a very high accuracy and reproducibility, which is the main key to a reliable growth process for CdTe nanowires despite the exceptionally small growth temperature window. A detailed description of this process is given in the Appendix A.

2.2 Structural characterization and crystal quality

The development of a reproducible growth process for CdTe nanowires is an important step for further optimization. The electron micrograph in Fig. 2.6(b) shows that the nanowires obtained are mostly free of kinks and have a large aspect ratio as desired for the fabrication of CdTe-HgTe core-shell nanowires. In the following, we discuss in detail the morphology and crystal structure of the CdTe nanowires. A thorough analysis of the macroscopic shape of the nanowires allows to draw conclusions about the underlying growth mechanism, and a detailed investigation of the crystal structure on a microscopic scale is important for discussing the quality of the nanowires for the subsequent epitaxial overgrowth with a HgTe shell.

Morphology of the CdTe nanowires

We begin with a general discussion of the geometric shape of the grown nanowires. In order to serve as a suitable basis for quasi-one-dimensional transport devices, the CdTe nanowires need to be long enough to place multiple contact electrodes on top, and their diameter should be small enough to ensure phase coherence along the circumference. In the scanning electron micrograph shown in Fig. 2.6 we find an overall variation of both the length and the diameter. On average, the nanowires have a diameter of 40–80 nm and a length of around 2 µm, which is ideal for templating HgTe nanowire shells. The observed morphological variation is likely a consequence of the self organized way of fabricating the growth seeds, which results in a randomly distributed droplet size. A smaller Au–Ga droplet seeds the growth of a nanowire with a smaller diameter, which in turn grows faster as long as growth is mostly affected by adatom diffusion from the substrate rather than by material directly impinging the droplet. [56] The lateral relocation of the growth seeds during the initial growth of the ZnTe stubs possibly enhances the morphological variation further. [14]

A closer look at the nanowires shown in Fig. 2.7(a) reveals that they are tapered with a decreasing diameter from base to tip. For most nanowires, the tapering is observed primarily in the lower part while the upper part exhibits more parallel side facets. Shrinking of the growth seed – for example due to the incorporation of Au or Ga into the growing nanowire – can be ruled out as the main origin, because CdTe nanowires grown for 8 h [Fig. 2.7(a)] still exhibit a similar diameter at the growth front compared to nanowires grown for only 2.75 h [Fig. 2.7(b)], as pointed out by the overlay image in Fig. 2.7(c). Instead, the tapering can be understood as a result of radial overgrowth during nanowire growth: The nanowires are grown at an elevated temperature compared to layer epitaxy in order to suppress direct vapor–solid overgrowth in favor of VLS-catalyzed axial nanowire growth. However, a

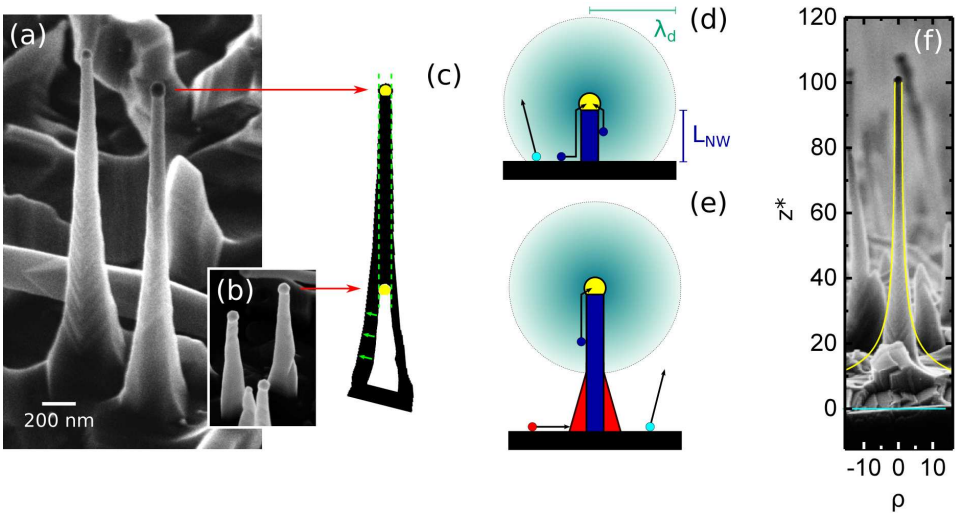

Figure 2.7: Electron micrographs of CdTe nanowires grown for (a) 8 h and (b) 2.75 h, together with a schematic overlay (c) of exemplary nanowires from (a) and (b). Images (d) and (e) illustrate different adatom processes (blue: vapor–liquid–solid incorporation, red: vapor–solid incorporation, turquoise: desorption) depending on the nanowire length L_{NW} and the adatom diffusion length λ_{d} sketched by the shaded sphere. The graph (f) shows a qualitative fit to the shape of the sides of an exemplary nanowire (in relative coordinates) with Eq. 2.2 for $L^{\star}_{\mathrm{NW}} = 100$. The electron micrograph in the background of the graph was acquired parallel to the substrate surface.

finite probability remains for direct incorporation of the supplied material preferentially at step edges of the nanowire side facets. The significance of this effect further depends on the ratio between the nanowire length L_{NW} and the adatom diffusion length λ_{d}. [57] For short nanowires, i.e., $L_{\mathrm{NW}} < \lambda_{\mathrm{d}}$, the Au–Ga droplets are the main sink of the diffusing adatoms that are not desorbed from the substrate surface. Hence, vapor–liquid-solid incorporation of the supplied material dominates the overall crystal growth, which results in a mostly untapered shape as sketched in Fig. 2.7(d). For longer nanowires, only the fraction of adatoms that impinge within a distance of less than λ_{d} from the next droplet – sketched by the shaded sphere in Fig. 2.7(e) – can contribute to the axial growth. The rest is either desorbed or contributes to vapor–solid overgrowth of the nanowire side facets. Thus, starting from the base of the nanowires, radial overgrowth occurs over time and becomes considerable when the length of the nanowires exceeds the adatom diffusion length. [57] It was shown, that in a purely diffusion-driven growth regime with a low vertical growth rate – a reasonable assumption since the CdTe

VLS growth is strongly limited by desorption – the nanowire shape ρ can be approximated by the analytical expression

$$\rho(L^{\star}_{\mathrm{NW}}, z^{\star}) = \frac{3}{4} + \frac{1}{4}\left(\frac{L^{\star}_{\mathrm{NW}} + \sqrt{2}}{z^{\star} + \sqrt{2}}\right)^2 \tag{2.2}$$

with the relative nanowire length $L^{\star}_{\mathrm{NW}}$ and vertical coordinate $z^{\star}$. [31] Figure 2.7(f) shows an electron micrograph of an exemplary nanowire where the shape of the nanowire is fitted with Eq. 2.2 ($L^{\star}_{\mathrm{NW}} = 100$, yellow line). The turquoise horizontal line indicates the position of the nanowire base ($z^{\star} = 0$). Apart from a small faceted region close to the base, the shape of the nanowire is very well reproduced, which further corroborates that nucleation on the nanowire sides can indeed explain the observed significant amount of tapering. The tapered shape of the CdTe nanowires is expected to especially impact quantum interference experiments on CdTe-HgTe core-shell nanowires, where the oscillation period of the magnetoconductance is linked to the magnetic flux enclosed by the conducting states in the HgTe shell. Hence, for the transport investigation it is crucial to use the part of the nanowire close to the tip where the nanowire sides are mostly parallel.

Crystal quality of the CdTe nanowires

Previous studies on the crystal quality of CdTe nanowires focused mostly on high-resolution X-ray diffraction (HR-XRD) and RHEED. [14,17] The results obtained with these techniques indicate a good overall crystal quality and an epitaxial relation to the substrate. Further, the diffraction experiments show the presence of twinning in the samples. However, due to the integrative nature of HR-XRD and RHEED it is not possible to determine whether the twinning occurs only at the interface to the substrate, or if it is also found within the individual nanowires which could affect the subsequent overgrowth. In the following, we present the main results of a comprehensive transmission electron microscopy (TEM) study in order to investigate the crystal quality of the CdTe nanowires on a local scale. The TEM investigation was carried out at the Norwegian Center for Transmission Electron Microscopy (NORTEM) by R. Bakke during her masters project [58] at the Department of Physics, NTNU Trondheim (Norway) under supervision by S. Wenner and A. T. J. van Helvoort.

Previous work suggested that the majority of CdTe nanowires are zinc blende crystals growing along [111]B. [14] Thus, when grown on a (111)B-terminated substrate, most nanowires grow perpendicular to the surface. This is desired when the nanowires are to be overgrown on all side facets with a tubular closed HgTe shell. [19] However, if we take a closer look at the nanowires grown on (111)B shown in Fig. 2.6(b), we observe that many of

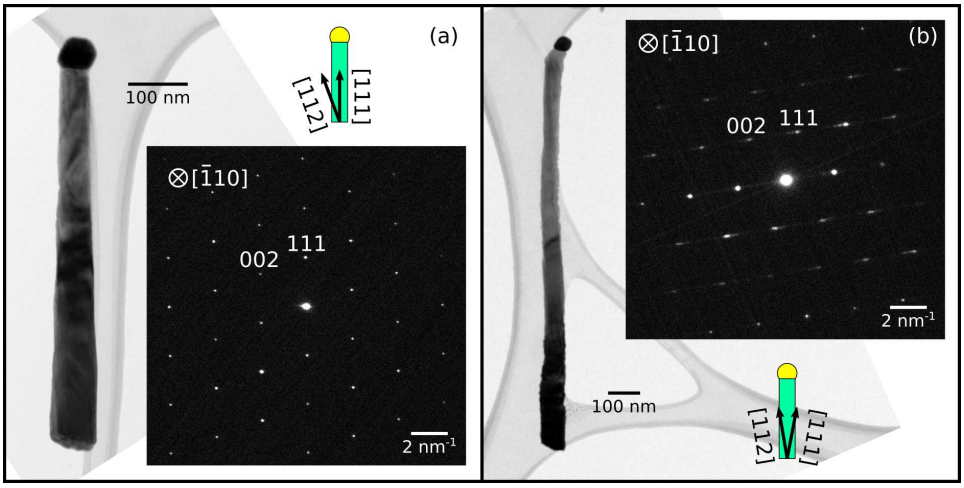

Figure 2.8: Brightfield TEM images of zinc blende CdTe nanowires together with a corresponding diffraction pattern along the $[\bar{1}10]$ zone axis. The relation between the nanowire growth axis and the [111]/[112] crystal directions as inferred from the diffraction pattern is schematically depicted.

the nanowires are close to but not exactly perpendicular to the substrate. The typical growth direction for most VLS-grown zinc blende nanowires is [111]. [36] Hence, understanding the origin for the deviating orientation of the CdTe nanowires could give valuable information about the growth regime, which is crucial for the optimization of the growth process. The local crystal structure of individual nanowires is most reliably detected by TEM, and the direct comparison of real-space imaging with a simultaneously acquired electron diffraction pattern is a precise technique to determine the growth direction. Therefore, a bunch of nanowires from the sample shown in Fig. 2.6(b) was prepared for TEM investigation. The results obtained from two exemplary nanowires are shown in Fig. 2.8. The nanowire depicted in the transmission electron micrograph of Fig. 2.8(a) exhibits the regular [111] growth axis as inferred from the corresponding diffraction pattern. The nanowire shown in Fig. 2.8(b), however, grew neither along [111] nor along [112] which would be the closest low-indexed stable crystal facet, but appears rather oriented in between both.

In order to investigate the origin of this intriguing unusual growth direction, high resolution TEM images of this particular nanowire were acquired. Figure 2.9(a) shows the results obtained from the nanowire base. Most strikingly, dark stripes are visible that run through the nanowire at a small angle from the growth direction. They are identified as a set of $(\bar{1}\bar{1}1)$ planes. From the atomically resolved micrographs in the insets of Fig. 2.9(a) we can infer that the observed stripes are in fact 60°/180° rotational twin planes,

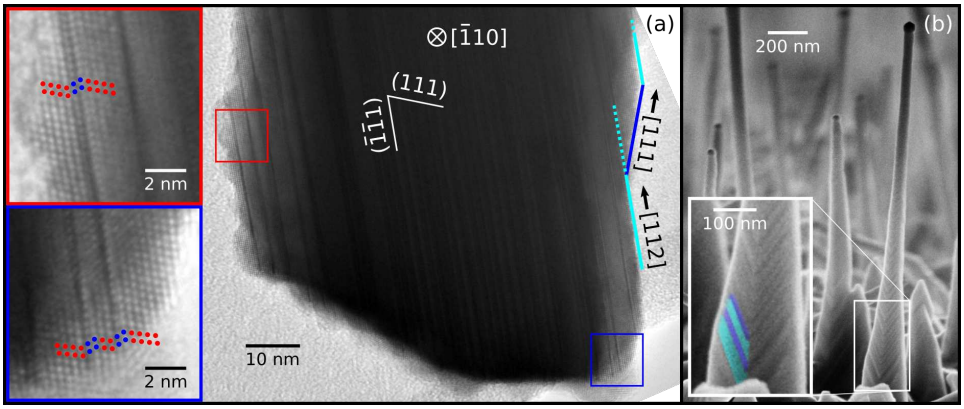

Figure 2.9: (a) High resolution brightfield TEM images obtained from the base of the nanowire shown in Fig. 2.8(b). The main crystal planes and directions are labeled. The insets show atomically resolved high magnification details from the marked positions. Red and blue dots highlight the stacking order of $(\bar{1}\bar{1}1)$ crystal planes. (b) Scanning electron micrograph of the as-grown sample. False colors in the inset highlight the corresponding crystal facets indicated in the right hand side of image (a).

where the stacking sequence is reversed mostly for only one or two layers [highlighted by the blue dots in Fig. 2.9(a)] before it switches back to the original stacking sequence (red dots). The occurrence of periodic lattice defects in nanowires is typically observed when a large lattice mismatch to the substrate is present, [59] which in this case has a value of 13.7% [47] between the CdTe nanowires and the GaAs substrate. It is remarkable that new misfit dislocations are formed on the entire length of the nanowires, even far away from the substrate. The large lattice mismatch to the substrate leaves us with essentially two approaches attempting to avoid the observed planar defects in the nanowires: On the one hand, the effect of lattice mismatch reduces with the nanowire diameter. Below a critical diameter the nanowires are expected to be essentially free of lattice mismatch-induced defects (cf. Fig. 1.3 in Section 1.2), [32] but the diameter of the CdTe nanowires can hardly be influenced due to the self-organized formation of the growth seeds and the subsequent relocation at the early stage of growth. On the other hand, growing the CdTe nanowires onto long ZnTe nanowires rather than only short stubs can possibly improve the buffering effect of the ZnTe structure in order to reduce the effective lattice mismatch down to 6.1%, [47] the native mismatch between CdTe and ZnTe unaffected by the GaAs substrate, which might be low enough to achieve a defect free CdTe nanowire segment. However, inferring the correct substrate temperature for CdTe nanowire growth from RHEED relies on the appearing of a nanowire-specific diffraction pattern,

which would already be present with the ZnTe nanowires. Hence, this option would not allow to directly calibrate the band edge substrate temperature for CdTe growth, which makes the growth process less reliable.

Based on the structural analysis we can draw several conclusions: Due to the large aspect ratio and a length that is sufficient for the fabrication of transport devices the nanowires are suited for overgrowth with an epitaxial HgTe shell. The occurrence of planar twinning defects in the CdTe nanowires should *per se* not alter the charge transport characteristics as the CdTe core can still be safely assumed as an insulator at low temperature. However, HgTe grows epitaxially on CdTe, hence the defects are expected to continue into the HgTe shell, which in turn might affect charge transport. For the observation of defect-sensitive effects such as probed in quantum interference experiments it might be important to avoid these planar defects. Further, we observe that the VLS growth of CdTe nanowires comes with a significant contribution of axial overgrowth, which leads to a considerable amount of tapering and, consequently, an inhomogeneous cross-section. The exceptionally narrow growth temperature window makes further optimization challenging, despite the enhanced temperature control provided by band edge thermometry. Thus, as an alternative approach we instead investigate in the next chapter ZnTe nanowires as a high quality template for HgTe overgrowth, which has in particular a larger tolerance with respect to the substrate temperature.

Chapter 3

Selective area grown ZnTe nanowires

So far, CdTe nanowires grown from self-organized Au–Ga droplets were used as a template for HgTe overgrowth. Even though the advancements presented in the previous chapter significantly enhanced the control over the strongly temperature-sensitive CdTe VLS growth, the exceptionally narrow growth temperature window still imposes strong limitations for the necessary further optimization. Additional boundaries for growth development arise from the random distribution of the growth seeds formed by the thermal dewetting of a thin Au layer, such as an inhomogeneous nanowire diameter and length, and the shadowing of the material flux as well as competitional effects between adjacent nanowires due to the high areal density.

In order to overcome these obstacles, this chapter investigates an entirely different approach: The position-controlled growth of ZnTe nanowires as the basis for tubular CdTe/HgTe multishells. The significantly larger temperature window for the VLS growth of ZnTe nanowires, together with the precise thermometry technique developed for CdTe nanowires in Section 2.1, offers a much wider range for optimization. Further, employing a selective area method for the fabrication of nanowire arrays allows to establish homogeneous and stable growth conditions for both the nanowire core and shell.

This chapter starts with a discussion of the fundamental requirements to achieve the position-controlled growth of ZnTe nanowires. An investigation of the growth kinetics allows us to optimize the ZnTe nanowire arrays for radial overgrowth, which is followed by a structural investigation both on a macroscopic and an atomic scale. With the optimized growth process we are able to fabricate ZnTe nanowires that are ideal for subsequent radial overgrowth. Parts of this chapter are published in »J. H. *et al.*, Phys. Rev. Materials **4**, 066001, (2020)«.

3.1 Achieving position-controlled nanowire growth

The position-controlled fabrication of nanostructures – also referred to as selective area growth – is a powerful tool to combine the main advantages of the two fundamental approaches to nanofabrication, which are the high degree of control over position and geometry of top–down procedures and the high structural quality of self-assembled bottom–up techniques. Reports on the position controlled growth of nanowires mostly employ silicon oxide or silicon nitride masks with predefined holes, which serve as nucleation sites for the growth. This approach is typically used for the self-catalyzed growth of III-V semiconductor nanowires, where the group III element acts as VLS growth seed. [61–63] The VLS-MBE of ZnTe nanowires, however, requires an additional liquid metallic growth seed. So far, only self-organized growth of ZnTe nanowires was reported where self-assembled Au–Ga [42, 43] or Au–Si [64] droplets were used to seed the growth. Here, we explore a different approach in order to achieve the position controlled growth of ZnTe nanowires by nano-patterning the Au-based VLS growth seed.

The vapor–liquid–solid growth of II-VI nanowires is strongly affected by the properties of the growth seed. A precise control of its physical properties such as the melting point and the droplet volume, as well as its chemical composition is crucial for successful nanowire synthesis. The eutectic alloy of Au and Ga, provided by the thermal dewetting of a thin layer of about 1 nm Au on top of a GaAs substrate, introduced in Chapter 1 for the growth of CdTe nanowires, proves to be well suited also for the self-organized growth of ZnTe nanowires (cf. Fig. 3.1). Hence, we rely on Au–Ga growth seeds for the development of a selective area VLS process for ZnTe nanowires. In order to allow precise control of the diameter and position of each individual nanowire, we use an electron beam lithography based lift-off process to pattern gold

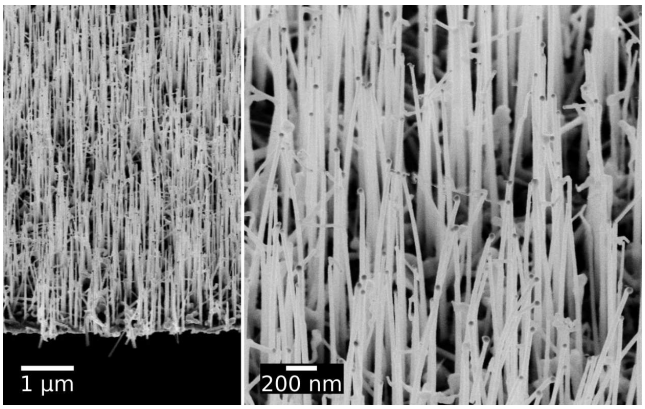

Figure 3.1: Electron micrographs of self-organized ZnTe nanowires grown by VLS-MBE on a Si-doped (111)B GaAs substrate.

disks, which – supplied with the right amount of Ga – serve as the growth seeds. In the following we will describe the key points in the fabrication of the growth seeds, as well as the subsequent steps required to achieve the growth of free-standing vertical nanowires. Beyond that, comprehensive instructions are listed in the Appendix B.

Selective area fabrication of VLS growth seeds

First, we discuss the lithographic fabrication of the Au disk array. The main steps are sketched in Fig. 3.2. Sample preparation starts with the spin-coating of a substrate with a two-layer polymethylmethacrylate (PMMA) resist [Fig. 3.2(a)]. We use a less electron sensitive resist as top layer compared to the bottom layer in order to achieve an aperture after the development. This is required to prevent Au deposition on the PMMA sidewalls. The size of the resist aperture is adjusted by the dot exposure time of a spot on the substrate, which defines the diameter of the Au disk [Fig. 3.2(b)]. Since a clean crystal surface underneath the Au is crucial, an Ar ion milling step is applied prior to the evaporation of Au without breaking the vacuum in between [Fig. 3.2(c)]. Finally, the resist is stripped in acetone, leaving just the Au that is in direct contact to the substrate [Fig. 3.2(d)]. Typically, the Au disks have a diameter of about 70 nm and a height of 27 nm, and they are patterned in a hexagonal array to achieve a more homogeneous next-neighbor distance.

The high melting temperature of Au alloyed with the materials that are supplied during growth, i.e., of Au–Zn [65] and Au–Te [66], requires to add an additional element in order to provide a liquid VLS seed at the typical growth temperatures of 430–450 °C for ZnTe nanowires. Adding about 30at% of Ga reduces the melting point to below 360 °C, [67] which is low enough to ensure reliable conditions for VLS nanowire growth. Further, Ga has a high solid solubility in Au, [67] which facilitates the alloying of the patterned

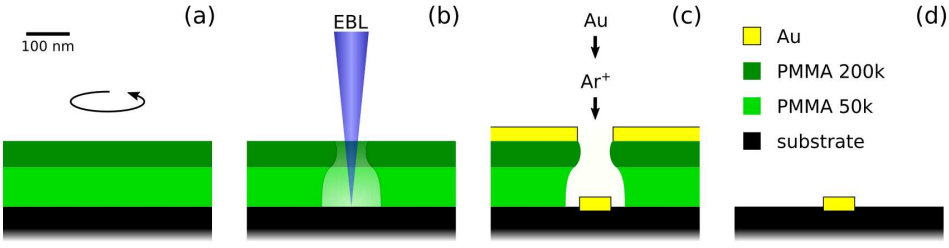

Figure 3.2: Schematic depiction of the main steps of Au disk lithography: (a) spin-coating of a two-layer PMMA resist, (b) electron beam dot exposure and subsequent development, (c) Ar ion milling followed by Au deposition, (d) final structure after lift-off.

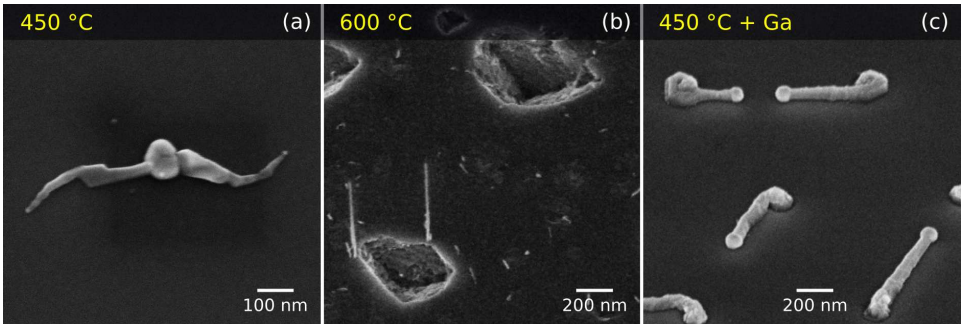

Figure 3.3: ZnTe nanowires grown on Si-doped (111)B GaAs substrate from Au disks annealed at (a) 450 °C, (b) 600 °C, and (c) 450 °C after exposure to Ga flux.

Au disks. For the self-organized growth of nanowires, the GaAs substrate is typically used as Ga source for the thermal dewetting of a thin Au layer at about 450 °C. Applying the same procedure to Au disks patterned onto a GaAs substrate does not yield the desired result: Figure 3.3(a) shows ZnTe nanowires grown from Au disks that were annealed for 10 min at 450 °C. The shape of the resulting nanowires indicates that only minor parts of the Au disk are able to seed nanowire growth while the rest remains solid. Apparently, the greatly reduced surface–to–volume ratio of the Au disks – compared to the 1 nm thin Au layer in the self-organized process – does not allow for a sufficient diffusion of Ga into the Au. Heating the substrate to 600 °C in order to enhance the Ga interdiffusion does also not yield the desired result of nanowire growth at predefined sites; there, the accompanying dissociation of the substrate results in large thermal etch pits in place of the Au disks and a strong delocalization of the Au is observed in Fig. 3.3(b). Thus, it appears more reliable to supply additional Ga from an effusion cell. To do so, the sample is heated to 250 °C in the III-V MBE chamber in order to enhance the diffusion of Ga on the sample surface. Ga is then supplied with a beam equivalent pressure of around 5×10^{-8} mbar for 120 s in total. Separating the Ga supply into six iterations of 20 s followed by 120 s delay ensures sufficient time for the intermixing of Au and Ga. Subsequently, the sample is transferred to the II-VI chamber and heated to 430–450 °C. With this method we finally achieve the growth of a single ZnTe nanowire from each Au disk [cf. Fig. 3.3(c)]. The spherically shaped droplet at the tip of the nanowires indicates that the array of Au disks was successfully transformed into liquid Au–Ga droplets that are able to seed VLS growth. However, most of the nanowires grow parallel to the substrate surface. Thus, we thus discuss in the following the fabrication steps that are necessary to achieve the position controlled growth of vertical free-standing ZnTe nanowires.

Substrate preparation for vertical nanowire growth

The position controlled ZnTe nanowires shown in Fig. 3.3(c) grow almost exclusively laterally on the GaAs substrate. From self-organized ZnTe VLS growth, shown in Fig. 3.1, we know that the most stable growth direction of ZnTe nanowires is [111]B. Hence, one or several effects make lateral growth energetically more favourable. An obvious source for additional energy can be seen in the large lattice mismatch of 7.6% [47] between the GaAs substrate and the ZnTe nanowires. From Fig. 1.3 (Section 1.2), we expect for this amount of lattice mismatch the formation of dislocations above a critical nanowire radius of approximately 20 nm, which can possibly explain the observed lateral growth. Thus, for now we focus only on the homoepitaxial nanowire growth on virtual ZnTe substrates, which we prepare as an 0.5–1 µm thick MBE-grown buffer layer on top of a Si-doped (111)B GaAs wafer.

The position controlled growth of ZnTe nanowires from an array of Au discs on ZnTe substrate, prepared the same way as discussed with Fig. 3.3(c), results in a similar picture [cf. Fig. 3.4(a)]. Again, the spherical droplet at the nanowire tip indicates successful VLS growth, which demonstrates that supplying Ga from an effusion cell rather than from the substrate allows in

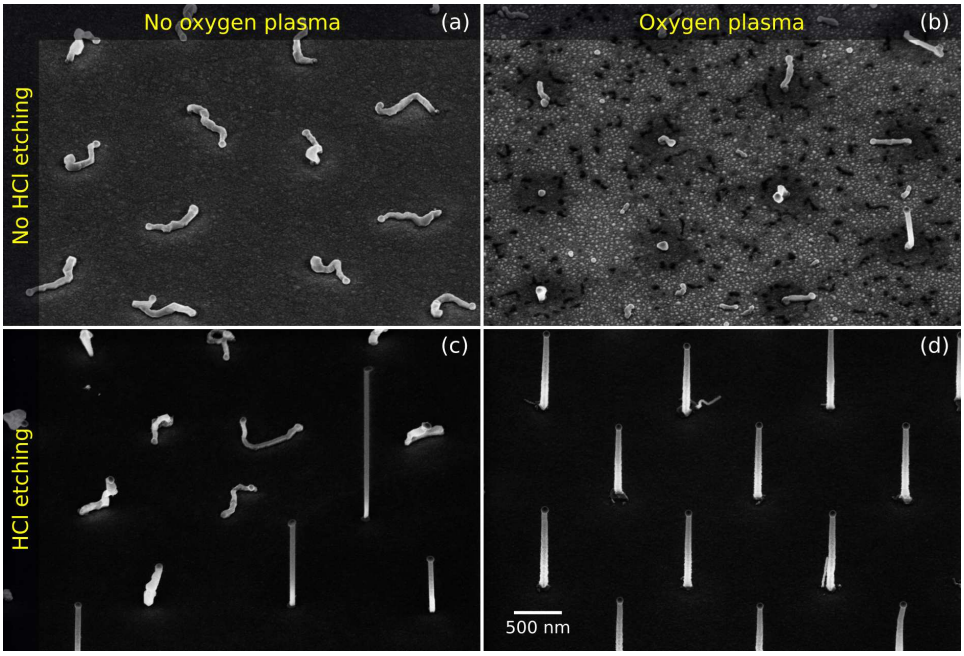

Figure 3.4: ZnTe nanowires grown on (111)B ZnTe substrates treated with different *ex situ* preparation steps: (a) without additional cleaning, surface cleaning with (b) oxygen plasma only, (c) HCl dip only, and (d) both oxygen plasma and HCl dip.

principle to change the substrate material freely. However, the nanowires still grow laterally on the substrate; hence, avoiding a heterointerface between substrate and nanowire is not sufficient to ensure vertical nanowire growth. A major difference to the self-organized VLS growth – where we observe mostly vertical nanowires – is the involvement of lithographic substrate processing that can possibly lead to a carbon contamination of the surface. Carbon is known as a source of crystal defects for epilayer growth [68] and thus might also be a trigger for lateral nanowire growth. Further, sidewalls around the Au disks can be formed by redeposited material that might not be entirely removed during the lift-off, which can additionally disturb the initial nucleation. In a first attempt we used an oxygen plasma cleaning step to remove residues of PMMA and organic solvents. The result is shown in Fig. 3.4(b). The presence of few vertical wires indicates that the plasma treatment provides a certain improvement but is still not sufficient. Apart from a circular region around the nanowires with a diameter of approximately 0.4 µm the surface appears significantly rougher, which can be attributed to a reduced diffusion length of adatoms on the oxygen plasma treated surface. In order to further improve the surface quality, residues of the oxygen plasma treatment are removed together with possibly remaining sidewalls around the Au disks by an additional etching step in aqueous hydrochloric acid (HCl). The result justifies the cleaning process. Figure 3.4(d) shows a very high yield of vertical nanowires. Surface cleaning involving HCl etching only is not sufficient, as can be seen in the example given in Fig. 3.4(c).

In order to see whether the correct substrate preparation alone is the main key to vertical nanowire growth, we now compare how the choice of the substrate material influences the ZnTe nanowire growth. To do so, we examine different configurations of lattice matched and mismatched growth on (III-V) and (II-VI) substrates. Arrays of Au–Ga growth seeds are prepared on GaAs, InAs, ZnSe and ZnTe (111)B substrates; the latter three are provided as 0.5–1 µm thick MBE-grown layers on GaAs. Figure 3.5 summarizes the results. On GaAs, Fig. 3.5(a), the percentage of vertical nanowires is almost zero. We attribute this observation to the fact that the large lattice mismatch of 7.6% [47] between GaAs and ZnTe does not favor vertical nanowire growth, which might additionally be enhanced by the unsaturated bonds at the (III-V)–(II-VI) interface. For InAs as well as for ZnSe substrate, Figs. 3.5(b) and (c), we observe only little improvement compared to GaAs. While the InAs substrate is nearly lattice matched but still exhibits dangling bonds at the interface, the ZnSe substrate provides a crystallographically correct interface but again does not match the lattice constant. Hence, both parameters appear to be essential for the growth of straight and free-standing nanowires. For the homoepitaxial growth of ZnTe nanowires on a ZnTe substrate both parameters are matched, and we observe an almost perfect yield of vertical nanowire growth [cf. Fig. 3.5(d)].

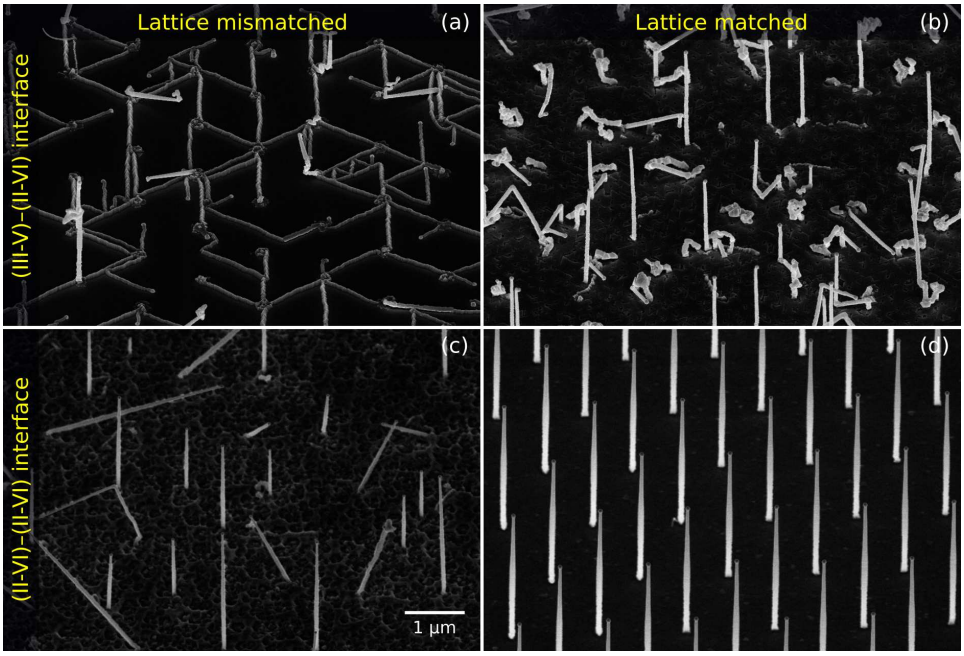

Figure 3.5: ZnTe nanowires are grown under similar conditions at 440 °C on diverse (111)B substrate materials: (a) GaAs, (b) InAs, (c) ZnSe, and (d) ZnTe. These materials cover the different possible options regarding lattice mismatch (columns) and interface type (rows) between substrate and nanowire.

For a high yield of position controlled vertical ZnTe nanowires, the VLS growth on a ZnTe substrate with an according two-step substrate cleaning gives the best results. Further optimization of the ZnTe nanowires with respect to templating radial HgTe shells for transport devices is thus based on these findings.

3.2 Investigation and optimization of the growth kinetics

In the previous section we showed for the first time the successful realization of position controlled ZnTe nanowire arrays grown by VLS-MBE. Their essentially untapered shape and high ensemble uniformity makes them a very promising basis for radial HgTe nanowire heterostructures as an alternative to the CdTe nanowires discussed in Chapter 2. In the following, we discuss how growth parameters such as the substrate temperature and the pitch distance between adjacent nanowires influence the growth rate and morphology of the nanowires. This allows us to investigate the kinetics of the VLS process in order to optimize the nanowires for subsequent radial overgrowth. The statistical data presented in this section was averaged over at least 20 nanowires for the nanowire length and axial growth rate, and the yield of vertical nanowires was inferred from 3–5 representative sample areas that each contain about 600–1200 growth seeds.

Optimization of the growth temperature

Important for the radial overgrowth of the ZnTe nanowires is their length and shape. For both, one of the key parameters is the substrate temperature and its constancy during growth. We use band edge thermometry, which is discussed in Section 2.1, to control the substrate temperature precisely. Figure 3.6 shows the results of a growth series of ZnTe nanowires grown at different substrate temperatures in the range of 420–460 °C. From the electron micrographs shown in Fig. 3.6(a) we infer that at 440 °C we obtain a very uniform array of nanowires pointing along the vertical [111]B direction. For temperatures below 440 °C the nanowires tend to kink and grow in various higher-indexed directions. Above 440 °C both the axial growth rate and the yield of vertical nanowires reduce until growth is fully suppressed at 460 °C.

For a systematic analysis of the influence of the substrate temperature we compare the yield of vertical nanowires in Fig. 3.6(b). The highest yield, in this growth series about 50%, we find at 440 °C. Towards higher temperature the yield reduces continuously until it reaches zero at 460 °C. From electron micrographs we find that the non-vertical nanowires grown at high temperatures are typically straight and kink-free but grow at a large angle from the surface normal. Hence, a suppression of vertical growth towards higher temperatures can possibly be explained by the thermally activated formation of additional stable crystal facets aside from the (111)B surface parallel to the substrate, which can promote nanowire growth in tilted directions. Towards lower temperature we also observe a decreasing yield in addition to pronounced kinking, which occurs either half-way towards the tip (these nanowires are counted as vertically grown) or directly at the base.

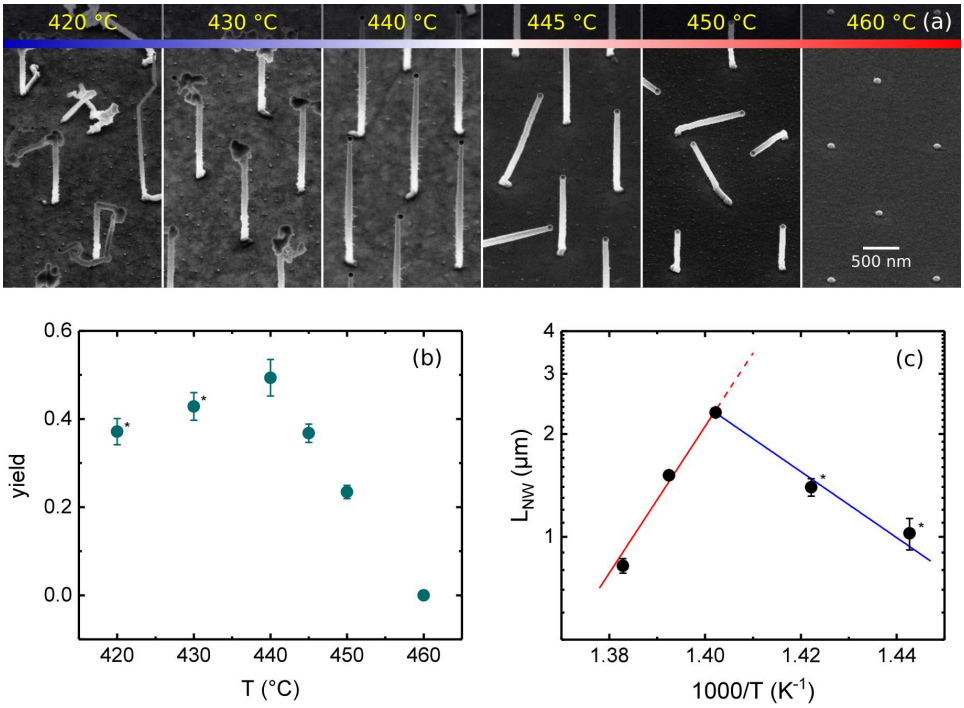

Figure 3.6: (a) Electron micrographs of ZnTe nanowires grown for 150 min at different substrate temperatures ranging from 420–460 °C. Growth temperature dependence of (b) the yield of vertical ZnTe nanowires and (c) the nanowire length L_{NW}. The red line in (c) is an Arrhenius-fit to the data for $T = 440$–$460\,^{\circ}\mathrm{C}$, the blue line for $T = 420$–$440\,^{\circ}\mathrm{C}$ where low-temperature kinking limits the length of the nanowires (data points marked by stars *).

Apart from the yield, the substrate temperature influences also the length of the nanowires L_{NW}. In Fig. 3.6(c), L_{NW} is plotted on a logarithmic scale against the inverse temperature. This so-called Arrhenius graph is often used to analyze the effect of temperature on diffusion-driven processes because it transforms an exponential temperature dependence of the shape

$$L_{\mathrm{NW}} = Ce^{-E_{\mathrm{d}}/(k_{\mathrm{B}}T)} \tag{3.1}$$

to a straight line. E_{d} denotes the potential energy barrier for diffusion, sometimes also referred to as the activation energy, and can be deduced from the slope of a linear fit to the data in the Arrhenius graph, C is a prefactor and k_{B} the Boltzmann constant. Depending on the sign of E_{d}, Equation 3.1 can be used to describe thermally activated ($E_{\mathrm{d}} > 0$, negative slope in the Arrhenius graph) or suppressed ($E_d < 0$, positive slope) processes. For a higher substrate temperature of 440–450 °C, L_{NW} is fitted by a linear increase [red line in Fig. 3.6(c)]. This indicates, that the growth rate of ZnTe

nanowires is mainly driven by adatom diffusion to the growth front, which in this temperature range is limited by desorption. [31] At lower temperatures the nanowires start to kink. For these data points (marked by stars *) the plotted value of L_{NW} resembles the length of the vertical segment at the nanowire base. Interestingly, also in this temperature range L_{NW} follows a linear trend, but with a negative slope [blue line in Fig. 3.6(c)]. Hence, the kinking of nanowires towards lower substrate temperature can possibly be understood as a result of a thermally deactivated nucleation process, such as adatom nucleation on the nanowire sides, or the clustering of material at the triple phase boundary between droplet, crystal and gas phase. [69]

Further, a more detailed view on the nanowire morphology shows that the substrate temperature affects also the cross-sectional shape. Figure 3.7 summarizes the results for nanowires grown at a substrate temperature of 440, 445 and 450 °C. Depending on the temperature, we observe a clear change in morphology. For 450 °C, Fig. 3.7(c), the cross-section of the nanowire appears circular with a diameter defined by the spherical VLS growth seed. For a slightly reduced substrate temperature [445 °C, Fig. 3.7(b)] the cross-section begins to develop facets resulting in a shape that resembles a truncated triangle. For 440 °C, Fig. 3.7(a), the faceting seems completed and a fully trigonal shape evolves. The morphological change can be explained by the influence of the substrate temperature on the direct vapor–solid incorporation of adatoms on the nanowire sides: In principle, the cross-section of the nanowire is defined by the shape of the growth seed, resulting in a circular geometry. However, at lower temperatures a finite probability for vapor–solid nucleation of adatoms leads to the enlargement of the most stable side facet,

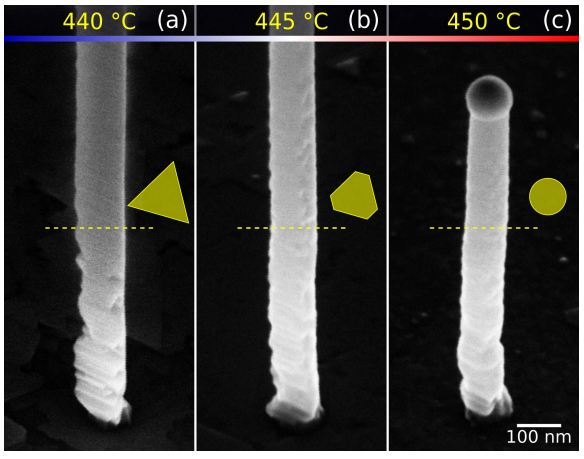

Figure 3.7: Electron micrographs of ZnTe nanowires grown under similar conditions at different substrate temperatures of (a) 440 °C, (b) 445 °C, and (c) 450 °C together with a sketch of the estimated cross-section.

which explains the formation of the triangular cross-section observed for 440 °C. An increasing growth temperature shifts the growth kinetics further towards desorption and thus suppresses this effect. Hence, for high substrate temperature the cross-section remains circular. It is interesting to note that, contrary to the CdTe growth discussed in Chapter 2, the ZnTe nanowires do not develop a tapered shape. This indicates that the faceting observed at 440 °C is a self-limited process, i.e., the nucleation of material occurs only as long as the faceting is not yet complete, but appears to be suppressed on top of the stable side facet, which prevents further overgrowth.

These results show that by adjusting the substrate temperature we are able to control the cross-sectional shape of the nanowires. But the high substrate temperature required for a more circular cross-section – which is favourable for the subsequent overgrowth – reduces the yield and the growth rate of well oriented nanowires. Hence, based on the purpose of the nanowire sample a suitable compromize has to be found. With the detailed analysis of the influence of the growth temperature, it is possible to straightforwardly determine the most suitable growth parameters for a particular sample.

Influence of the pitch distance

For self-organized ZnTe nanowires we observe a dense distribution of nanowires with a strongly varying distance between adjacent nanowires (cf. Fig. 3.1). The selective area technique allows us now to freely adjust this distance. Hence, it is important to investigate if, and how, the spacing between adjacent nanowires influences the VLS growth. To do so, we compare ZnTe nanowire arrays with a pitch distance in the range of 0.4–6.4 µm. The arrays are grown in close proximity on the same substrate, which ensures consistent growth conditions. Electron micrographs of the resulting samples are depicted in Fig. 3.8(a), and Fig. 3.8(b) shows a statistical analysis of the nanowire arrays. Overall, we find a similar behavior for the yield of vertical growth [black data points in Fig. 3.8(b)] and the average growth rate r_g (red, right axis). Both are mostly constant for the larger pitch distances of 0.8–6.4 µm. However, for the smallest spacing (0.4 µm) we find a significant drop in the yield by almost a factor of two. This sharp transition in the vertical yield is accompanied by a reduced axial growth rate. We can explain this behavior as the manifestation of two distinct growth regimes: [70] When the distance between the nanowires δ_{NW} exceeds twice the surface diffusion length of adatoms λ_d, growth is limited only by adatom diffusion and the nanowires can be treated as isolated. This results in a growth rate that is independent of the next-neighbor distance, and the vertical yield is consistently high at around 90%. For $\delta_{NW} < 2\lambda_d$, however, adjacent nanowires begin to compete for the availible material. In this competition-limited regime the pitch distance defines the adatom capture area; hence, a reduced distance between the nanowires results in a reduced

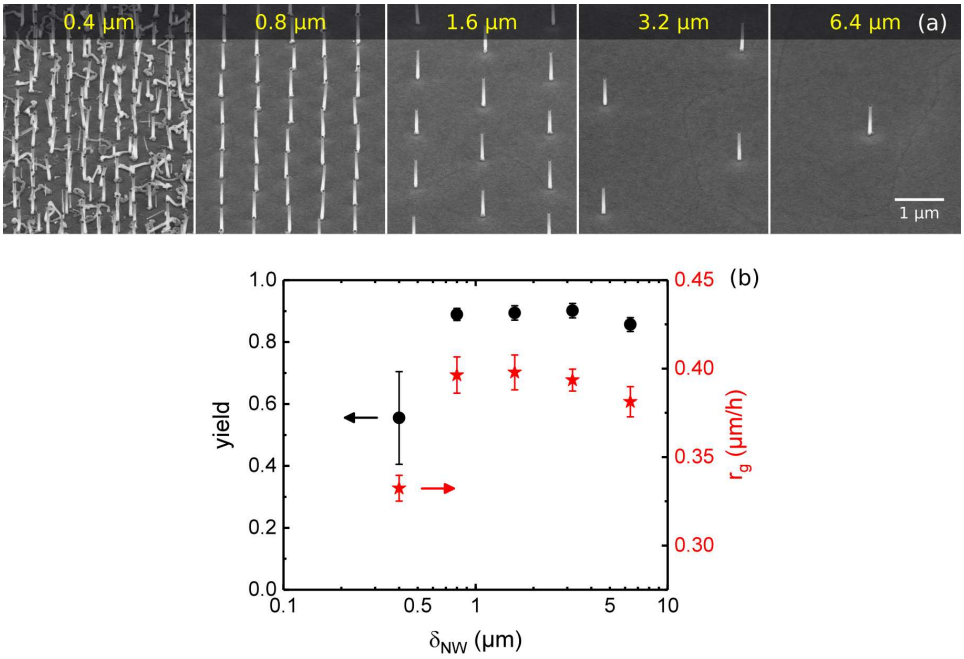

Figure 3.8: (a) Electron micrographs of ZnTe nanowire arrays with a pitch distance δ_{NW} between adjacent nanowires ranging from 0.4–6.4 µm (left to right). (b) Influence of the pitch distance on the yield of vertical growth (black circles, left axis) and the axial nanowire growth rate r_g (red stars, right axis).

axial growth rate compared to the diffusion-limited case. In general, the diffusion length differs for individual atomic species, thus upon entering the competition-limited regime the effective material composition reaching the growth seeds might change. This could explain the influence of a small pitch distance also on the vertical yield. Shadowing effects can be safely excluded as the origin of the significant decrease in yield, because most of the growth defects leading to non-vertical growth occur already at the nanowire base.

With a spacing of 0.8 µm or larger, competitional effects during the ZnTe nanowire growth can be avoided. The position-controlled process allows us to freely adjust the distance between the adjacent nanowires, and to increase it beyond the competition-limited regime. This corroborates its advantage with respect to the homogeneity and reliability over the self-organized approach, where a typical spacing of 0.2 µm or less between adjacent nanowires is observed (cf. Fig. 3.1). The findings of this growth study allowed us to optimize the morphology of the ZnTe nanowire arrays for radial overgrowth. Apart from the appropriate geometrical properties, a high crystal quality of the ZnTe cores is crucial for the epitaxy of nanowire shells. Hence, a detailed analysis of the crystal quality is the focus of the following section.

3.3 Structural characterization and crystal quality

Up to now, we optimized the position-controlled growth of ZnTe nanowires with respect to their morphology. Apart from that, the crystal quality of the ZnTe nanowires is a second crucial parameter for subsequent radial overgrowth as it determines, to some extent, the quality of the radial shells. Thus, a detailed characterization of the crystal structure – especially with respect to defects and impurities – is the focus of this chapter. Integrative techniques on the as-grown samples, i.e., RHEED or HR-XRD, are not suitable because on the one hand the nanowire arrays typically have about two orders of magnitude lower areal density compared to self-organized samples which drastically reduces the signal strength, and on the other hand the substrate consists of the same material, ZnTe, and thus superimposes the signal generated by the nanowires. Hence, we use TEM as a local probe on individual nanowires in order to characterize the material distribution and the crystal quality of the ZnTe nanowire arrays. The TEM investigation was carried out by S. Wenner at the NORTEM facility in Trondheim, Norway.

Material distribution in the ZnTe nanowires

In a first experiment we investigate the material composition of the nanowires. The element distribution within a sample can be mapped with energy dispersive X-ray spectroscopy (EDX). Typically, a focussed electron beam is used to generate characteristic X-ray radiation in the sample. The spatial resolution of EDX is therefore mainly limited by the lateral spread of the electron beam, which is minimized for high energetic electrons. Thus, performing the EDX analysis in a scanning transmission electron microscope allows to precisely map the spatial distribution of elements within a single nanowire. Figure 3.9 shows the distribution of Au, Ga, Zn and Te in the vicinity of a nanowire's tip. From the EDX data we infer that the nanowire itself consists exclusively of Zn and Te. Au and Ga are not detected within the nanowire and can only be found in the metallic droplet at the tip. This indicates that both materials act solely as a catalyst for the nanowires and are essentially not incorporated into the nanowire. Furthermore, while Au seems to be homogeneously distributed within the droplet, Ga appears to occur in two different concentrations. This points to a non-eutectic Au–Ga alloy which solidifies in two phases with different stoichiometry during cooldown. [67] Additionally, a significant amount of Zn is found in the droplet, which at the same time is nearly free of Te. This is consistent with the low solid solubility of Te in Au [66] compared to Zn [65] and indicates a growth mechanism where Zn is dissolved within the droplet while Te is transported to the growth front mostly by surface processes.

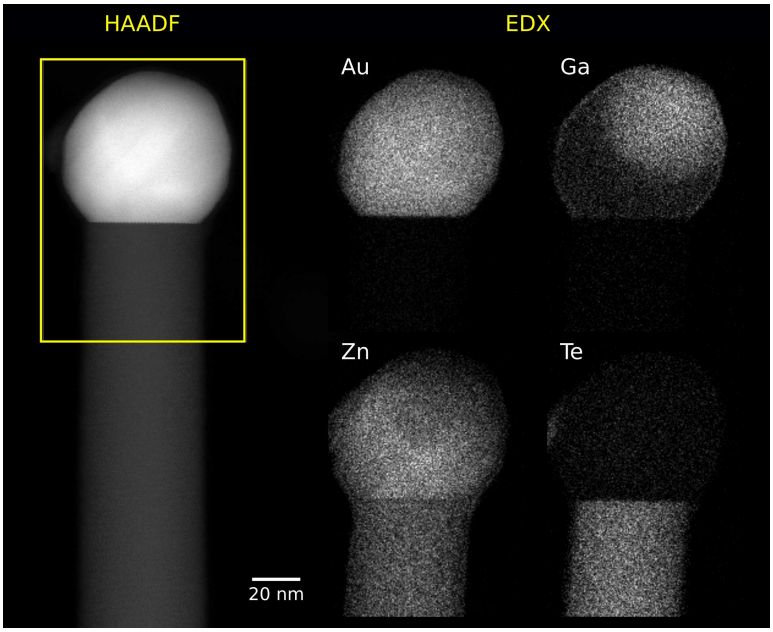

Figure 3.9: High angle annular darkfield (HAADF) image of a nanowire (left), together with elemental maps obtained by energy dispersive X-ray spectroscopy from the area marked by the yellow frame.

Crystal quality of the ZnTe nanowires

Generally, we observe a change in the surface roughness of the ZnTe nanowires along their entire length. In SEM images of samples such as shown in Fig. 3.6 the tip region appears smooth while the base of the nanowires becomes rough. E. Janik *et al.* [71] reported a high density of stacking faults for self-organized ZnTe nanowires that seems to be linked to a sawtooth-like appearance of the nanowire sides and reduces towards the tip of the nanowires. This raises the question whether or not the roughness observed in our nanowires is caused by lattice defects, which would impact the subsequent radial overgrowth, and if the crystal quality changes locally over the length of the nanowires. Therefore, nanowires grown at a substrate temperature of 440 °C have been prepared for TEM investigation. The results are shown in Fig. 3.10. The diffraction contrast is homogeneous along the entire length and comparable for different nanowires. This already indicates that the nanowires consist of a single crystal phase. High resolution imaging reveals a defect-free zinc blende crystal structure over the entire length (cf. insets in Fig. 3.10) and no signs of twin planes or polytypism, i.e., the formation of wurtzite segments in the zinc blende lattice that is often observed in VLS-grown nanowires. [72] Comparing the terminating side facets of tip and base, we find that the lower part consists mostly of the low-index $\{\bar{1}11\}$ and $\{\bar{1}00\}$ facets (marked in yellow), while the upper part exhibits $\{2\bar{1}\bar{1}\}$ facets (blue) parallel to the growth direction.

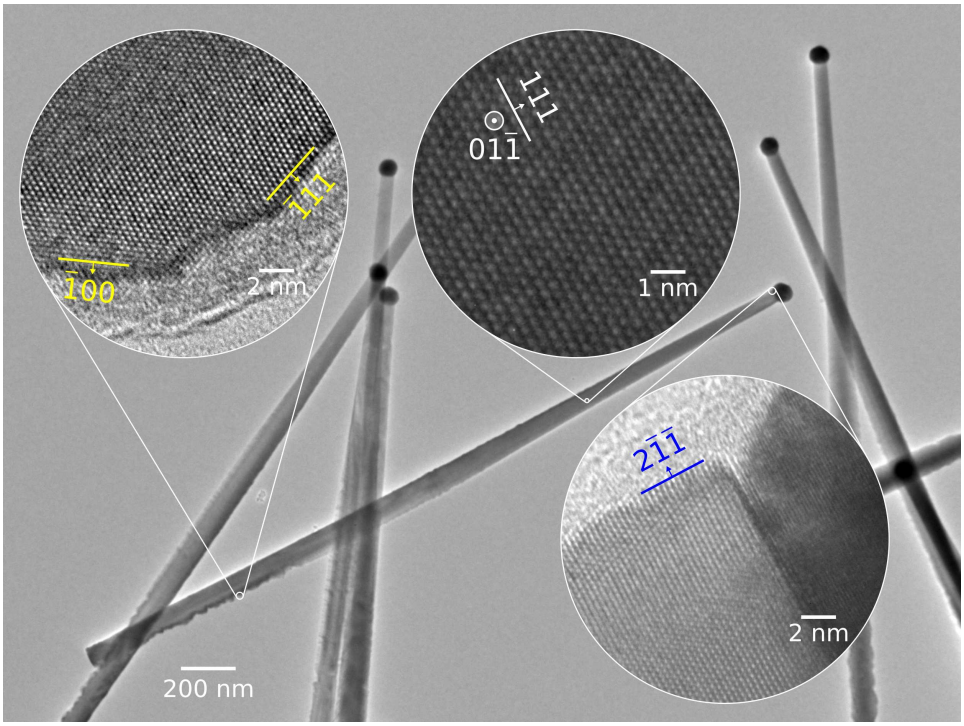

Figure 3.10: A transmission electron micrograph of ZnTe nanowires is shown together with high resolution insets recorded at different positions along one of the nanowires as indicated.

We relate this observation to the following fact: During growth, the base of the nanowires is exposed to the material flux for several hours. Therefore, the observed roughness in the vicinity of the nanowire base is explained by the formation of low-index microfacets due to a finite probability for the direct vapor–solid incorporation of adatoms on the nanowire sides, which is suppressed at a higher substrate temperature (cf. Fig. 3.7 in Section 3.2). Further, the thermal dissociation and redistribution of material throughout growth could also contribute to the observed faceting.

With these results, we finally can state that the ZnTe nanowires obtained by the novel selective area VLS-MBE technique are indeed perfectly suited for radial overgrowth with functional shells. Not only their geometrical morphology, characterized by a straight and essentially untapered shape with a high aspect ratio, but also their excellent crystal quality makes them a highly promising basis for HgTe nanowire heterostructures as an alternative to the previously investigated self-organized CdTe nanowires.

Chapter 4

Radial shell overgrowth

Semiconductor nanowires find increasingly application as a building block in quantum transport devices. For this, a precise control of the charge transport properties is crucial. Combining two or more material systems in a radial nanowire heterostructure offers a vast range of possibilities to engineer the band structure as desired. Here, we explore the fabrication of HgTe-based core–shell nanowires for the purpose of a charge transport investigation of a tubular quasi-one-dimensional topological insulator.

The growth of planar thinfilm heterostructures can be highly optimized for a particular surface orientation, while different orientations typically require different sets of growth parameters. Contrary, for the radial overgrowth of nanowires, the process has to be optimized for all side facets of the nanowire core at once. Finding a compromise for optimal overgrowth conditions on all sides is thus the main challenge.

The selective area grown ZnTe nanowire arrays exhibit ideal properties in order to template overgrowth with radial shells. However, the large lattice mismatch to HgTe requires a CdTe buffer shell, which is discussed in the first section of this chapter. The precision of the improved thermometry technique introduced in Chapter 2, together with the high quality and sample-to-sample reproducibility of the ZnTe nanowire arrays discussed in Chapter 3, allows to investigate the kinetics of HgTe shell overgrowth in order to finally optimize its structural properties, which is the focus of the second section of this chapter.

4.1 CdTe buffer shells on ZnTe nanowires

The nanowires discussed in the previous chapters are optimized in order to template tubular HgTe shells. Our investigation shows that the ZnTe nanowire arrays are the most promising substrate for radial overgrowth, especially due to their exceptionally high crystal quality and their homogeneous and untapered shape. Thus, these nanowires are the preferred substrate for subsequent HgTe shells. However, the large lattice mismatch of about 5.7% [47] between ZnTe and HgTe can cause plastic relaxation via the formation of dislocations. These lattice defects might have an undesired effect on the charge transport characteristics of the HgTe shell, in particular on quantum interference experiments where the signal can easily be dominated by defect-induced universal conductance fluctuations. Separating the HgTe shell from the ZnTe core by a buffer layer could help to absorb the lattice mismatch induced defects in order to provide a mostly defect-free surface for epitaxial overgrowth. HgTe with a high crystal quality can be grown by MBE on CdTe. [12] Hence, we investigate how the side facets of the ZnTe nanowires can be overgrown with a homogeneous CdTe buffer shell. As discussed in Section 1.2 the magnitude of elastic strain relaxation in the radial core–shell geometry increases with increasing shell thickness; thus, lattice mismatch induced defects that occur at the ZnTe–CdTe interface can be expected to reduce throughout buffer overgrowth. A microscopical analysis of the crystal structure thus helps to estimate a feasible CdTe shell thickness in order to achieve a high surface quality for the epitaxial HgTe overgrowth.

CdTe shell growth on ZnTe nanowires

Contrary to vapor–liquid–solid growth of the nanowire core, the subsequent radial overgrowth is achieved by direct vapor–solid nucleation at a significantly lower substrate temperature. After ZnTe nanowire growth, the samples are cooled in Te flux down to a growth temperature of 300–330 °C, which is typical for CdTe thinfilms. Upon thermal equilibration for about 5–10 min, Cd flux is added in order to initiate the CdTe overgrowth. At this temperature the growth seed is solid, thus VLS growth is entirely suppressed. However, the solid Au–Ga droplet may still catalyze growth by the VSS mechanism, resulting in the formation of kinked structures at the nanowire tip, which are comparably small due to the strongly reduced growth rate of the VSS process and thus are not expected to affect the quality of the shell.

Figure 4.1 shows close-up electron micrographs of representative nanowires obtained for different growth temperatures and Cd : Te flux ratios. It is important to note that the samples of this growth series were grown with thermocouple thermometry only; thus, the exact substrate temperature has a rather large uncertainty. This may further come with variations in the

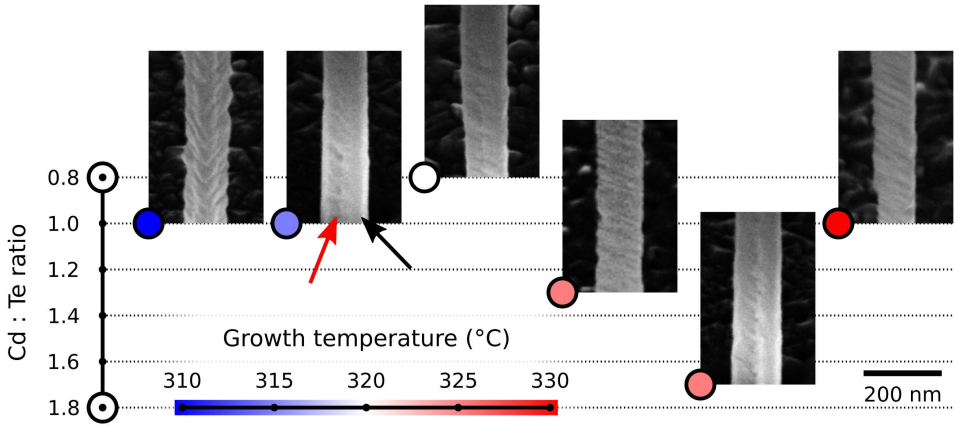

Figure 4.1: Electron micrographs of CdTe shells grown at different Cd : Te flux ratio (indicated by the vertical axis) and growth temperature T_{TC} (color-coded) on selective area grown ZnTe nanowires. Black and red arrows point out exemplary vertical facets of the CdTe shell that are referred to as "edge" and "side" of the more or less trigonal nanowires, respectively.

axial growth rate and the cross-sectional shape of the ZnTe core as discussed in Section 3.2 of the previous chapter, which can additionally affect the CdTe morphology. Hence, this growth series can only provide conclusions about general trends, rather than a precise set of growth parameters. Overall, Fig. 4.1 shows a rather homogeneous result throughout a wide range of growth parameters. Only for the lowest growth temperature of $T_{\mathrm{TC}} = 310\,^{\circ}\mathrm{C}$, we find a strongly increased surface roughness. A closer look indicates that especially for lower growth temperatures of 315–320 °C, or for a high Cd : Te ratio of 1.7, the CdTe shell is mostly flat close to the edges (cf. black arrow in Fig. 4.1) while the sides appear stepped (red arrow). This suggests the formation of different types of side facets during CdTe overgrowth.

The growth of HgTe depends strongly on the substrate orientation. Thus, it is important to characterize the crystallographic orientation of the side facets of the CdTe shell. In order to do so, we use a focussed ion beam to cut a cross-sectional lamella from an exemplary ZnTe–CdTe/HgTe nanowire for scanning transmission electron microscopy (STEM). This investigation was carried out by S. Wenner at the NORTEM facility in Trondheim, Norway, with financial support from the European Union Horizon 2020 research programme ESTEEM3. Figure 4.2(a) shows the resulting overview image of the entire nanowire cross-section together with a high resolution inset of the CdTe crystal lattice. The ZnTe core has a mostly circular cross-section with a slightly pointed shape towards the $\{11\bar{2}\}$A directions. The CdTe shell, however, does not exactly reproduce the shape of the core, but rather

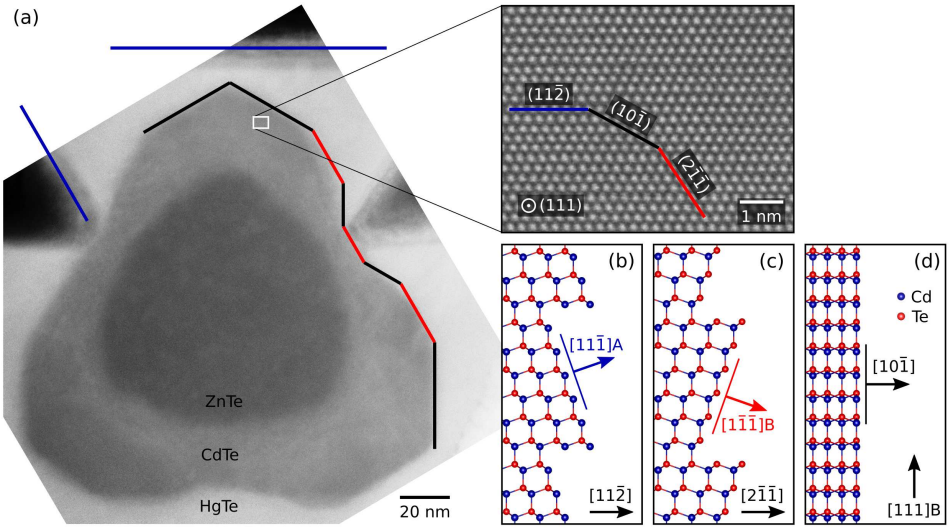

Figure 4.2: (a) Cross-sectional STEM image of a ZnTe–CdTe/HgTe core–multishell nanowire. The inset shows a higher magnification from within the CdTe shell. The main crystal facets are highlighted by lines. The line color indicates the surface polarity: blue – A-polar, red – B-polar and black – unpolar. (b)–(d) atomic model of the three different side facet types $\{11\bar{2}\}$A, $\{2\bar{1}\bar{1}\}$B and $\{10\bar{1}\}$.

develops a distinctly faceted surface. From the shape of the HgTe side facets we inferred in a previous study [19] that the main sides of the HgTe shell are $\{11\bar{2}\}$A-type [blue lines in Fig. 4.2(a)]. This allocation allows us to label the side facets of the CdTe shell, which correspond to $\{10\bar{1}\}$ (black lines) and $\{2\bar{1}\bar{1}\}$B-type (red lines) surfaces. $\{11\bar{2}\}$A and $\{2\bar{1}\bar{1}\}$B surfaces typically consist of the more stable microscopic A-polar $\{11\bar{1}\}$ and B-polar $\{1\bar{1}\bar{1}\}$ facets, respectively [cf. Fig. 4.2(b) and (c)], which can evolve to larger surface steps due to step bunching during overgrowth, [14] as sketched in Fig. 4.3. Contrary, the $\{10\bar{1}\}$ sides are unpolar and do not intrinsically exhibit surface steps as can be inferred from the atomic model in Fig. 4.2(d). This explains the observation of mostly flat facets close to the edges of the nanowires, while the sides show steps.

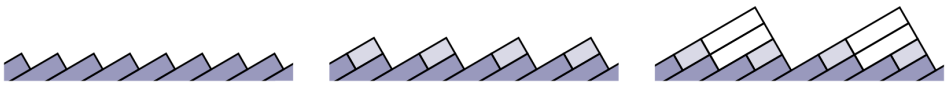

Figure 4.3: Illustration of step bunching during overgrowth of a micro-faceted surface (left to right), where the merging of microfacets leads to an increase of the facet size and a reduction in number.

Crystal quality and lattice mismatch induced defects

In order to characterize the crystal quality of the CdTe shell, we further analyze a cross-sectional lamella of a ZnTe–CdTe/HgTe core–multishell nanowire with (S)TEM. The results are shown in Fig. 4.4. In the large-aperture electron diffraction pattern shown in Fig. 4.4(a) we observe two sets of diffraction spots originating from two distinct lattice constants. The outer diffraction spots (marked in yellow) result from the ZnTe core, while the inner ones (marked in red) – corresponding to a larger lattice constant – can be attributed to CdTe and HgTe, which are not individually resolved due to their small lattice mismatch. The clear separation between the two sets of diffraction spots indicates relaxation between core and shell. A detailed look at the atomic lattice at the ZnTe–CdTe interface in Fig. 4.4(b) shows that the crystal is strongly distorted in the inner region of the CdTe shell. Further away from the interface in the outer part of the CdTe shell, however, we observe a high crystal quality as shown in Fig. 4.4(c). This already suggests that the strain-induced dislocations and defects in the CdTe shell reduce further away from the nanowire core, which allows us to prepare a CdTe surface with a high crystal quality for subsequent HgTe overgrowth.

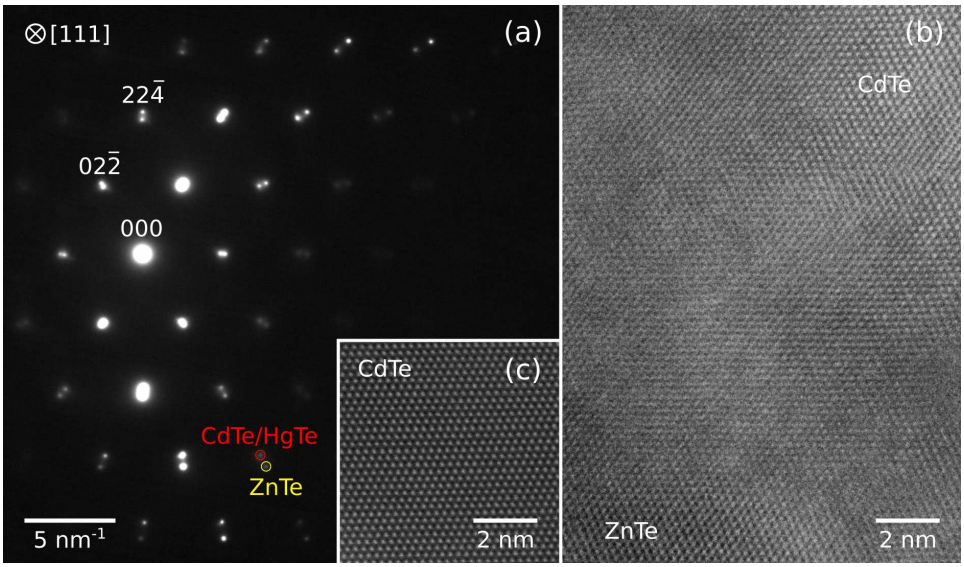

Figure 4.4: Transmission electron micrographs obtained from a ZnTe–CdTe/HgTe core–multishell nanowire. (a) Electron diffraction pattern of the entire nanowire cross-section, and STEM images obtained from (b) the ZnTe–CdTe interface and (c) the outer part of the CdTe shell.

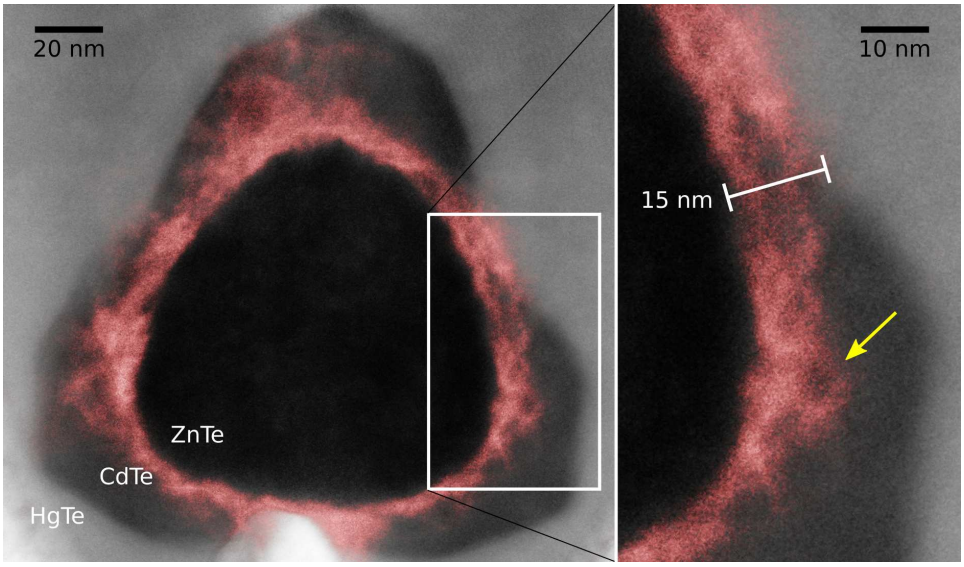

Figure 4.5: HAADF STEM image of a ZnTe–CdTe/HgTe core–multishell nanowire overlayed with the false-colored LAADF signal (red) obtained from the same spot. The arrow points out an exemplary dislocation line.

The density of dislocation defects reduces with an increasing CdTe buffer shell thickness. However, the amount of radial overgrowth is limited, on the one hand by layer growth on the substrate between the nanowires which buries the base of the nanowires over time and thus reduces the effective length, on the other hand by the total circumference of the final nanowire heterostructure that should stay well below the phase coherence length of electrons in the subsequent HgTe shell in order to retain the quasi–one–dimensional properties of the system. Hence, a more quantitative characterization of the defect distribution in the CdTe shell is important in order to estimate a reasonable compromize for the shell thickness. Low angle annular darkfield (LAADF) microscopy is a technique that is very sensitive to the dechanneling of the electron beam in a STEM measurement. Thus, it highlights defect-rich areas in an otherwise defect-free crystal already at low magnification, which can be used to acquire a general overview of the defect distribution across the entire nanowire. Figure 4.5 shows an overlay STEM image of a ZnTe–CdTe/HgTe radial nanowire heterostructure that combines material contrast (grayscale background image) obtained from a HAADF detector with the false-colored LAADF signal (red) on top. Within the ZnTe core we find a very low LAADF contrast, which matches the observation of essentially defect-free ZnTe nanowires discussed in Chapter 3. Directly at the ZnTe–CdTe interface the contrast increases significantly and remains high within about the first 15 nm of the CdTe shell (cf. inset in Fig. 4.5). In this region, one can clearly

see dislocation lines extending transversally away from the nanowire core, as pointed out by the arrow. Up to a shell thickness of about 30 nm, most of the dislocation lines appear to intersect and annihilate. Beyond that, the LAADF contrast is low and shows mostly spot-like features rather than clear dislocation lines. Thus we conclude, that already with a CdTe shell thickness of about 30–40 nm we achieve the suppression of a large amount of the strain-induced dislocations, which helps to significantly improve the crystal quality of the nanowire surface for the subsequent HgTe overgrowth.

Optimized CdTe overgrowth

Based on the previous studies of the morphology and crystallography in this chapter, we now focus on the optimization of the CdTe shell as a substrate for HgTe nanowire charge transport devices. The observation that stable $\{10\bar{1}\}$ facets can evolve during CdTe overgrowth (cf. Fig. 4.2) in addition to the main $\{2\bar{1}\bar{1}\}$B side facets of the ZnTe core is intriguing: Contrary to the stepped $\{2\bar{1}\bar{1}\}$B surfaces, $\{10\bar{1}\}$ facets are intrinsically flat. Combined with the straight and untapered shape of the ZnTe core, this could allow for a particularly homogeneous cross-section along the nanowire, which is important for quantum interference experiments. Thus, we explore how CdTe overgrowth can be influenced in order to achieve nanowire sides composed of only $\{10\bar{1}\}$ facets.

From the growth parameter series in Fig. 4.1 we can infer the presence of smooth $\{10\bar{1}\}$ facets – such as highlighted by the black arrow – at low to intermediate growth temperatures, as well as for a high Cd : Te ratio. In order to enhance the stability of these facets we thus use an increased Cd : Te ratio

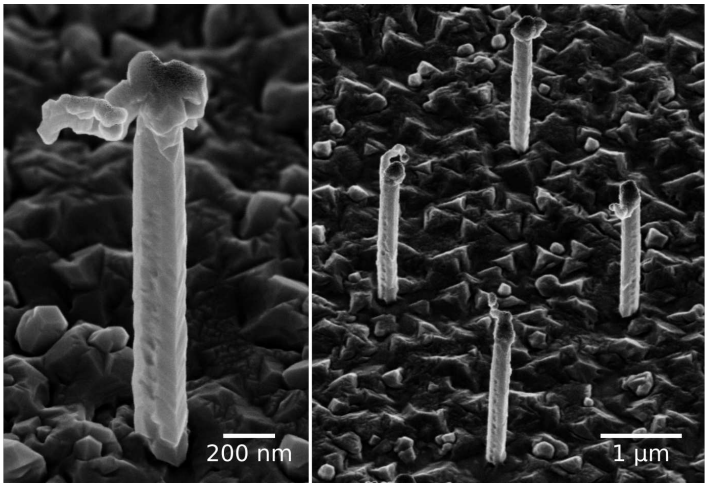

Figure 4.6: ZnTe nanowires overgrown for 45 min with a CdTe shell at a growth temperature $T_{BE} = 315\,^{\circ}\mathrm{C}$ and a Cd : Te ratio of about 2.

of about 2 at a rather low substrate temperature of $T_{\mathrm{BE}} = 315\,^{\circ}\mathrm{C}$. Further, a fully hexagonal cross-section composed of only $\{10\bar{1}\}$ facets likely requires a long overgrowth time on the $\{2\bar{1}\bar{1}\}$B sides of a trigonal ZnTe core. The resulting increased thickness of the CdTe shell comes with the additional benefit of providing more spatial separation between the defective ZnTe–CdTe interface and the subsequent HgTe shell. The electron micrograph of ZnTe nanowires overgrown for 45 min with optimized growth parameters for the CdTe shell, Fig. 4.6, shows that the desired result of smooth and basically untapered CdTe overgrowth can indeed be achieved. It should be noted, that the increased overgrowth time also leads to a more pronounced VSS growth of CdTe triggered by the solidified Au–Ge droplet (the kinked structure at the nanowire tip). However, we do not expect a noticeable negative influence of this structure on subsequent radial overgrowth. Thus, with a constant diameter of about 200 nm along the entire length of about 2 µm the ZnTe–CdTe core–shell nanowires are the ideal basis for HgTe nanowire heterostructures for transport investigations that place high demands on the homogeneity of the cross-sectional shape.

4.2 Epitaxial overgrowth with HgTe

Previous work demonstrated the molecular beam epitaxy of HgTe shells on self-organized CdTe nanowires in a narrow range of growth parameters. [14,19] The morphology of the HgTe shell is characterized by a trigonal shape with a pronounced faceting of the surface on $\{11\bar{2}\}$A sides and a tendency for the formation of gaps on the $\{2\bar{1}\bar{1}\}$B sides of the nanowires. However, further optimization towards a reliable overgrowth with a smooth and closed HgTe shell has so far been severely obstructed by the low precision of thermocouple-based thermometry, which limited the reproducibility of the CdTe core as well as the controllability of HgTe overgrowth. The well-controlled fabrication of homogeneous ZnTe–CdTe core–shell nanowire arrays combined with the high precision of band edge thermometry even at low substrate temperatures presented in the previous chapters allows us now to investigate in detail the radial overgrowth of nanowires with HgTe.

In the following, we explore how the morphology of the HgTe shell can be influenced in order to achieve homogeneous overgrowth on all nanowire sides, and to prevent faceting of the nanowire sides as a result of step flow growth. Finally, we discuss the crystal quality of the HgTe shell and the distribution of strain at the CdTe–HgTe interface.

HgTe growth within the step flow regime and beyond

Ideally, HgTe would overgrow all side facets of the nanowire core homogeneously. However, the growth rate and morphology of HgTe epilayers depend strongly on the substrate orientation. One of the main reasons for this is the condensation coefficient of Hg, which was found to be significantly higher on B-terminated (111) or (112) substrates compared to A- or unpolar surfaces. [37] This makes homogeneous overgrowth on all sides of the nanowires challenging, and requires a compromize to be found for the Hg : Te ratio that yields comparable growth on all different side facets. Further, for the molecular beam epitaxy of (001) HgTe layers a step flow growth regime is observed at the typical growth temperatures around $T_{\mathrm{TC}} = 180\,^{\circ}\mathrm{C}$, which is characterized by the formation of atomically flat terraces of a size determined by the adatom diffusion length. [73] This allows to achieve flat surfaces with a very low surface roughness as long as the direction of step flow is oriented parallel to the substrate surface. However, for the HgTe overgrowth of CdTe nanowires we find that the main direction of step flow points along $\{11\bar{1}\}$A facets, which are tilted by an angle of about 19.5° to the growth axis. Step flow overgrowth on these microscopical $\{11\bar{1}\}$A facets leads to step-bunching, where adjacent facets merge and form large tilted surface steps on the $\{11\bar{2}\}$A-sides of the nanowires as sketched in Fig. 4.3. [14] The resulting inhomogeneous cross-section along the nanowire might make the

observation of interference-based charge transport effects such as Aharonov–Bohm oscillations challenging. By suppressing the step flow mechanism, one can expect to reduce the formation of surface steps to some degree, and thus obtain a smoother surface morphology of the HgTe shell.

Fundamental for the step flow growth regime is a low probability for the formation of adatom clusters, preventing island growth, and a high probability of nucleation at the step edges of the substrate. This is typically realized within a growth temperature window where the energy of adatoms is sufficient for a high diffusion length on the atomically flat substrate, but less than the potential barrier of a step edge, the so-called Ehrlich–Schwoebel barrier. [74, 75] Increasing the substrate temperature would allow adatoms to overcome the Ehrlich–Schwoebel barrier and be less efficiently trapped at step edges, which can be expected to result in a more homogeneous overgrowth.

In order to test whether the formation of $\{11\bar{1}\}$A facets can indeed be suppressed at a higher substrate temperature we fabricated a series of HgTe nanowire shells at increasing substrate temperatures close to the high-temperature limit of HgTe growth. A Hg : Te ratio of 230 is chosen, which lies between the optimal values for growth on the different kinds of substrate orientations. Figure 4.7 shows the results. For a substrate temperature of

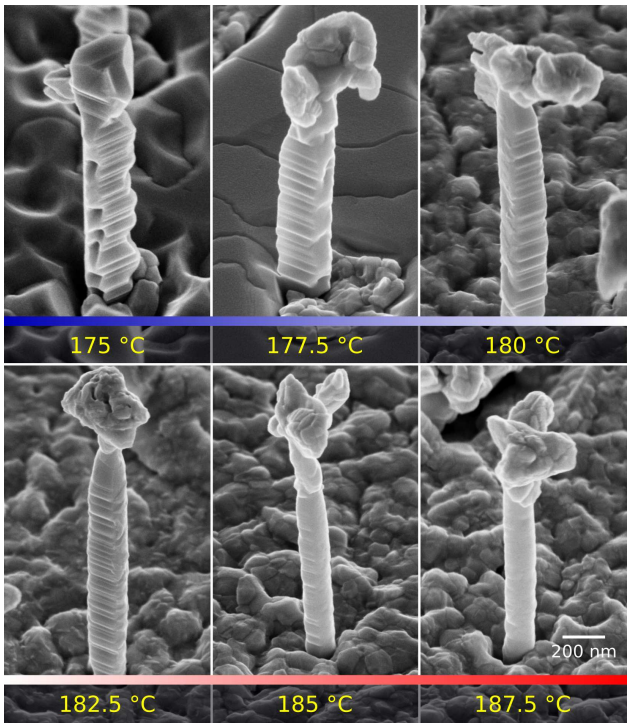

Figure 4.7: Electron micrographs of HgTe nanowire shells grown with a Hg : Te ratio of 230 at different substrate temperatures as denoted.

$T_{\mathrm{BE}} = 175\,^{\circ}\mathrm{C}$ we observe a faceted trigonal morphology with gaps at the edges of the HgTe shell. At this temperature, the condensation coefficient of Hg is in general relatively high. Hg is most efficiently bound on B-polar surfaces. The resulting accumulation of a significant excess of Hg on the B-polar side facets of the nanowires possibly limits the amount of Te reaching the growth front, which can lead to the formation of gaps on these sides. [14] Step bunching during step flow overgrow of the microscopic $\{11\bar{1}\}$ facets of the A-polar nanowire sides can explain the pronounced surface steps. With increasing temperature, several changes can be observed: At 177.5 °C, the gaps in the HgTe shell close while the overall shell thickness remains approximately the same. This can be explained by a reduced condensation coefficient of Hg with increasing temperature, which now allows to also form B-terminated side facets. The growth rate on the A-terminated sides, however, is mostly unaffected because at this temperature the condensation coefficient of Te can still be assumed as 1, and HgTe growth is typically limited by the supply of Te. [73] Increasing the growth temperature to 180 °C apparently begins to affect the nanowire diameter. From this, one can conclude that the surface desorption of Te sets in, which effectively limits the supply of Te and lowers the axial growth rate of the HgTe shell. Additionally, for even higher temperatures (182.5–185 °C) the size of the surface steps starts to decrease until smooth radial overgrowth is finally achieved at 187.5 °C. At this temperature, the kinetic energy of the Te adatoms is eventually high enough to overcome the Ehrlich–Schwoebel barrier and to be less efficiently trapped by step edges, which can explain the successful suppression of surface steps at these high substrate temperatures. Based on the conclusions obtained from this temperature series we can now adjust the growth parameters accordingly to achieve the shell morphology desired for charge transport investigations.

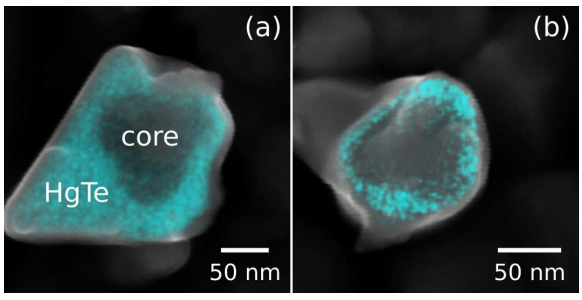

Figure 4.8: Electron micrographs of the cross-sectional surface of HgTe nanowire shells grown at (a) 177.5 °C and (b) 185 °C. The background image was acquired with an InLens secondary electron detector, the overlayed false-color image data giving material contrast between the ZnTe–CdTe core and the HgTe shell was obtained with an EsB backscattered electron detector.

Energy selective backscattered electron (EsB) imaging allows to obtain a clear material contrast between the HgTe shell and the ZnTe–CdTe core by means of scanning electron microscopy. Thus, it can be used to quantify the thickness of the HgTe shell in order to calculate the growth rate. Figures 4.8 (a) and (b) show electron micrographs of two exemplary nanowires which were overgrown with HgTe for 30 min at 177.5 °C and 185 °C (upper and lower central images in Fig. 4.7), respectively, with the simultaneously acquired material-sensitive EsB data from the cross-sectional surface overlaid in false-color. For the lower growth temperature, Fig. 4.8(a), we infer a growth rate of about 1.0 nm/min on the A-sides of the nanowires. Overgrowth on the B-sides varies between about 4.3 and 0.7 nm/min, depending whether or not the adjacent flat A-sides merge and form a sharp edge. At the higher substrate temperature, Fig. 4.8(b), the HgTe growth rate is rather homogeneous with about 0.5 and 0.7 nm/min on A- and B-sides, respectively. The overall reduced growth rate for the higher substrate temperature can in principle be compensated by a longer growth time.

Crystal quality and strain in HgTe shells

Radial nanowire heterostructures are characterized by an especially efficient elastic relaxation of strain (cf. Section 1.2). Theoretical calculations suggest, that below a critical nanowire core radius of about 400 nm an infinitely thick shell with a lattice mismatch of 0.3% (as between CdTe and HgTe) can be grown without plastic relaxation at the interface. [31] With a typical core diameter of about 100–250 nm we thus expect a similarly high crystal quality of the HgTe shell compared to the CdTe below. This is confirmed by Fig. 4.9(a), which shows a transmission electron micrograph of the atomic lattice at the CdTe/HgTe interface of a ZnTe–CdTe/HgTe core–shell nanowire. Figure 4.9(b) shows the respective overview image. The absence of dislocations at the CdTe–HgTe interface in Fig. 4.9(a) indicates that the crystal quality of the HgTe shell is in principle determined by the nanowire core. We thus conclude, that HgTe nanowire shells with a very high crystal quality can be fabricated based on the ZnTe–CdTe core–shell nanowire arrays. Consequently, we can expect strain (i.e., a deformation of the unit cell) to be present in the crystal lattice of both HgTe and CdTe.

Strain in two-dimensional epilayers below the critical thickness for plastic relaxation is typically homogeneously distributed, because lattice mismatch-induced stress can only be released elastically in the direction of growth. Thus, integrative techniques such as electron or X-ray diffraction can be straightforwardly used to characterize strain in crystalline thinfilms. This is fundamentally different for lower-dimensional nanostructures, where the elastic release of stress is possible in all directions. In general, the result is an inhomogeneous spatial distribution of strain that requires high-resolution

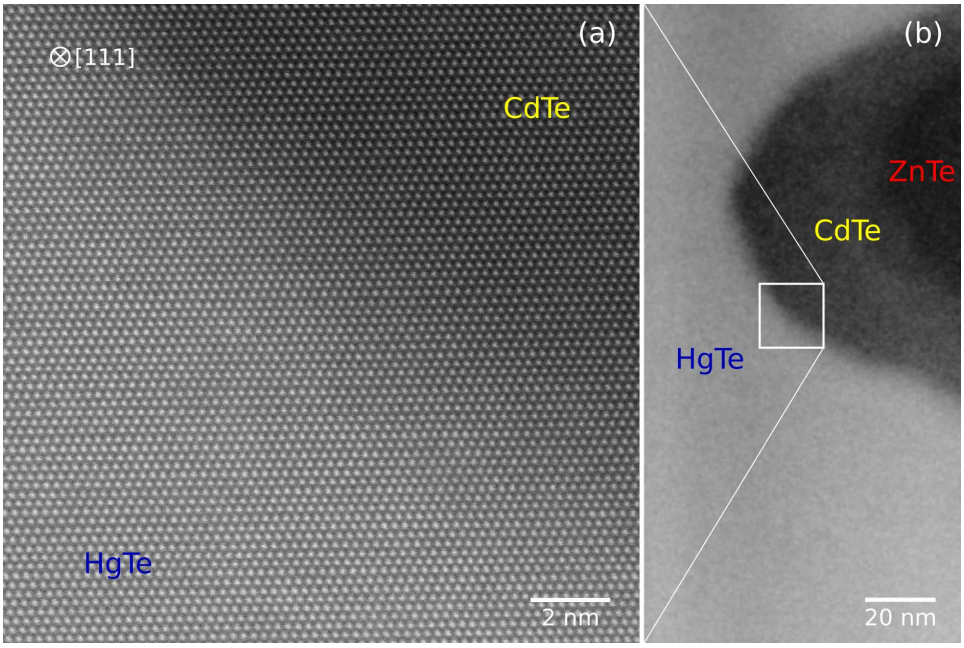

Figure 4.9: Transmission electron micrographs of a cross-sectional lamella from a ZnTe–CdTe/HgTe core–shell nanowire. The high resolution STEM image (a) was obtained at the position marked in the overview image shown in (b).

mapping. Transmission electron microscopy is so far the only method capable of resolving small amounts of strain with a very high spatial resolution. In the following, we present the main results of local strain mapping on the cross-sectional surface of CdTe–HgTe core–shell nanowires, and compare it to a previous experiment [17] that employed HR-XRD for an integrative strain measurement of an as-grown nanowire ensemble. For strain mapping we use the geometrical phase analysis (GPA), which is among the most established techniques for TEM-based strain measurements. From a high resolution real-space image of the crystal lattice, typically a HAADF STEM image, phase spectra are extracted by means of a selective inverse Fourier transform of a chosen area of one of the maxima in the Fourier transformed lattice image. These Fourier filtered phase images can then be used to calculate the displacement field, followed by numerical differentiation to obtain the strain tensors. A detailed mathematical description of this procedure is given by M. J. Hÿtch *et al.* [76]

The TEM data for the GPA investigation presented in Fig. 4.10 was acquired and processed by S. Wenner at the NORTEM facility in Trondheim, Norway. Figure 4.10(a) shows a high resolution HAADF STEM image of the cross-sectional core–shell interface of an exemplary CdTe–HgTe nanowire.

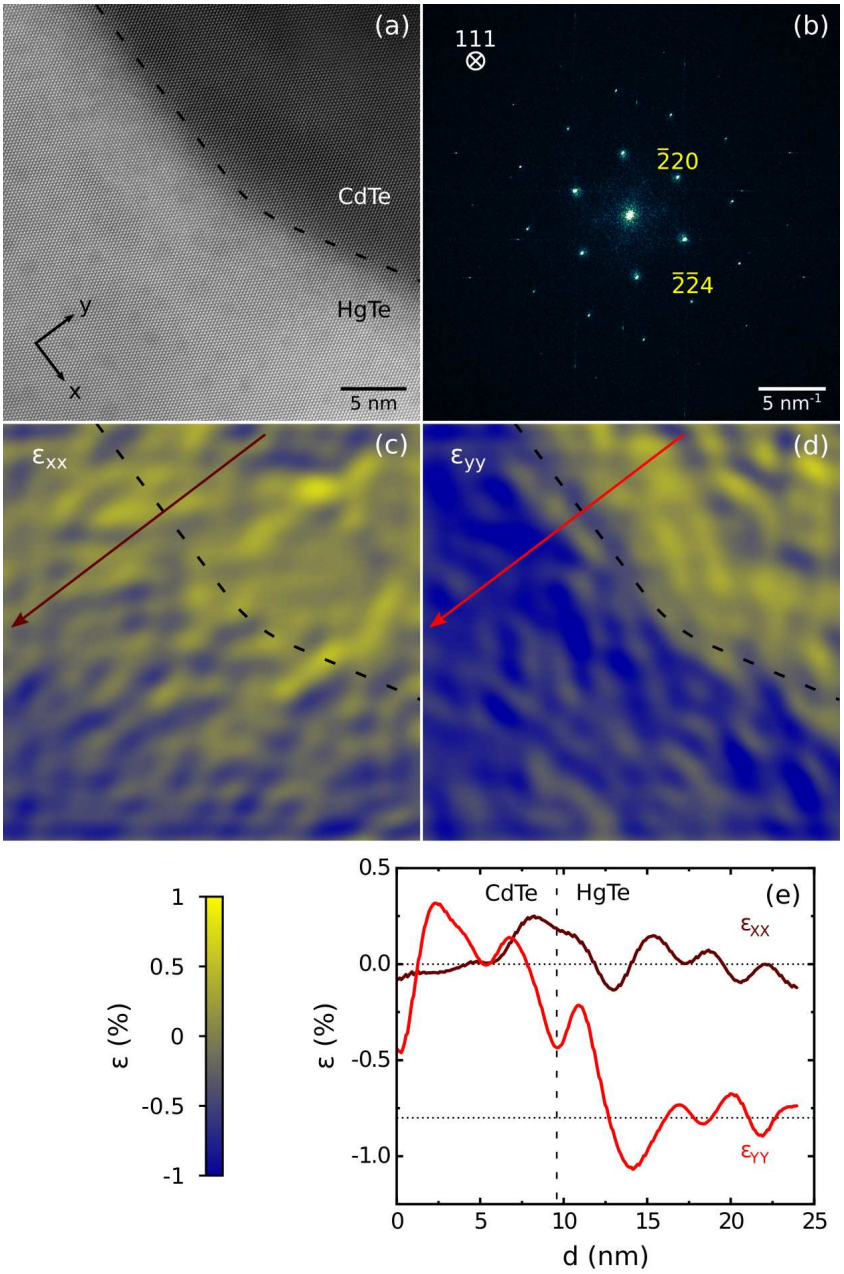

Figure 4.10: (a) Scan distortion and stage drift corrected HAADF STEM image of the atomic lattice at the core–shell interface of a CdTe–HgTe nanowire. (b) Fourier transform of the lattice image (a). (c)–(d) Color coded maps of the strain tensor components ε_{xx} and ε_{yy} obtained from a geometrical phase analysis of (a). The dashed line in the images indicates the approximate position of the interface. (e) Line profile of strain ε along the arrows in images (c)–(d). Dotted horizontal lines are a guide to the eye.

The GPA places high demands on the imaging precision; thus, the image is corrected for stage drift as well as for scan distortion and includes only a relatively small field of view of about $30 \times 30\,\mathrm{nm}^2$. The power spectrum of the lattice image, Fig. 4.10(b), is obtained by Fourier transformation. The color coded strain maps in Figs. 4.10(c) and (d) show the strain tensor components ε_{xx} and ε_{yy} parallel and perpendicular to the $[1\bar{1}0]$-oriented upper left part of the interface, respectively. It is important to note, that here the strain components on both the CdTe- and the HgTe-side of the interface are normalized with respect to an area within the CdTe. Thus, the contrast in the ε_{xx} and ε_{yy} maps has to be interpreted as a relative change in the lattice constant, and not as the absolute value of strain which would require normalization to the intrinsic bulk lattice constant of the respective material instead. For the perpendicular ("out-of-plane" with respect to the respective interface area) component ε_{yy} we find a clear contrast change in close proximity to the CdTe–HgTe interface [Fig. 4.10(d)], whereas the parallel "in-plane" component ε_{xx} remains approximately constant within the level of background fluctuations [Fig. 4.10(c)]. This observation is further corroborated by a line profile, Fig. 4.10(e), acquired along the position of the arrow in the strain maps. The fact, that basically no change in the relative in-plane lattice constant is observed over the length of about 25 nm across the CdTe–HgTe interface indicates pseudomorphic overgrowth and – following from the by about 0.3% smaller intrinsic bulk lattice constant of HgTe – the presence of a significant amount of tensile strain in the HgTe shell parallel to the interface even in the core–shell nanowire geometry. The expected corresponding out-of-plane compressive response shows up as a change in the relative lattice constant by about -0.8% perpendicular to the interface [cf. dotted guidelines in Fig. 4.10(e)]. Repeating this analysis for the $[1\bar{2}1]$-oriented right part of the interface, as well as for a different nanowire, gives very similar results both qualitatively and quantitatively as can be inferred from Fig. D.1 in the Appendix D.

We now compare this observation to the HR-XRD based strain investigation of CdTe–HgTe nanowire heterostructures by M. Kessel *et al.* [17] Figure 4.11 shows the main result of this study. It should be pointed out that the samples investigated there are CdTe nanowires grown tilted on a (110)-oriented substrate, which are overgrown with a partial HgTe shell that covers only the upper $(11\bar{2})$A side of the nanowire facing the material beam [cf. Figs. 4.11(a)–(b)]. This is in contrast to the tubular core–shell geometry investigated here. Figure 4.11(c) shows the relative change in the lattice constant of core and shell. An average in-plane stretch along the [111] growth direction of about 0.03% was found in the ensemble of HgTe partial shells while the CdTe lattice showed compression by $\sim 0.05\%$. Furthermore, the results obtained from several diffraction reflexes with different angles to the [111] direction suggest the presence of shear strain which causes a monoclinic

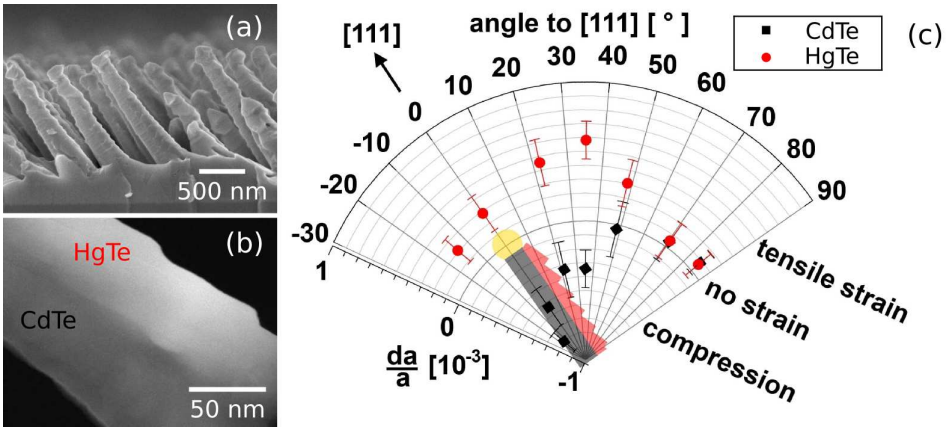

Figure 4.11: (a) Electron micrograph of CdTe–HgTe core–shell nanowires grown on a (110)-oriented substrate, view angle is parallel to the substrate plane. (b) Transmission electron micrograph of a longitudinal cut through a nanowire from the same sample. (c) Relative changes in the lattice constant da/a of core and shell acquired by HR-XRD for various reflexes with a given angle to the [111] growth direction. Images and graph are adapted from M. Kessel *et al.* [17]

distortion of the unit cell with a stretch along the vertical [110] direction at an angle of about 35°. The origin of the shear strain was attributed to the microscopic surface steps of the $\{11\bar{2}\}$A sides of the nanowire core. Hence, residual strain in the HgTe shell has been detected with both the local TEM-based technique and the integrative HR-XRD investigation. However, the amount of strain determined by either of these methods differs by roughly an order of magnitude. This apparent discrepancy can possibly be explained by several contributing factors: First, in contrast to the integrative HR-XRD measurement the TEM-based analysis investigates strain only within a range of about 30 nm around the heterointerface. While this field of view is sufficient to draw conclusions about the inner surface area, and even partially the bulk of the HgTe shell, the outer part where the crystal lattice is expected to be most relaxed is not included. Hence, the average amount of strain in the heterostructures is likely smaller than the result of the TEM-based GPA. Second, an integrative investigation averages over all nanowires from a large ensemble, while only regular-shaped wires were picked for TEM investigation in a similar selection process as used for the preparation of the charge transport devices. Because strain can be efficiently released by irregularities in the crystal lattice such as twinning and dislocation defects, a variation of the crystal quality of nanowires on the same sample, as well as in between different samples, will influence the amount of residual strain observed. Depending on the crystal quality of the particular nanowire probed in TEM, this can in principle cause

deviations of the GPA result towards both higher and lower values from the ensemble average inferred from HR-XRD. And third, the partial shell geometry investigated in the HR-XRD-based experiment can be expected to offer a more efficient elastic strain release compared to a tubular shell due to its significantly smaller contact area on only one side of the CdTe core.

While the high surface–to–volume ratio of the nanowire geometry can already help to gain enough signal from the surface states in charge transport investigations to be observable even with finite bulk conductivity, [77] an insulating bulk is nonetheless advantageous, especially for the interpretation of complex transport experiments that are based on the topological properties of the system. Strain is known to lift the degeneracy of bulk bands in HgTe, [41] which opens a bandgap in the electronic bulk states that is typically of the order of 10 meV. [78] It was shown, that this is sufficient to transform the intrinsic semimetal HgTe into a three-dimensional topological insulator at cryogenic temperatures, for which charge transport is governed solely by the surface states. [12,79,80] Thus, the observation of tensile strain on both $\{10\bar{1}\}$-type and $\{2\bar{1}\bar{1}\}$B-type facets, the main side facets of the nanowire core, is an important result that might eventually be linked to a bulk bandgap in our nanowires. In order to investigate whether or not this is the case, the second part of this work is devoted to the characterization of these optimized core–shell nanowires in charge transport.

Overview of Part I

Part I of this thesis discusses the MBE growth of core–shell nanowires in the (Hg,Cd,Zn)Te material system. The purpose of this investigation is to provide a reliable fabrication process for strained HgTe nanowire shells with a high crystal quality and a homogeneous tubular morphology for charge transport investigation. This we successfully achieve through several significant advancements in the fabrication of both the nanowire core and the subsequent radial overgrowth, as summarized in the following.

The substrate temperature is the most critical parameter for the fabrication of CdTe nanowires by MBE. The narrow growth temperature window of the order of 1 °C is below the precision of the commonly used thermocouple-based thermometry system. Thus, we discuss in Section 2.1 the implementation of an alternate temperature monitor based on the temperature dependent shift of the band edge in the absorption spectrum of the semiconductor substrate. This technique proves to be highly successful and allows to achieve reproducible growth of CdTe nanowires despite of the exceptionally narrow temperature window. Moreover, its high precision is of fundamental importance later on for the optimization of ZnTe nanowires as an alternative nanowire core, as well as for the subsequent HgTe shell overgrowth.

In Section 2.2 we investigate the structural properties of the CdTe nanowires. With an average diameter of 40–80 nm and a length of $\sim 2\,\mu$m, they are in principle well suited as the core for our radial nanowire heterostructures. However, the nucleation of adatoms on the nanowire sides during VLS growth leads to a pronouncedly tapered shape, which results in an inhomogeneous cross-section that could impede the investigation of quantum interference in the electronic states. Further, transmission electron micrographs indicate a strong tendency for the formation of planar dislocations, which affects also the crystal quality of the subsequent HgTe shell.

Hence, Section 3.1 investigates ZnTe as an alternative material for the nanowire core, which offers a significantly larger growth temperature window and, linked to that, a better control over the morphology and crystal quality. Further, instead of the common self-organized formation of the VLS growth seed, a selective area process is developed that brings full control over the position of the individual nanowires, which allows for a significantly more

homogeneous surrounding during subsequent overgrowth. For this purpose, an array of Au disks is patterned by electron beam lithography on ZnTe substrate. Supplied with the right amount of Ga, the Au disks form eutectic Au–Ga droplets at the defined positions, which – after an adequate surface cleaning – catalyze the growth of uniform ZnTe nanowire arrays.

The precise control of the growth parameters in combination with the reliable position controlled growth process allows us to get a better understanding of the growth kinetics for the ZnTe core, which is the focus of Section 3.2. It turns out, that the substrate temperature, i.e., the kinetic energy of the adatoms, is the most crucial parameter to adjust between a high axial growth rate and vertical yield at lower temperature, and a more circular cross-section, which is ideal for subsequent shell overgrowth, at higher. In addition, the study of competitional effects in dense nanowire arrays allows to define a minimum pitch distance of the order of 1 µm between adjacent nanowires in order to ensure that vapor–liquid–solid nucleation is limited only by adatom diffusion, which makes the growth significantly more stable.

The structural properties of the optimized ZnTe nanowires are investigated in Section 3.3. The nanowires show a very high ensemble uniformity and an essentially untapered shape with a diameter of about 50 nm and a typical length of about 3 µm. Further, an excellent crystal quality is confirmed by a transmission electron microscopy study. This makes the ZnTe nanowire arrays the ideal basis for high-quality core–shell heterostructures.

In order to avoid interfacial dislocations due to the large lattice mismatch between ZnTe and HgTe, we investigate in Section 4.1 the overgrowth of the ZnTe nanowires with a CdTe buffer shell. We find, that the enhanced stress relaxation in the core–shell geometry leads to an efficient reduction of the misfit dislocation lines density away from the interface. Thus, a high crystal quality at the surface can be achieved even with a moderate CdTe buffer thickness of about 30–40 nm. Further, a detailed study of the crystal facets that develop during CdTe overgrowth allowed to optimize the growth parameters in order to achieve a smooth and regular morphology of the nanowire sides.

Section 4.2 finally discusses the optimization of the HgTe shell. The substrate temperature strongly influences the interplay between the condensation coefficients of Hg and Te, as well as the efficiency of adatom trapping at crystal step edges. This we use to adjust the morphology of overgrowth between a stepped surface consisting of stable low-indexed microfacets, and a homogeneous and smooth overall shape at high substrate temperatures. A detailed transmission electron microscopy study shows that the resulting HgTe shells have a very high crystal quality and an epitaxial relation to the CdTe below, and a geometric phase analysis indicates a significant amount of elastic strain at the CdTe–HgTe interface.

Part II

Quantum transport in tubular HgTe core–shell nanowire heterostructures

Chapter 5

Introduction to charge transport in HgTe nanowires

Contrary to the discrete energy levels of electrons in an isolated atom, electronic states in a solid-state system are described by energy bands. Charge transport through a material is thus governed by its band structure, which for a topological insulator is well known: The bulk material has an insulating band gap, whereas the surface states are characterized by a gapless linear energy dispersion with a strong coupling between the electron spin and momentum. The scientific interest for topological insulators is mostly tied to the non-trivial properties of their surface states. Charge carriers in these states are protected against backscattering, which implies dissipationless transport with an intrinsically quantized conductance as a realization of the quantum spin Hall effect. [81] *Furthermore, with superconducting pair correlations induced by the proximity effect, the surface states of a topological insulator are predicted to host Majorana bound states, which are zero-energy excitations that obey non-Abelian exchange statistics and have thus potential application in quantum computation.* [82]

In this chapter, we first discuss the effect of quantum confinement introduced by the nanowire geometry on the topological band structure. For this we impose periodic boundary conditions for the surface state along the nanowire perimeter. Subsequently, we summarize the current state of research on charge transport through HgTe nanowires.

5.1 Energy dispersion of a topological insulator nanowire

The characteristics of electron transport through a material are governed by its energy dispersion relation $E(\vec{k})$. Thus, a basic knowledge of the dispersion of a topological insulator nanowire – the focus of this chapter – is fundamental for the understanding of the subsequent experimental transport investigations.

The origin of the topological properties of HgTe lies in the energetic inversion of the Γ_6 and Γ_8 bands. [81] This band order is reversed at the interface to a trivial insulator, which gives rise to a gapless surface state with a linear dispersion at the Γ-point of the Brillouin zone. A three-dimensional topological insulator has a two-dimensional surface, hence the dispersion of the surface state

$$E(\vec{k}) \propto \sqrt{k_\mathrm{x}^2 + k_\mathrm{y}^2} \tag{5.1}$$

is also two-dimensional, i.e., cone-shaped, with the wave vector k_z perpendicular to the surface being zero. Electrons in the surface state are described by the Dirac equation for a massless spin-1/2 fermion, thus this dispersion relation is often referred to as the Dirac cone. Intrinsically a semimetal, HgTe becomes a bulk insulator under applied tensile strain, which opens an energy gap of the order of 10 meV at the Fermi energy between the light- and heavy-hole Γ_8 bulk bands. [12] At low temperature, charge transport in three-dimensional HgTe is therefore clearly dominated by the surface states. [12] Reducing the dimensionality of a topological insulator to the nanowire geometry influences the band structure of these surface states. Based on theoretical work by J. H. Bardarson *et al.* [83] we discuss in the following a basic model to describe charge transport through a topological insulator nanowire.

Dispersion relation of the nanowire surface states

A tubular topological insulator nanowire can be understood as a three-dimensional thinfilm that is wrapped up to a cylindrical geometry as sketched in Fig. 5.1. Surface states, indicated in yellow in Fig. 5.1, are then located at

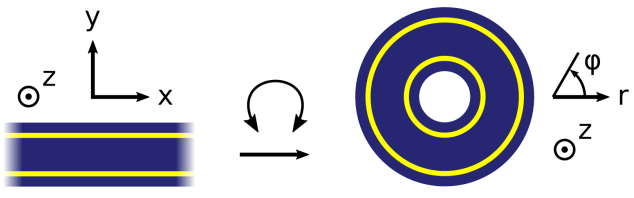

Figure 5.1: Illustration of the morphological transition from a bulk topological insulator thinfilm (left) to a tubular nanowire geometry (right). Both structures are assumed to be infinitely elongated along z.

the inner and outer surface of the structure. With a transformation of the coordinate system from carthesian (x, y, z) to cylindrical (r, φ, z), inner and outer surface state can each be described from a mathematical point of view by introducing the periodic boundary condition

$$\psi(r, \varphi) = \psi(r, \varphi + C) \cdot e^{i\phi} \tag{5.2}$$

for electron wave functions along the tangential direction φ. This leads to a quantization of the energy spectrum with respect to the angular component k_φ of the wave vector as long as the phase coherence length is significantly larger than the circumference C of the respective surface state. Upon a full rotation along φ, the electron picks up a phase ϕ that in general can consist of several components as discussed in the following.

The first phase component to consider is the Berry phase, [84] which has a finite value when an adiabatic change along a closed loop in the parameter space of a non-trivial system does not bring it back to the original state. In particular, the full rotation of a spin-$^1/_2$ particle along a closed trajectory in a system with strong spin–orbit coupling – such as the surface states of a topological insulator – results in an antiperiodic boundary condition expressed as a phase factor of π. [85] As a consequence, the quantized angular component of the wave vector k_φ is shifted from integer to half-integer multiples of the quantization lengthscale $2\pi/C$, which prevents the existence of the perfectly

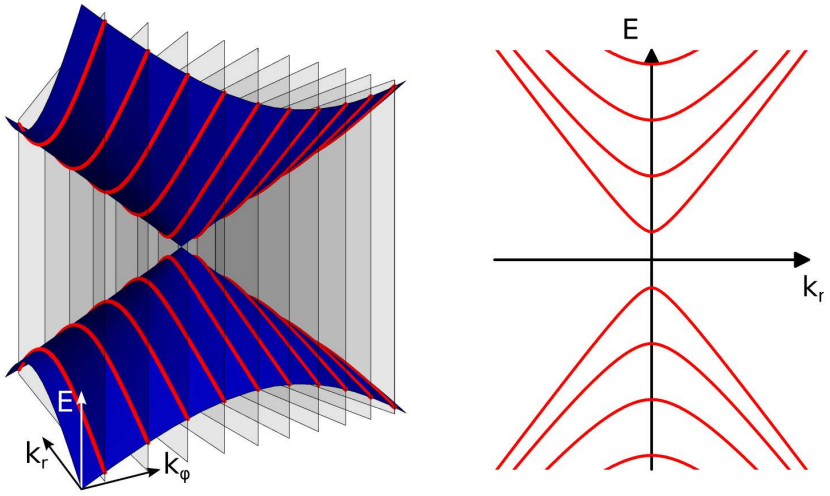

Figure 5.2: Basic model of the surface state energy dispersion (red) of a topological insulator nanowire in a three-dimensional (left-hand side) and projected two-dimensional (right-hand side) representation. Vertical planes indicate the quantization in k_φ, the Dirac cone of a three-dimensional topological insulator is depicted in blue.

transmitted gapless linear mode at $k_\varphi = 0$. Figure 5.2 illustrates how the resulting gapped quasi-one-dimensional surface state spectrum (red) emerges from the intersection of the Dirac cone of a three-dimensional topological insulator (blue) with parallel planes that resemble the quantization along k_φ introduced by the periodic boundary conditions of the nanowire geometry. It should be pointed out that this spectrum describes a single surface state. Hence, for the tubular nanowire geometry discussed in this work an additional set of bands with the respective inter-band spacing has to be taken into account.

The second phase component originates in the Aharonov–Bohm effect, [86] which describes that the wave function of an electron moving on a closed path penetrated by a magnetic flux Φ gains a phase of $2\pi \cdot \Phi/\Phi_0$, where $\Phi_0 = h/e$ is the magnetic flux quantum, h the Planck constant and e the elementary charge. When we combine the contribution of the Berry phase with the Aharonov–Bohm-related phase factor, the angular component of the wave vector takes discrete values of

$$k_\varphi = \left(n + \frac{1}{2} + \frac{\Phi}{\Phi_0}\right) \frac{2\pi}{C} \tag{5.3}$$

with $n \in \mathbb{Z}$. Thus, an external magnetic field with a homogeneous magnetic flux density $B_\parallel = \Phi/A$ applied in parallel to the nanowire, A being the area enclosed by the tubular electronic state in the shell, can be used to alter its band structure. Figure 5.3 shows the evolution of the surface state spectrum with magnetic flux. For integer multiples of Φ_0 (left-hand side) the zero-field case is realized with a gapped dispersion consisting of doubly degenerate bands, as in Fig. 5.2. With increasing magnetic flux, bands with opposite momentum (and spin) shift in opposite direction in energy, which lifts the degeneracy until adjacent bands overlap at half-integer multiples of Φ_0 (right-hand side). At this particular flux value, the Aharonov–Bohm phase

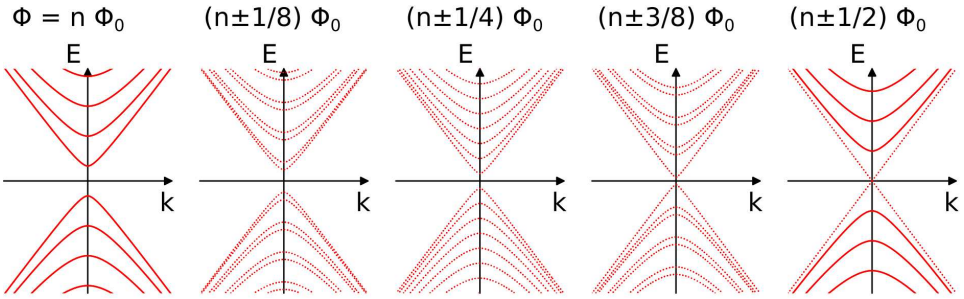

Figure 5.3: Schematic energy dispersion of a topological insulator nanowire for different values of magnetic flux Φ enclosed by the surface state, changing in steps of $\Phi_0/8$ from left to right. Solid lines indicate doubly degenerate bands, dotted lines are non-degenerate.

factor cancels the Berry phase, which allows to restore the gapless linear mode with $k_\varphi = 0$. This effectively means that the massless Dirac properties of the system can be switched on and off by changing the magnitude of an external magnetic field, which offers unique possibilities to investigate the influence of a topological band structure in various charge transport experiments. In general, apart from the Aharonov–Bohm effect additional geometric phase contributions, such as the Al'tshuler–Aronov–Spivak effect, [87] can occur. For simplicity these effects are not considered here, but will be addressed later on.

Relation to the bulk states

For an interpretation of charge transport results in the following chapters, the role of the bulk dispersion has to be considered in addition to the energy dispersion of the surface states. A qualitative overview can be obtained from the band structure of three-dimensional HgTe. Thus, we show in Fig. 5.4 the $\vec{k} \cdot \vec{p}$ simulation of the band structure of a HgTe thinfilm on top of a CdTe layer, both with a thickness of 40 nm, which is comparable to the typical shell thickness of our nanowire heterostructures. It should be pointed out that the calculation neither considers curvature effects nor periodic boundary conditions that would be necessary for a realistic description of the

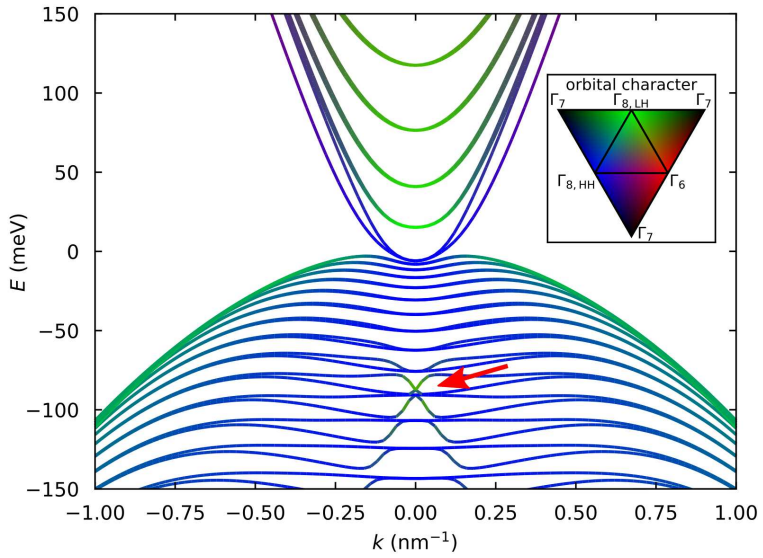

Figure 5.4: Simulated band structure of a 40 nm HgTe thinfilm on top of a CdTe layer of the same thickness, including a simplified homogeneous distribution of strain. The arrow highlights the position of the Dirac point. The $\vec{k} \cdot \vec{p}$ calculation was done with the »biscuit« software developed in-house by W. Beugeling.

nanowire shell, whereas strain effects are included. Still, we can infer several characteristics of the HgTe band structure from the simulation: First, the band curvature is large in the conduction band, but low in the valence band. From this we can expect high mobility electron transport with a low carrier density in the n-conducting regime, and low mobility hole transport with a high density in the p-conducting regime. The latter is further enhanced by the camel's back shape of the valence band. And second, the Dirac cone of the surface states is shifted deep into the bulk valence band (cf. arrow in Fig. 5.4). This means, that the Dirac point is well below the Fermi energy and thus not directly accessible in charge transport experiments. Further, the density of states at the rather flat valence band edge is likely large enough in order to pin the Fermi level, which would prevent to reach the Dirac point by gating. However, despite of an eventual bulk conductance, the surface state modes can still be expected to contribute to charge transport.

Before turning to the experimental charge transport results of this thesis, we review in the following the experimental work that has previously been carried out on the charge transport investigation of CdTe–HgTe core–shell nanowires.

5.2 Review of charge transport in CdTe–HgTe core–shell nanowires

The integration of nanowires into electrical circuits is challenged by several factors that require adaptations to the established lithographic processing of thinfilm microstructures. First, the small size of the individual nanowires demands a fundamentally different handling compared to thinfilm samples. Second, the three-dimensional shape of the nanowires placed on the lithography substrate, especially with the gaps that form in between, poses difficulties for the lift-off processes commonly employed for the contact lithography. And third, the small cross-section leads to high current densities even for moderate applied voltages, which requires special precautions to be taken in order to protect the wires from electrostatic discharge.

M. Kessel and J. Brehm [14,88] developed a process that overcomes the challenges of HgTe nanowire contact lithography, which allowed for successful first charge transport studies. In the following, we start with summarizing the key points of this process before we review the charge transport results that have so far been achieved. Based on that, we set the aim of this work.

Fabrication of integrated nanowire transport devices

In order to apply electrical contacts, the nanowires are transferred from the as–grown ensemble to a lithography substrate, which typically consists of SiO_2 on Si with a Ti/Au coordinate grid that allows to infer the exact location of the nanowires. Two options turned out to be feasible for the transfer. Either, the nanowires are dispersed in isopropyl alcohol by ultrasonic cavitation, and the effect of AC dielectrophoresis [89] is utilized to attract and align the floating nanowires to an electrode on the substrate as discussed by M. Kessel, J. H. and S. Krüger. [14,90,91] Or, the nanowires are dropcasted by mechanical stamp transfer, i.e., a piece of the as-grown nanowire sample is gently pressed upside-down on the lithography substrate. While the former provides more control over the alignment of the nanowires – which can be advantageous particularly for magnetotransport where a defined field orientation with respect to the nanowire axis is important – the latter is more flexible and requires significantly less effort. Also noteworthy is the by orders of magnitude higher transfer efficiency of the mechanical approach, which makes it the better choice for the position controlled nanowire arrays with a rather low area density discussed in Chapter 3.

After transferring the nanowires, the contact electrodes are patterned by electron beam lithography. Based on optical micrographs of the dropcasted ensemble, an individual contact layout is designed for several of the nanowires. It is crucial, though, that the sample is already coated with PMMA resist prior to the optical imaging in order to prevent subsequent changes in the

nanowire position. The electrodes are typically designed in a quasi-four terminal geometry, where four independent leads for bias current and voltage probe meet pairwise on top of the nanowire [cf. inset in Fig. 5.5(a)]. In order to achieve the required high precision, exposure is started only after the background pressure in the electron microscope is fully stable (usually overnight), which minimizes shifts of the sample stage throughout the process. After development of the areas exposed by the electron beam, the surface is cleaned from contaminations by Ar ion milling, followed by the evaporation of the contact material. It is important to deposit sufficient material in order to overcome the gap between substrate and nanowire; a contact height of about 300 nm proved to be adequate. Then, the remaining resist is removed altogether with the excess contact material on top. A typical resulting sample is shown in Fig. 5.5(a).

Finally, the sample is mounted onto a chip carrier. Prior to bonding the nanowire electrodes to the contact pads of the chip carrier, as shown in Fig. 5.5(b), it is vital to short-circuit the latter for example with bonds to the conductive rim of the chip carrier [cf. red dashes in the inset of Fig. 5.5(b)]. This efficiently protects the samples from electrostatic discharge, which could easily destroy the nanowires due to the high current densities that can develop due to the small cross-section. These protective bonds are removed directly before mounting the sample into a cryostat.

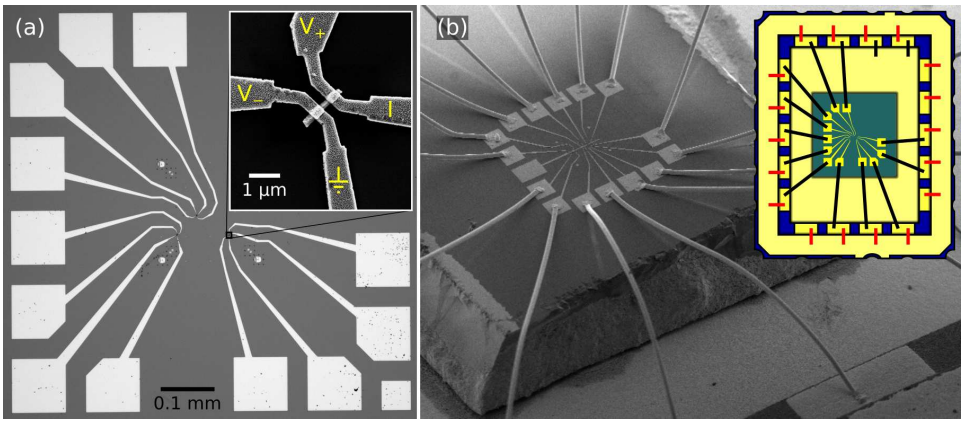

Figure 5.5: Optical micrograph of a typical charge transport sample. The inset shows an electron micrograph of a single contacted nanowire with higher resolution. (b) Electron micrograph of a bonded sample. The inset illustrates the bond wires (black) connecting the nanowire electrodes to the contact pads of the chip carrier, as well as the protective wires (red) that short-circuit all contact pads until the sample is to be measured.

First characterization of charge transport

First low-temperature charge transport experiments involving CdTe–HgTe core–shell nanowires led to several important conclusions: [14] A low contact resistance as well as a high yield of working contacts were observed for Ti- and Al-based electrodes (the respective material stack is given in the Appendix C), whereas AuGe/Au turned out to give unreliable results, which was attributed to the more columnar growth of the latter causing rip-offs at the step from the substrate surface onto the nanowire. The nanowires themselves exhibit typical resistance values of the order of 0.5–2 kΩ in the quasi-four terminal measurement geometry sketched in Fig. 5.5(a). This electrode geometry gave consistent results compared to a true four-terminal geometry, which corroborates the low contact resistance and allows to contact short nanowires with a length that would not be sufficient to connect four individual electrodes. The low total resistance indicates a multi-modal transport regime.

The lithography substrate typically consists of 100–200 nm SiO_2 on degenerately doped Si, thus it can be used as an integral back gate in order to apply an electrostatic potential that affects the Fermi energy in the band structure of the nanowires. Gate dependent conductance measurements showed random fluctuations with an amplitude of the order of e^2/h on top of a positive slope that indicates the population of electronic states with increasing gate voltage. However, the back gate efficiency turned out to be too low in order to draw conclusions about the underlying electronic structure. [14]

Further, the influence of an external magnetic field was investigated. A pronounced positive magnetoresistance was found for a field orientation perpendicular to the nanowire axis. Aperiodic fluctuations on top, which are symmetric under field reversal, were interpreted as universal conductance fluctuations. These fluctuations occur in mesoscopic systems from the interference of phase-coherent electron trajectories defined by the random distribution of scattering sites. With parallel magnetic field orientation, a similar but slightly more regular fluctuation pattern was observed. In this case, the interfering electron trajectories are geometrically constricted by the tubular cross-section of the HgTe shell. [14]

Beyond that, first experiments on charge transport with superconducting contact electrodes were also conducted. A non-linear voltage–current (VI) characteristic with a reduced zero-bias resistance was observed at millikelvin temperature, which was interpreted as a noise-limited supercurrent as the manifestation of superconducting correlations induced from the contact electrodes into the HgTe nanowires via the proximity effect. In addition, a pronounced subgap structure in the dynamic conductance dI/dV indicates the presence of multiple Andreev reflections. [14,45]

Starting point for the following investigation

So far, many basic obstacles for the investigation of charge transport through HgTe nanowires have already been overcome, and first transport results were achieved. Still, several important points remain to be addressed.

The first major aspect concerns the quality of the nanowires for magneto-transport. Quantum interference is very sensitive to both the crystal quality and the cross-sectional morphology of the nanowires. Up to now, a clear sign of a purely geometry related flux-periodic quantum interference oscillation has not been observed in CdTe–HgTe core–shell nanowires. These heterostructures typically exhibit pronounced tapering and a dense distribution of twin plane defects. The ZnTe–CdTe/HgTe nanowires developed in Part I of this work bring a significant improvement with respect to both of these points. The question is now whether their quality is sufficient to allow for the investigation of flux-periodic magnetoconductance oscillations, which is an important step in the progress of gaining further insight into the electronic structure of the HgTe nanowire shell, and could help to take advantage of the unique flux-tunable band structure in future experiments.

The second aspect is a reliable gate electrode that allows to adjust the Fermi level over a wide range, which is fundamental for a thorough transport characterization. The substrate as an integral back gate turned out to provide only insufficient gate efficiency and stability. The most straightforward approach to improve gating would thus be a top gate fabricated subsequent to the contact electrodes, which minimizes possible damage to the gate insulator during sample processing and thereby improves its reliability. Further, a thinner gate insulator with a higher dielectric constant is important to enhance the gate effect.

And the third aspect is the methodological improvement of the investigation of proximity superconductivity. So far, a high level of current noise led to a considerable suppression of the observed supercurrent. This impairs its quantitative analysis, which is crucial for a better understanding of the induced superconductivity. A careful investigation of the induced supercurrent with improved filtering is thus the starting point for further experiments. Additionally, while direct current (DC) measurements can provide an important general characterization, eventual topological properties are better accessible by probing the dynamic behavior of the junction. In order to do so, an established technique is to detect the characteristics of the Shapiro steps, which are regions of constant voltage appearing in the VI curves under microwave excitation.

The following chapters address these aspects in order to provide a thorough characterization of the nanowires grown in the first part of this work as a basis for future studies that strive to investigate topological charge transport in the novel tubular nanowire geometry.

Chapter 6

Quantum interference

Electrically conducting nanowires are often referred to as quantum wires. The eponymous characteristic of a quantum wire is the strong influence of size effects that arise from its nanoscale physical dimensions. One of these effects observed in our HgTe nanowire shells is the interference of electronic states that gives rise to a modulation of the conductance in a parallel magnetic field. This modulation may be composed of different contributions. On the one hand, reproducible but aperiodic fluctuations of the magnetoconductance can originate from self-interference along time-reversed paths formed by scattering sites and defects in the sample. On the other hand, regular magnetoconductance oscillations can occur with a period that is linked to the cross-sectional geometry of the sample – or, to be more precise, the spatial extent of the conductive states in the HgTe shell.

Hence, the analysis of the magnetoconductance might allow to draw conclusions about the underlying physical properties of the system and can be used to investigate and compare the quality of the nanowire heterostructures discussed in the first part of this work.

6.1 Magnetotransport for quality assessment

Electron microscopy is ideal for the detection of extended defects in a crystal lattice such as twin domains or dislocation lines. However, charge transport can be affected also by local scattering centers, i.e., dopants, impurities or vacancies that distort the electronic structure of the periodic crystal, [92] which are very challenging to detect with common imaging techniques. Thus, the quality of a sample is probed more reliably by a transport analysis. In nanoscale systems with an electronic state on a closed trajectory, the manifestation of quantum interference in the magnetoconductance is strongly affected by defects in the crystal lattice: For heavily distorted materials, the phase coherence length is well below the sample dimensions and interference effects are absent. At an intermediate density of scattering sites, the interference of phase coherent time-reversed paths can alter the magnetoconductance and give rise to universal conductance fluctuations [93] and the Al'tshuler–Aronov–Spivak effect. [87] In very clean systems, the Aharonov–Bohm effect [86] can result in magnetoconductance oscillations that are h/e-periodic in magnetic flux. Hence, the analysis of magnetotransport can provide an essential tool to investigate and compare the quality of the nanowire heterostructures discussed in the first part of this work.

Comparison of quantum interference effects

We start with a brief overview of different quantum interference mechanisms, which are illustrated in Figure 6.1. A detailed review of those is given by S. Washburn and R. A. Webb. [94] Generally, electron interference may occur when phase coherent closed paths exist in a sample. In clean samples with a very low defect density a closed path can be realized as a quantum ring connected to a source and drain contact. Electrons have two possibilities to traverse the ring, indicated by the blue and green traces in Fig. 6.1(a). With

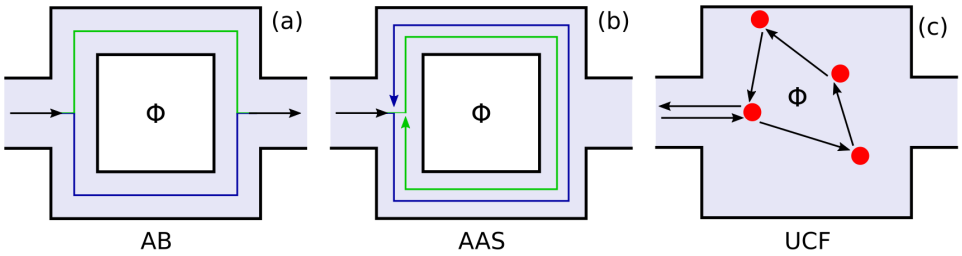

Figure 6.1: Illustration of different quantum interference effects: (a) Classical h/e-periodic Aharonov–Bohm effect, (b) $h/2e$-periodic Al'tshuler–Aronov–Spivak effect, and (c) universal conductance fluctuations. Φ is the magnetic flux enclosed by the electron trajectories denoted by arrows, red dots indicate elastic scattering sites.

a vector potential enclosed by the ring – in this case the magnetic flux Φ – the electron accumulates a phase that depends on the direction of motion, which is referred to as the Aharonov–Bohm phase. Thus, the superposition of both possible paths creates interference with a periodicity given by the flux quantum $\Phi_0 = h/e$. [94] With increasing defect density this interference effect is quickly suppressed: Elastic scattering events that vary with magnetic field randomly alter the phase relation between the two possible trajectories through the quantum ring. Without the defined zero-field phase relation, the Φ_0-periodic oscillations average out. [95] Beyond the classical realization in quantum rings, the Aharonov–Bohm effect also gives rise to the Φ_0-periodic effect on the band structure of tubular electronic states enclosing a magnetic flux that is discussed in Section 5.1 of the previous chapter.

In moderately distorted crystals, interference paths can be formed not only by the sample geometry, but also by the random distribution of defects. For the geometry-defined case, Fig. 6.1(b), B. L. Al'tshuler, A. G. Aronov and B. Z. Spivak [87] showed that the interference of a full 2π–passage through a quantum ring gives a similar result compared to the classical Aharonov–Bohm effect, but with half the oscillation period. However, in this case the interference occurs between time-reversed paths [cf. blue and green arrows in Fig. 6.1(b)], which have the same zero-field phase relation at the interference point irrespective of elastic scattering events. [95] Thus, the $\Phi_0/2$-periodic oscillations tolerate the presence of defects as long as phase coherence is maintained.

In the defect distribution-defined case, illustrated in Fig. 6.1(c), the scattering paths change randomly with magnetic field. As long as phase coherence is maintained, the random interference contributions are not averaged out. [94] Hence, the conductance fluctuates of the order of the conductance quantum e^2/h, which is referred to as universal conductance fluctuations. [93] Resulting from the defect configuration within the sample, these fluctuations in general do not depend on the sample size. However, in samples that are small compared to the phase coherence length, such as nanowires, the average area $\bar{A}$ enclosed by the phase coherent scattering paths can be restricted by geometry. This results in a lower boundary for the characteristic magnetic field scale for a fluctuation period, the so-called correlation field B_{corr}, which is inversely proportional to $\bar{A}$.

In the following, we analyze the magnetic field dependent charge transport at low temperature ($T \sim 2\,\mathrm{K}$) with respect to these quantum interference effects in our HgTe nanowires contacted with Ti/Au electrodes in a quasi four terminal geometry. For details on the lithographic processing of these samples, please refer to the Appendix C.

Self-organized CdTe–HgTe nanowires

We begin the experimental invesitigation with the core–shell heterostructures based on self-organized CdTe nanowires (cf. Chapter 2). Figure 6.2 shows the magnetoconductance of two exemplary nanowires together with an electron micrograph of the as-grown ensemble and an illustration of the typical qualitative cross-section. The magnetoconductance curve of the first device, depicted in Fig. 6.2(a), exhibits pronounced fluctuations with a magnitude of the order of e^2/h that are symmetric in B. Up to about 3 T the fluctuations show some degree of regularity, which vanishes towards higher fields. Overall, the signal is predominantly aperiodic, which can be interpreted as a manifestation of universal conductance fluctuations. Their presence is possibly explained by a large amount of scattering centers formed by the high density of twin plane defects in the CdTe-based nanowires (cf. TEM investigation in Chapter 2). However, the rather low spread in the average fluctuation period of the order of 0.3–0.6 T indicates also an influence of the restricted sample geometry. From $\bar{A} = \gamma\Phi_0/B_{\mathrm{corr}}$, γ being a numerical coefficient of the order of 1, [96] we can estimate an equivalent circle diameter of roughly 0.1 µm, which is consistent with the typical dimensions of the self-organized CdTe–HgTe nanowires (cf. Chapter 2). Further, the tapered morphology of the nanowire core shown for example in Fig. 2.7, as well as the stepped HgTe surface that can be inferred from the electron micrograph Fig. 6.2(c), alters the cross-sectional shape. This leads to a variation of the geometrical frequency along the nanowire, which might additionally hinder the observation of a regular Φ_0-periodic Aharonov–Bohm oscillation.

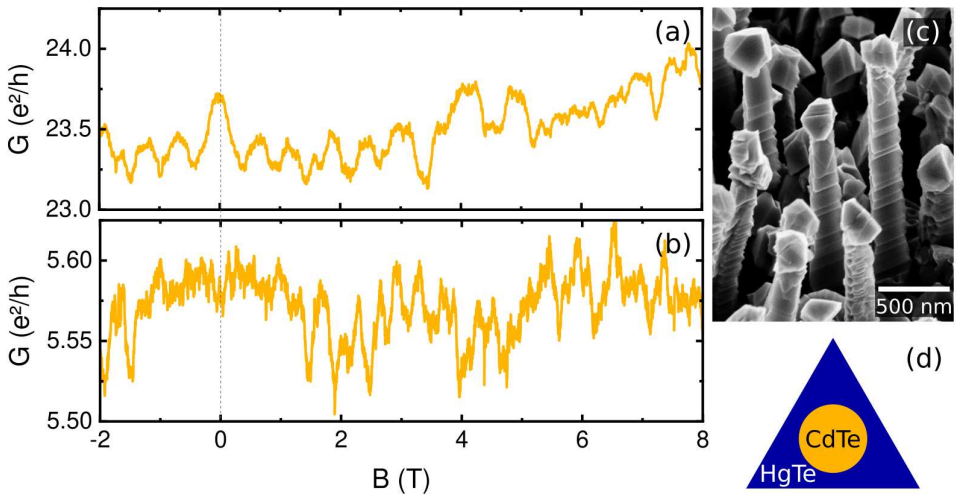

Figure 6.2: (a)–(b) Magnetoconductance curves obtained from two exemplary self-organized CdTe–HgTe nanowires of the as-grown sample shown in (c), (d) illustrates the qualitative cross-section.

Compared to Fig. 6.2(a), the magnetoconductance curve of the second device shown in Fig. 6.2(b) is qualitatively similar but has a significantly different shape with a stronger contribution of fluctuations with a smaller correlation field. This diversity of the magnetoconductance signal is possibly linked to differences in both the nanowire geometry and the defect density, which is likely a result of the self-organized fabrication process. These results are qualitatively similar to what was reported in previous work on CdTe–HgTe nanowires. [14, 45]

Position-controlled ZnTe–CdTe/HgTe nanowires (smooth HgTe shell)

Contrary to the self-organized CdTe nanowires, our selective area grown ZnTe cores appear to be mostly dislocation free and have an essentially untapered shape (cf. Chapter 3). Further, in Chapter 4 we optimized HgTe overgrowth in order to suppress the faceting of the surface, which allows us now to investigate charge transport through a smooth HgTe shell. The quality of the magnetoconductance oscillations can be expected to benefit from both factors. Figure 6.3 shows the result obtained for two exemplary nanowires of an array that was optimized for a smooth surface. Surprisingly, the magnetoconductance curve shown in Fig. 6.3(a) exhibits a slightly regular pattern (up to 1 T, and around 4 T) that is again overlaid with a strong

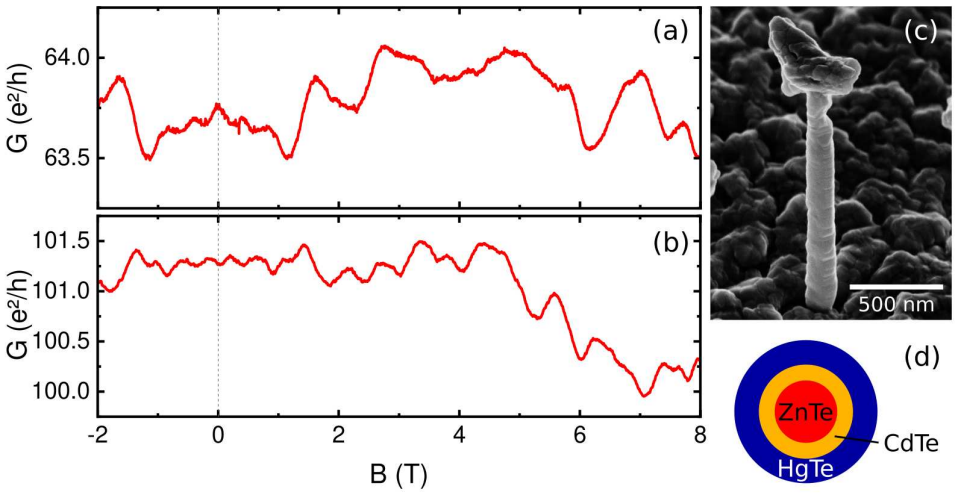

Figure 6.3: (a)–(b) Magnetoconductance curves obtained from two exemplary selective area grown ZnTe–CdTe/HgTe nanowires, for which the HgTe overgrowth was optimized for a smooth surface. The as-grown sample is shown in (c), (d) illustrates the qualitative cross-section.

contribution of aperiodic fluctuations. The average period of the more regular pattern, $\sim 0.4\,\mathrm{T}$, resembles an approximate equivalent circle diameter of about 110 nm, which is consistent with the typical dimensions of the nanowires [cf. Fig. 6.3(c)] and thus might represent the influence of the sample geometry. The aperiodic fluctuations with a larger period are taken as a sign of universal conductance fluctuations, where elastic scattering sites can form smaller interference trajectories. Hence, this might point to the presence of a significant defect density also in these heterostructures. However, with this batch of nanowires we observe qualitatively similar magnetoconductance results for different devices [cf. Fig. 6.3(b)], which is consistent with the homogeneous appearence of the nanowire arrays resulting from the well-controlled selective area growth process, and indicates a good sample–to–sample reproducibility.

In order to explain the still prominent contribution of conductance fluctuations in these nanowires, we need to consider that the smooth outer surface of the HgTe shell is realized at a relatively high substrate temperature close to the point of desorption (cf. Section 4.2). This could give rise to high temperature growth defects such as Hg vacancies, which are difficult to observe in transmission electron microscopy but likely detoriate the transport properties. Even though HgTe shells grown at a high substrate temperature have an advantageous smooth shape, they might not be the ideal candidate for charge transport investigation due to their possibly limited crystal quality. Hence, we discuss in the following the magnetotransport in nanowire heterostructures that are based on the position controlled ZnTe nanowire arrays but have a HgTe shell that is grown at an intermediate substrate temperature.

Position-controlled ZnTe–CdTe/HgTe nanowires (stepped HgTe shell)

In Section 4.2 we found that the formation of surface steps in HgTe nanowires is likely linked to a step-flow growth regime. While these growth conditions give rise to an inhomogeneous diameter of the outer surface, they might possibly provide superior crystal quality, which in turn would result in a lower contribution of universal conductance fluctuations to the magnetoconductance signal. In order to test this, we investigate in the following samples where the HgTe shell is grown at a substrate temperature that is low enough to ensure step-flow overgrowth, but at the same time sufficiently high to match the growth window on both A- and B-polar surface facets. This regime can be inferred from the smooth morphology of layer growth on the substrate between the nanowires (cf. upper central image in Fig. 4.7). Figure 6.4 shows the results obtained from such a sample. The electron micrograph in Fig. 6.4(c) indicates that the nanowires have pronounced surface steps and a triangular cross-section. Despite the irregular outer

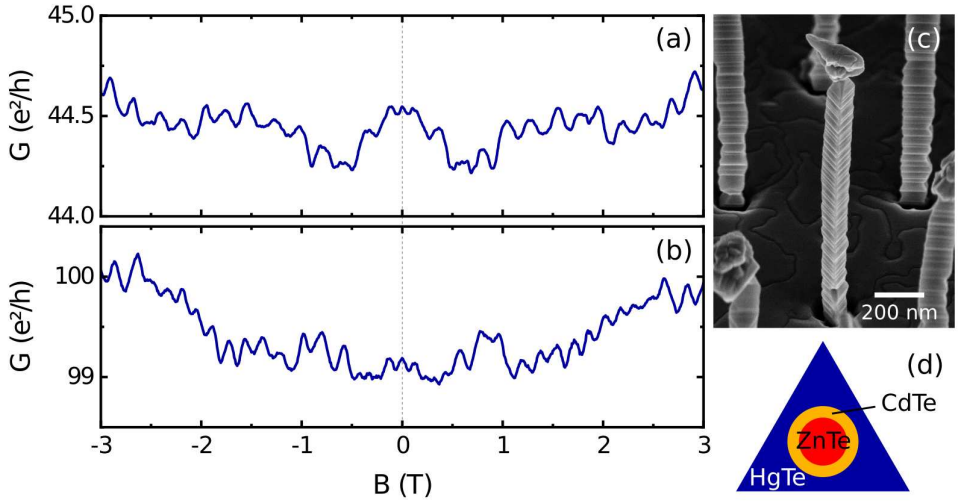

Figure 6.4: (a)–(b) Magnetoconductance curves obtained from two exemplary selective area grown ZnTe–CdTe/HgTe nanowires, where the HgTe shell was grown in the step-flow regime. The as-grown sample is shown in (c), (d) illustrates the qualitative cross-section.

morphology, the magnetoconductance curve depicted in Fig. 6.4(a) shows a magnetoconductance oscillation that is by far more homogeneous and clear than the previously discussed measurements. The random features of universal conductance fluctuations seem to be essentially absent, which indicates the successful realization of a HgTe nanowire shell with a very high crystal quality. The magnetotransport result of a second nanowire from the same batch – shown in Fig. 6.4(b) – appears very similar, which indicates that the improvement of quality is consistent and reproducible.

If these oscillations indeed originate in the Aharonov–Bohm effect, their period should relate to the cross-sectional geometry of the nanowire. As discussed in Section 5.1, the magnetoconductance of an electronic state enclosing a homogeneous magnetic flux density B within an effective area A with a surface vector parallel to the direction of magnetic field is altered by an Aharonov–Bohm phase with a periodicity of

$$\Delta B = \frac{\Phi_0}{A} = \frac{h}{eA}\,. \tag{6.1}$$

In case of the Al'tshuler–Aronov–Spivak effect, an effective area of half the size would result in the same B-field period. Thus, from the observed oscillation period we can estimate the effective cross-sectional area of the electronic state and compare it to the dimensions of the nanowire. One possibility to extract the experimental oscillation period is to subtract a floating average from the magnetoconductance curve in Fig. 6.4(a), which

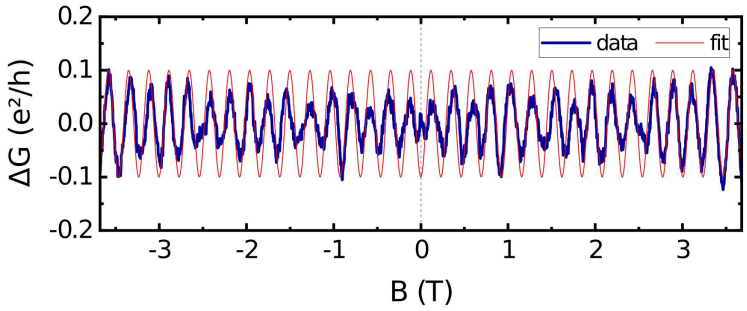

Figure 6.5: Background corrected magnetoconductance ΔG (blue) shown together with a sinusodial fit of the oscillation period, using $\Delta B = 0.231\,\mathrm{T}$. For background removal a floating average was subtracted from the curve shown in Fig. 6.4(a).

removes the varying background and leaves the pure oscillation signal shown in blue in Fig. 6.5. From a sinusodial fit (red) we can then extract an oscillation period of $\Delta B = 0.231\,\mathrm{T}$. Following equation 6.1, we infer an effective area of $0.0179\,\mu\mathrm{m}^2$, which corresponds to an equivalent circle diameter of about 150 nm. This is a plausible value, considering the typical diameter of around 200 nm observed in electron micrographs for a batch of nanowires from the same growth sample. Based on these promising first results, we investigate in the following section the magnetoconductance oscillations in more detail.

6.2 Evaluation of Aharonov–Bohm oscillations

In the previous section we confirmed the presence of regular magnetoconductance oscillations in our optimized ZnTe–CdTe/HgTe heterostructures. A thorough analysis of these oscillations might reveal further information about electron transport and the underlying band structure of the nanowires. This, however, requires to reliably control the band filling by adjusting the Fermi energy. To do so, an electrostatic potential is typically applied with an electrode separated from the device by a gate insulator. First experiments on the gate effect in CdTe–HgTe nanowires achieved only very limited influence with the integral back gate that is formed by the conductive n-doped Si lithography substrate covered with 100–200 nm of insulating SiO_2. Thus, we begin this section with the improvement of the gate efficiency, which then allows us to analyze the gate voltage dependent magnetotransport.

Implementation of a top gate

An alternative to using the conductive substrate as the gate electrode is the application of a dedicated gate structure on top of the contacted sample [cf. Figs. 6.6(a) and (b)]. This allows us to use HfO_2 as the gate insulator – a material that is characterized by a low chemical reactivity and an about six times larger dielectric constant ($\kappa = 25$) compared to SiO_2, [97] which is expected to significantly enhance the gate efficiency. The gate insulator is grown as an isotropic ~ 20 nm thin layer at a process temperature of 30 °C with atomic layer deposition, which is a purely surface reaction limited chemical vapor deposition technique where the sample surface is alternatingly saturated with the gaseous precursor molecules, in this case $Hf[N(CH_3)(C_2H_5)]_4$ as Hf

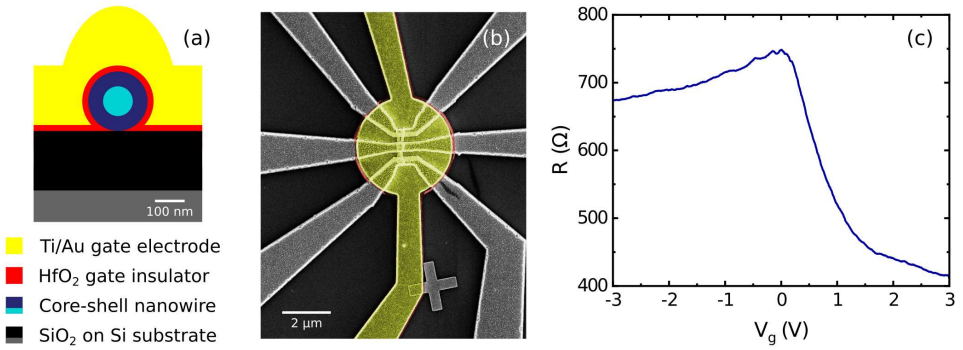

Figure 6.6: (a) Schematic cross-section of the nanowire gate stack. (b) Top down electron micrograph of a contacted HgTe nanowire transport device covered with a top gate (highlighted in false color). (c) Influence of the top gate voltage V_g on the resistance R of a ZnTe–CdTe/HgTe core–shell nanowire at a temperature of 2 K.

precursor and H_2O as oxidant, each followed by Ar purging. A thorough analysis of the respective surface reactions is given, e.g., by W. Chen *et al.* [98] Subsequently, the Ti/Au gate electrode is deposited self-aligned in an ultra-high vacuum metallization chamber. The fabrication processes is described in detail in the Appendix C.

An exemplary transport characterization of a top-gated nanowire junction is shown in Fig. 6.6(c). A pronounced modulation of the device resistance with the applied top gate voltage V_g is observed, with a qualitatively similar shape for different samples. This indicates, that we are now able to adjust the band filling over a considerable range, which is fundamental for studying the influence of the Fermi level on charge transport. Most samples exhibit a resistance maximum around zero gate voltage, as can be seen from the curve shown in Fig. 6.6(c). The steep decrease towards positive gate voltage can be interpreted, based on the typical band structure of a HgTe thinfilm shown in Fig. 5.4, as the electron (n) conducting regime, whereas the slight decrease towards negative gate voltage indicates hole (p) conductivity. The asymmetry of the curve can be explained by the difference in mobility and carrier density for electrons and holes in HgTe. [99] Intuitively, one would expect that the maximum in resistance corresponds to the bulk bandgap. However, scattering with holes from the bulk valence band can lead to an enhanced resistance towards lower gate voltage, thus the charge neutrality point in HgTe appears to be typically located not exactly at the resistance maximum but rather in the initial negative slope. [99] The overall low maximum resistance of the order of $\sim 1\,\mathrm{k}\Omega$ indicates multi-modal transport even at the charge neutrality point, which is not surprising given that the Dirac point is expected to be buried deep in the valence band (cf. Section 5.1) and already the surface states are therefore expected to carry several modes up to higher order in k_φ.

Evaluation of the Aharonov–Bohm effect

Having established the functionality of the top gate, we now can analyze the magnetoconductance oscillations in greater detail. For this we investigate a sample that is characterized by a particularly high ensemble homogeneity, which is important in order to estimate the cross-sectional area of nanowire core and shell with sufficient accuracy from electron micrographs of the as-grown ensemble.

We begin the evaluation at positive gate voltages, where we expect an overall high charge carrier mobility in HgTe. Figure 6.7(a) shows exemplary magnetoconductance curves for $V_g = 2.8$ and $3.0\,\mathrm{V}$. Similar to the results from the previously discussed batch we observe well-defined oscillations. Plotting the position of the conductance peaks [vertical red lines in Fig. 6.7(a)] against the peak index in Fig. 6.7(b) allows us to extract an oscillation period of

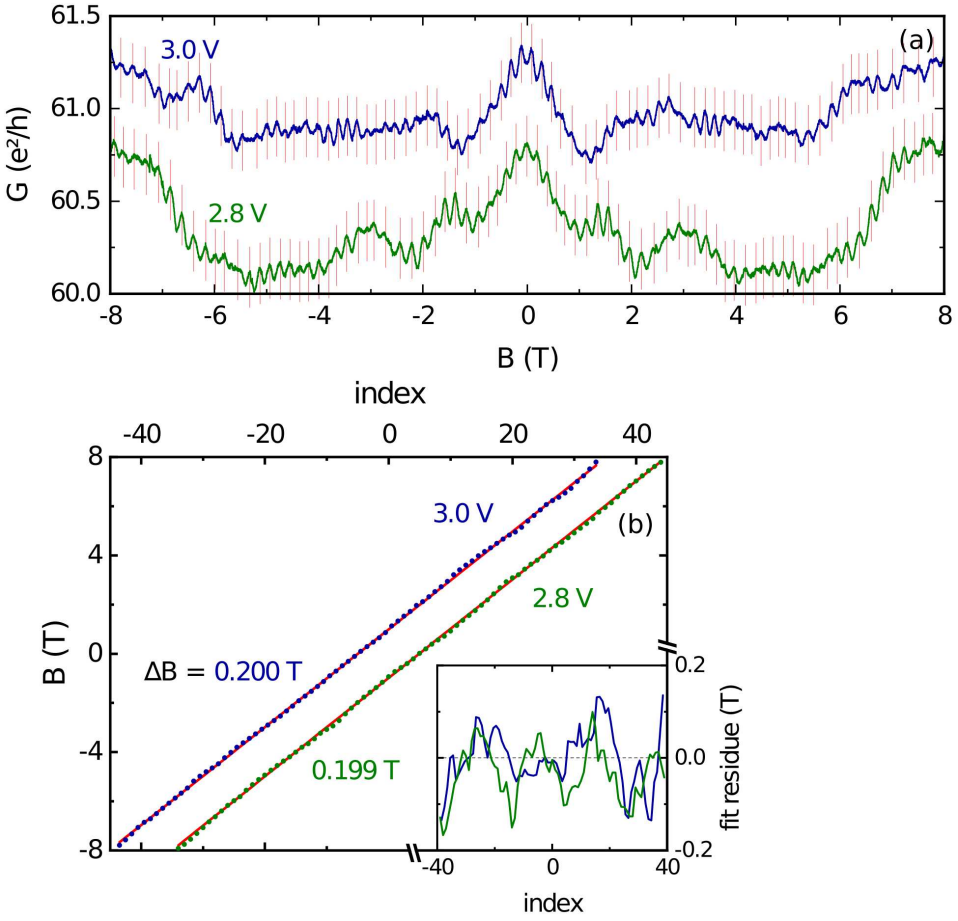

Figure 6.7: (a) Magnetoconductance of a ZnTe–CdTe/HgTe core–shell nanowire at two exemplary gate voltage values as denoted. Vertical red lines indicate peak positions, which are plotted in (b) against the peak index together with a linear fit to the data. Peak indices are shifted for clarity by ± 5 for $V_g = 2.8$ and 3.0 V, respectively. The inset in (b) shows the fit residue.

0.200 and 0.199 T from the slope for $V_g = 2.8$ and 3.0 V, respectively. This corresponds to an effective area of 0.021 μm^2.

In order to classify this value, we compare it to the geometrical dimensions of the nanowire, which we can infer from material sensitive SEM images of nanowires from the same batch. Figure 6.8 shows the results. The overview image, Fig. 6.8(a), indicates a very high ensemble uniformity of the as-grown nanowire array that allows to apply the conclusions drawn from the microscopy study to the nanowire measured in transport. From topography and material sensitive electron micrographs [Figs. 6.8(b) and (c), respectively] we compile false-colored overlay images of the cross-sectional surface such as shown in

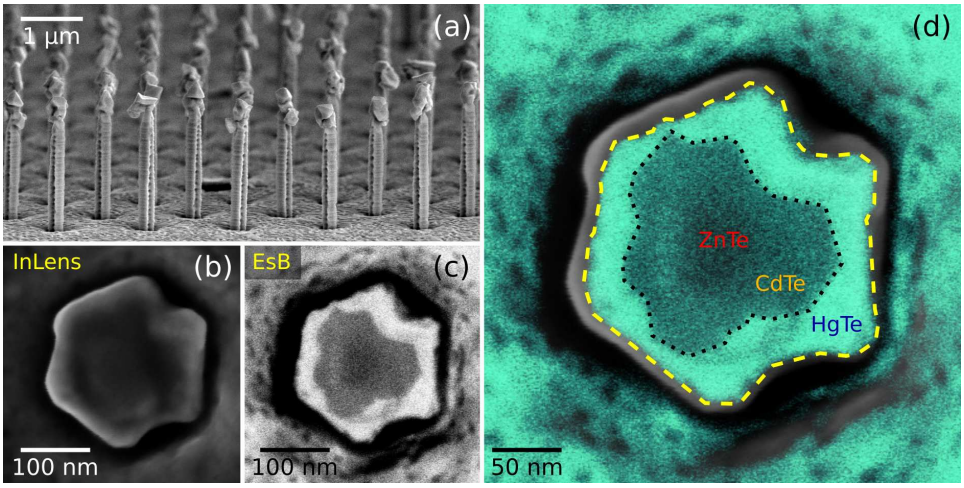

Figure 6.8: Scanning electron micrographs of a ZnTe–CdTe/HgTe core–shell nanowire. (a) Image of the as-grown ensemble under an angle of 80° from the surface normal. Top-down images (b) and (c) of the cross-sectional surface of a nanowire close to its base are acquired simultaneously with InLens and EsB detector, respectively. (d) Overlay image of (b) and (c) shown together with the estimated outer (yellow dashed line) inner (black dots) HgTe interface inferred from the EsB signal.

Fig. 6.8(d). Based on images of several individual nanowires we can calculate an average area enclosed by the outer [yellow dashed line in Fig. 6.8(d)] and inner (black dotted line) interface of the HgTe shell of $A_\mathrm{o} = 0.034 \pm 0.002\,\mu\mathrm{m}^2$ and $A_\mathrm{i} = 0.015 \pm 0.001\,\mu\mathrm{m}^2$, respectively. The fact that the effective area inferred from magnetotransport, $0.021\,\mu\mathrm{m}^2$, lies between A_i and A_o matches the assumption of charge transport taking place in the HgTe shell, and corroborates that the magnetoconductance oscillations are indeed Φ_0-periodic and can be attributed to the Aharonov–Bohm effect. In particular, this contradicts the $\Phi_0/2$-periodic Al'tshuler–Aronov–Spivak effect as the origin, where the effective area would be smaller than A_i, for which no evident current path exists. Hence, the magnetoconductance measurements suggest that our optimized ZnTe–CdTe/HgTe heterostructures are sufficiently clean in order to show a clear and pronounced Aharonov–Bohm effect. Interestingly, though, the effective area related to the observed oscillation period lies considerably closer to the inner interface.

Comparing the central part of the magnetoconductance curves for $V_\mathrm{g} = 2.8$ and 3.0 V in Fig. 6.7(a), we find that the feature at zero field changes from peak to valley. In order to investigate this switching in more detail we now discuss the gate dependence of the magnetoconductance at low magnetic field. Figure 6.9(a) shows the resulting background subtracted

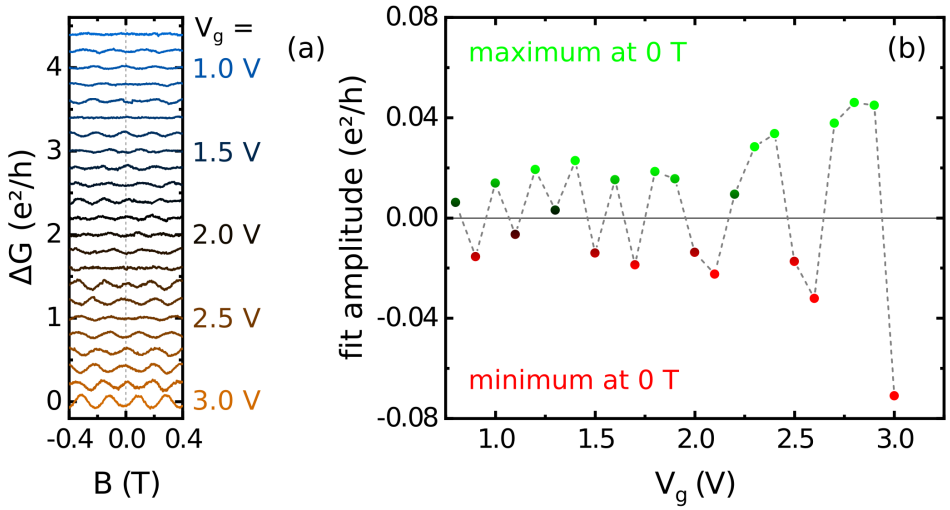

Figure 6.9: (a) Gate dependent magnetoconductance (background subtracted via floating average) for small magnetic field. Curves are offset by $0.2e^2/h$ for clarity. (b) Oscillation amplitude of a sinusodial fit to the data shown in (a).

curves for $V_g = 0.8$–$3.0\,\mathrm{V}$. Within this gate range we observe several peak-to-valley transitions. For a better visualization, the oscillation amplitude of a sinusodial fit to the data is shown in Fig. 6.9(b). Although the coarse resolution in gate voltage clearly limits the reliability of any conclusion drawn, there appears to be a trend for an increase of the absolute value of the oscillation amplitude with increasing gate voltage (i.e., deeper into the n-conducting regime), which might be an indication for bulk states as the origin of the magnetoconductance oscillations. In order to explain the switching, we need to consider the peculiar nanowire band structure discussed in Section 5.1. The periodic boundary condition for electron wavefunctions along the perimeter results in a quantization of the angular component of the wavevector. Thus, the continuous three-dimensional bandstructure is split into a set of subbands. When the Fermi energy is located at the bottom of a subband for $\Phi = 0$, the magnetic field oscillation due to the Aharonov–Bohm phase should have a conductance maximum at zero field. If it lies between two subbands, a minimum is expected. An increasing magnetic field shifts the subbands in energy, which at $\Phi = \Phi_0/2$ reverses the type of extremum and continues as a periodic oscillation. This predicts a transition between peaks and valleys in the magnetoconductance, irrespectively of the exact shape of the underlying three-dimensional dispersion. The fact that we are able to experimentally observe such transitions corroborates the validity of the simplistic band structure model, which is an important step for a basic understanding of charge transport effects in these structures.

However, in order to safely differenciate between contributions of trivial parabolic bulk bands and the linear topological surface states one would have to probe the presence of the perfectly transmitted mode at the Dirac point, as a qualitatively similar switching between magnetoconductance peaks and valleys can be observed in both topologically non-trivial [100] and trivial [101] nanowire systems. Unfortunately, in HgTe the Dirac point is buried deep in the bulk valence band and the massive desity of states at the valence band edge can possibly screen external electric fields, which impedes the accessibility by gating.

A closer look at the analysis of conductance peak positions in Fig. 6.7(b) indicates periodic deviations from the linear relation, which can be seen more clearly from the fit residue shown in the inset. This beating signals an overlay of multiple frequencies. Fourier transformation is a powerful tool that allows us to analyze the frequency contributions of which the magnetoconductance signal is composed. Figure 6.10(a) shows a color coded plot of the power spectral density (PSD) – the product of the Fourier transformed signal with its complex conjugate – for different gate voltage. It should be pointed out that the PSD is calculated from the raw data, without further smoothing or background subtraction that might influence the result. Over the investigated

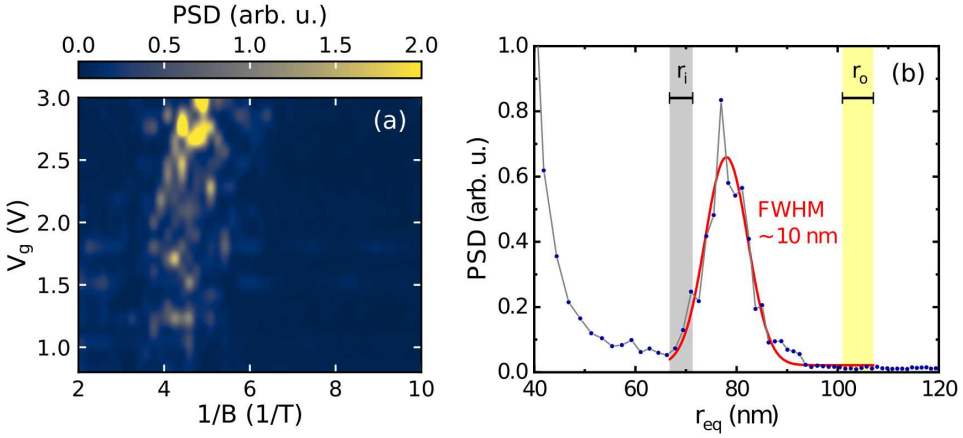

Figure 6.10: (a) Gate dependence of the power spectral density, obtained by a discrete Fourier transformation of the magnetoconductance raw data in a range of −3 to 3 T. (b) Average PSD over the gate range of 1–3 V fitted with a Gauß curve (red). The x-axis was converted from magnetic field frequency $1/B$ to an equivalent circular radius r_{eq} via the Aharanov–Bohm relation Eq. 6.1. Vertical bars labeled r_i and r_o denote the estimated equivalent radius of inner and outer HgTe interface, calculated from the cross-sectional area inferred from electron micrographs as discussed with Fig. 6.8(d).

gate range between 0.8 and 3.0 V we observe a broad peak within an approximately constant frequency range of about 3.5–6 T^{-1}, with an amplitude that decreases towards lower values of V_g. In order to analyze this peak in detail, we show in Fig. 6.10(b) the gate-averaged PSD in dependence of the equivalent circular nanowire radius r_eq, which we calculate from the effective cross-sectional area $A = \Phi_0/B = r_\mathrm{eq}^2\pi$. From fitting a Gauß curve (red) to the data we can infer that the peak is centered around $r_\mathrm{eq} = 78\,\mathrm{nm}$ with a full width half maximum (FWHM) of about 10 nm. Thus, the electronic state that contributes most to the Aharonov–Bohm oscillations appears to be located close to the inner interface of the HgTe shell [cf. vertical bars in Fig. 6.8(d) that illustrate the equivalent radii $r_\mathrm{i} = 69 \pm 2\,\mathrm{nm}$ and $r_\mathrm{o} = 104 \pm 3\,\mathrm{nm}$ of inner and outer interface], which coincides with the result of the peak position evaluation based on Figs. 6.7–6.8.

So far, our analysis suggests that the main contribution to mangetotransport is carried by modes closer to the inner interface of the shell within an approximate radial extent of about 10 nm. This *per se* neither contradicts transport through a slightly delocalized surface state, nor can exclude bulk-dominated transport (which appears as the more likely case, given that the oscillation amplitude increases when the sample is gated deeper into the n-conducting regime). Anyhow, it indicates a suppression of charge transport towards the outer surface, which might be improved by an *in situ* grown protective cap. Growth tests of an epitaxial (Hg,Cd)Te shell for this purpose already proved to be successful with respect to the crystal quality, and first transport results are expected soon. Following up on our FFT-based approach to the analysis of the radial mode distribution, the investigation of nanowires with a thicker HgTe shell and a therefore expectedly larger difference in the radial extent of surface and bulk modes might furthermore provide an important tool to distinguish their respective contribution to magnetotransport.

Chapter 7

Proximity-induced superconductivity

The conceptual breakthrough for the realization of spinless superconductivity in heterostructures of conventional superconductors and spin-active materials such as topological insulators, [82] *spin-orbit semiconductors* [102] *or ferromagnets* [103] *via the proximity effect spurred a large-scale research effort that is aimed at the realization of quasiparticle excitations that resemble Majorana fermions in a condensed matter system. Those peculiar states are invariant under complex conjugation (i.e., they are their own anti-particle) and might find potential application based on their non-abelian exchange statistics in fault tolerant topological quantum computation – nowadays considered as one of the future key technologies.*

Until now, a variety of material systems has been identified as a possible platform for the condensed matter realization of Majorana bound states. Among these are topological insulator nanowires in proximity to a trivial superconductor. Due to the spatial confinement in a quasi-one-dimensional geometry, pairs of Majorana bound states are predicted to be localized at both ends, which makes our HgTe nanowires an appealing potential candidate.

A fundamental step in this direction is to demonstrate that superconducting pairing can be induced into this system, the basic aim of the first section of this chapter where we investigate the DC behavior of HgTe nanowires that are connected to superconducting electrodes. Further conclusions about the nature of the induced pairing potential can be drawn from the Andreev bound state spectrum, which can be probed by studying the AC response of the nanowire junctions. In order to do so, we study the evolution of Shapiro steps under microwave irradiation in the second section. Parts of this chapter are published in »J. H. *et al.*, Nano Lett. **19**, 4078–4082, (2019)«.

7.1 Induced superconductivity and multiple Andreev reflections

Superconductivity is a highly correlated quantum state of matter that occurs as a low-temperature phase transition and comes with an abrupt change in a variety of material properties, such as a vanishing resistance (ideal conductivity) [105] and the expulsion of magnetic field from inside the material (ideal diamagnetism). [106] In a pioneering work, J. Bardeen, L. N. Cooper and J. R. Schrieffer (BCS) [107, 108] proposed a successful microscopic theory of superconductivity based on the pairing of electrons at the Fermi level. At low temperature, an attractive force mediated by phonon interaction can eventually overcome the Coulomb repulsion and bind electrons to so–called Cooper pairs. Composed of two correlated spin–1/2 Fermions, the Cooper pairs have an integer spin of 0 (spin–singlet state) or 1 (unconventional spin–triplet state) and can thus effectively be described by Bose–Einstein statistics as a macroscopic collective quantum phenomenon with a common ground state. The reduced energy of this BCS ground state alters the band structure of the unpaired electrons close to the Fermi energy and results in an energy gap $E_g = 2\Delta$, where Δ is the superconducting pairing potential. The conservation of states during the superconducting phase transition requires that unpaired states within an energy range of $\pm\Delta$ around the Fermi energy are shifted to the edges of the superconducting gap, which results in a density of states with a characteristic shape as illustrated by Fig. 7.1.

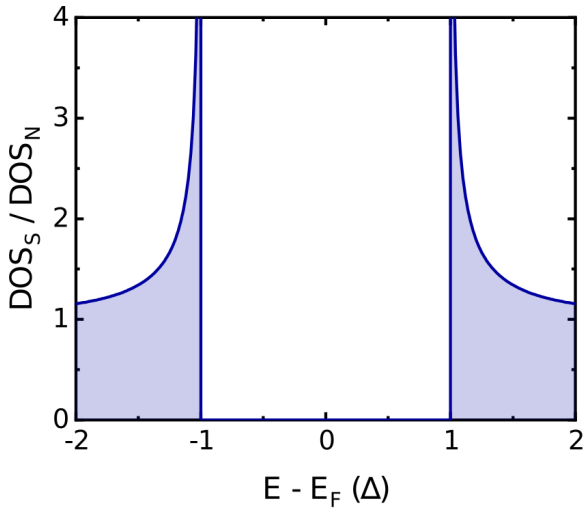

Figure 7.1: Density of states of a superconductor, normalized with respect to the density of states in its normal conducting state.

If the superconductor is in close proximity to a normal conductor (in the sense of not a superconductor) the Cooper pair wavefunctions can extend into the normal conductor, which is mathematically described by an induced superconducting order parameter Δ_i, and referred to as the proximity or Holm–Meissner effect. [109] The spatial extent of the induced gap is limited by pair breaking mechanisms such as scattering in the normal region. Thus, a junction consisting of a normal conducting link between two superconductors (SNS junction) can become entirely superconducting if the normal region is sufficiently small, which is experimentally evidenced by a dissipationless current flowing across the junction, the so-called Josephson supercurrent. [110]

This supercurrent is affected by the electronic band structure of the normal conductor. Hence, the combination of a conventional superconductor with a non-trivial material can be utilized to fundamentally alter the superconducting pairing. On this basis one can "artificially" design a system that hosts quasiparticle excitations that on the one hand obey the massless Dirac equation and on the other hand are their own anti-particle (which requires them to be spin- and charge-neutral [11]), the two basic pre-requisites for the realization of Majorana bound states. Both conditions are met in a topological p-wave superconductor with spin-triplet pairing symmetry. [111] One of the proposed systems where the unconventional pairing between aligned spins (i.e., a spinless Cooper pair) can be realized is the spin-polarized surface state of a topological insulator coupled to an ordinary spin-singlet host superconductor. [11, 82]

In the following, we discuss the experimental approach to superconductivity induced into the topological insulator HgTe in a nanowire geometry. We therefore study the charge transport through SNS junctions based on CdTe–HgTe core–shell nanowires and Al as the host superconductor.

Superconducting nanowire junctions

In order to investigate the superconducting proximity effect in our HgTe nanowires, we contact them with Al-based electrodes. Aluminium is an ordinary type–I superconductor with a bulk critical temperature of about 1.2 K. [112] The electron beam lithography process is similar to the fabrication of the transport devices discussed in the previous chapter; details are given in the Appendix C. It should be pointed out that a high interface quality is crucial for the observation of a clear proximity effect. Thus, the thorough cleaning of the contact area from organic residues and oxide by Ar ion milling is directly followed by the subsequent contact metallization without breaking the vacuum in between. The contact electrodes are designed in a quasi–four–terminal geometry where the individual lines for current and voltage connect on top of the nanowire. The electrodes typically consist of a 5 nm-thick layer of Ti evaporated as an adhesion layer for the subsequently deposited

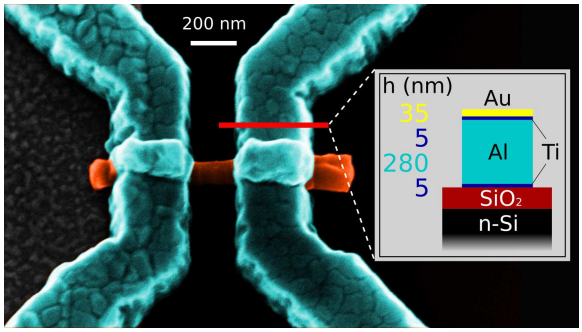

Figure 7.2: False-color electron micrograph of an SNS junction formed by a CdTe–HgTe core–shell nanowire (orange) connected to Al-based contact leads (turquoise). The inset sketches a vertical cut (red line) through the contact material stack on top of the SiO_2 substrate to denote the respective height h of the materials.

280 nm-thick Al superconductor, which is capped with 5 nm Ti and 35 nm Au. Figure 7.2 shows a scanning electron micrograph of an exemplary nanowire junction together with a schematic of the contact material stack.

Measurements of the superconducting properties of the contact electrodes give an average critical temperature of $T_c = 1.0 \pm 0.1\,\mathrm{K}$. This value is slightly reduced compared to the bulk critical temperature, which can be understood as a suppression of superconductivity due to the inverse proximity effect by the normal conducting part of the electrodes.[1] Using the BCS relation [107]

$$\Delta = 1.764\, k_B T_c \tag{7.1}$$

we can estimate a superconducting energy gap of $2\Delta = 0.30 \pm 0.03\,\mathrm{meV}$. Due to the geometry of the leads, the magnitude of the critical magnetic field depends on the orientation of the magnetic field. We observe different critical magnetic fields parallel ($B_{c,\parallel} = 10 \pm 2\,\mathrm{mT}$) and perpendicular ($B_{c,\perp} = 21 \pm 1\,\mathrm{mT}$) to the long axis of the nanowire.

In the following, we discuss the transport results obtained for nanowires that were tested in current-biased DC and standard lock-in measurements in a dilution refrigerator at a base temperature of about 30 mK. Cold low-pass RC filters are used to eliminate the possibility of spurious resonant features in the dynamic resistance. The samples were measured with specialized low-noise electronics in order to reduce the current noise rounding of the voltage–current characteristic. If not explicitely stated else, the measurements shown in this section are all acquired from the same device, SC-1, to ensure consistency. The results were qualitatively reproduced for further devices as can be seen from Tab. D.1 in the Appendix D.

[1] $1.2\,\mathrm{K} \cdot h_S/(h_N + h_S) = 1.2\,\mathrm{K} \cdot 280\,\mathrm{nm}/325\,\mathrm{nm} = 1.0\,\mathrm{K}$

Low-temperature voltage–current characteristic

First, we want to address the question whether superconducting pairing can be induced into our HgTe-based nanowires. An unambiguous sign of proximity induced superconductivity is typically found in the VI characteristic, where a Josephson supercurrent across the entire junction is evidenced by a zero–voltage plateau at low bias. Figure 7.3(a) shows the low-temperature VI characteristic of the nanowire junction SC-1. At low bias we indeed detect that the voltage drop for a finite current across the nanowire vanishes, which confirms the flow of an induced supercurrent. The transition between dissipationless and resistive regime is very sharp and of the order of the measurement resolution of about 0.1 nA. This is in contrast to a previous study of CdTe–HgTe nanowires in a standard dilution refrigerator setup, [14,45] where a high level of current noise resulted in the pronounced rounding of the VI characteristic and a finite low-bias resistance, which is shown as the red curve in Fig. 7.3(b). Thus, with adequate filtering we are now able to observe a clear superconducting transition, which is important for the accurate measurement of the critical current I_c in order to characterize the junction behavior.

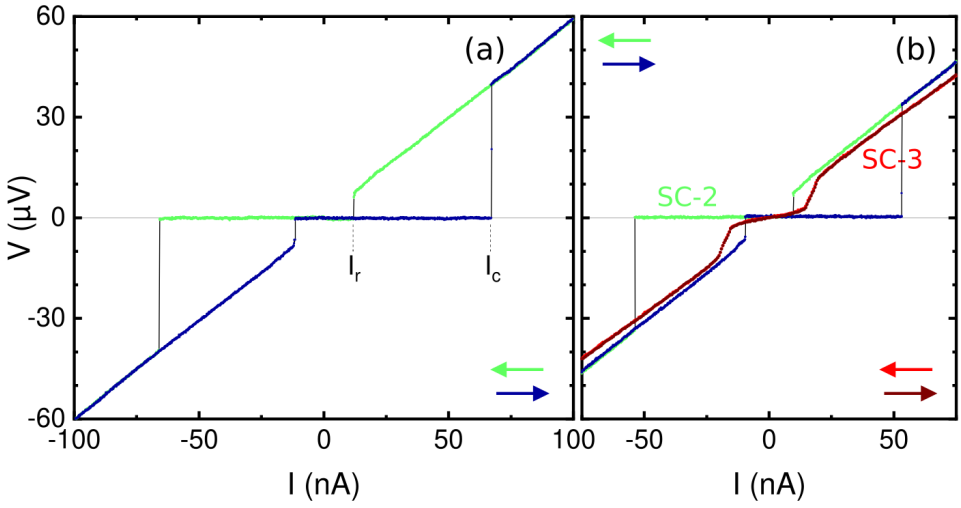

Figure 7.3: VI characteristics of CdTe–HgTe core–shell nanowires. Arrows indicate the sweep direction. (a) I_c and I_r mark the switching points at 66 and 12 nA between dissipationless and resistive transport for sweeps in positive (blue) and negative direction (green). (b) Comparison of two further samples, SC-2 and SC-3, measured in the noise-optimized setup (blue/green) and in a standard dilution refrigerator such as used in previous work [14,45] (brown/red), respectively.

From Fig. 7.3(a) one can infer a critical current value for the switching between superconducting and resistive regime of $I_c = 66\,\mathrm{nA}$. The retrapping current $I_r = 12\,\mathrm{nA}$, where the re-entrance into the superconducting state is observed, is significantly smaller compared to I_c. Such hysteretic behavior is a common observation in SNS junctions and can be understood as a result of an elevated electron temperature in the resistive regime, which sharply drops to the bath temperature upon entering the superconducting state. [113] If the noise level is too large, though, the system will undergo frequent jumps back to the resistive branch, which on the one hand can lead to a finite low-bias junction resistance and on the other hand may give rise to an elevated electron temperature even in the intrinsically superconducting state. Hence, no hysteresis is observed in the noise limited measurements [brown/red curve in Fig. 7.3(b)], as I_c is affected by the increased electron temperature and thus resembles the retrapping current rather than the critical current in the optimized measurements.

The strength of the proximity effect is characterized by the magnitude of the induced gap Δ_i, which depends on the relation between the superconducting coherence length ξ and the junction length L. In the short junction limit ($L \ll \xi$), Δ_i is of the order of the superconducting gap Δ in the contact electrodes and comparable to the product of critical current and normal state resistance $I_c R_n$, [114] whereas for long junctions ($L \gg \xi$) the Thouless energy $E_{Th} = \hbar D/L^2$ is the relevant energy scale, with D being the diffusion constant of the normal conductor. [115] The $I_c R_n$ product, which is also referred to as the characteristic voltage, is essentially independent of the cross-sectional area of the junction and can therefore serve as a figure of merit to compare different junctions. The value of R_n can be extracted from the slope of the VI characteristic at sufficiently large voltages to avoid any influence of quasiparticle transport by Cooper pairs (cf. Fig. 7.4). With $R_n = 1.01\,\mathrm{k\Omega}$ we calculate for the present sample a characteristic voltage of $I_c R_n = 67\,\mu\mathrm{V}$, which is comparable in magnitude to the gap value $\Delta/e = 150\,\mu\mathrm{V}$ of the contact electrodes. This suggests a reduced but still relatively large induced gap in the HgTe nanowire. Thus, the junction possibly lies between the limits of a short and long junction (i.e., $L \gtrsim \xi$). Measurements on different samples show values of the same order, which indicates a good reproducibility of the fabrication process [cf. Tab. D.1 in the Appendix D].

A linear extrapolation of the VI characteristic from the normal state at large bias – the red line in Fig. 7.4 – reveals a finite current offset at zero voltage, which is referred to as the excess current I_x. For the present sample we infer a substantial value of $I_x = 131\,\mathrm{nA}$. The excess current can be attributed to an enhancement of conductance at low bias due to quasiparticle transport by Andreev reflection. Andreev reflection is a scattering process at a transparent interface between a normal conducting material and a superconductor that can be schematically understood as the retro-reflection of an

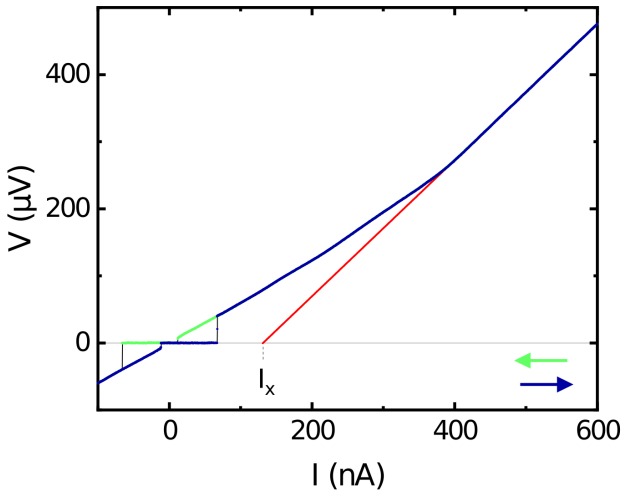

Figure 7.4: The same voltage–current characteristic as in Fig. 7.3(a), but up to a larger bias current. Arrows indicate the sweep direction. The red line is a fit to the data for $I > 550\,\mathrm{nA}$ with a slope of $R_\mathrm{n} = 1.01\,\mathrm{k\Omega}$. The extrapolation of the fit to zero voltage at 131 nA is labeled as the excess current I_x.

incident electron as a hole, which transmits a Cooper pair into the superconductor and therefore increases the total transferred charge. The magnitude of the excess current can be interpreted in the theoretical formulation of a phase-incoherent Josephson junction developed by M. Octavio, M. Tinkham, G. E. Blonder and T. M. Klapwijk (OTBK). [116] Within this framework, G. Niebler *et al.* [117] derived the analytical expression for the excess current

$$\frac{I_\mathrm{x}R_\mathrm{n}}{\Delta/e} = 2(1+2Z^2)\frac{\operatorname{arctanh}\left(2Z\sqrt{(1+Z^2)/(1+6Z^2+4Z^4)}\right)}{Z\sqrt{(1+Z^2)(1+6Z^2+4Z^4)}} - \frac{4}{3} \quad (7.2)$$

depending on the barrier parameter Z, which is related to the junction transparency by $\tau = 1/(1+Z^2)$. Taking $\Delta = 0.15\,\mathrm{meV}$, as inferred for the contact electrodes, we can calculate from Eq. 7.2 a moderately high transparency of about 0.7 for the respective nanowire junction. Considering the *ex situ* fabrication of the contact electrodes, this value implies a decent interface quality of our Al-based nanowire SNS junctions.

Modulation of the dynamic conductance

A close look at the VI curve in Fig. 7.4 indicates a slightly fluctuating slope at intermediate bias ($\sim$ 100–350 nA). This suggests a modulation of the conductance due to Andreev reflection processes, which we can probe in more

detail in the dynamic conductance dI/dV. In the following, we explain the basic principle of multiple Andreev reflection in SNS junctions before we discuss the experimental results. An in-depth theoretical study of multiple Andreev reflection is given by T. M. Klapwijk *et al.* [118]

Charge transport through a biased Josephson junction is strongly affected by the peculiar band structure of the superconducting electrodes. Depending on the voltage drop V across the junction, different transport regimes are realized as illustrated in Fig. 7.5. For $V > 2\Delta/e$, electrons with sub-gap energy from the first superconductor gain enough energy while traversing the junction to occupy vacant states above the gap of the second superconductor, resulting in normal single-charge transport [cf. Fig. 7.5(a)]. For $V < 2\Delta/e$, however, the energy gained across the junction is not sufficient to reach vacant single-particle states in the second superconductor. Hence, charge flow can only occur by Andreev reflection. This creates a Cooper pair in the second superconductor, as well as a hole with opposite momentum and energy with respect to the Fermi energy in the link. If the energy of the back-reflected hole after crossing the junction lies within the energy gap of the first superconductor it can be Andreev-reflected again. In a sufficiently transparent junction this can be repeated until a single-particle state is

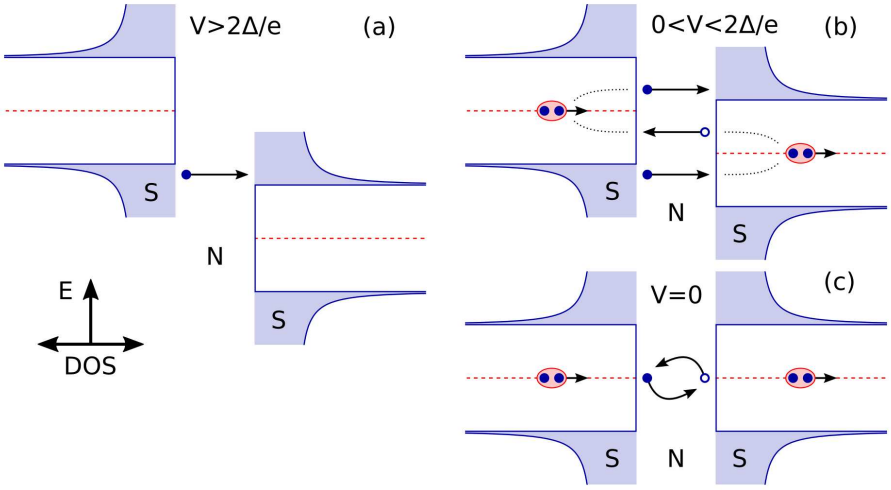

Figure 7.5: Illustration of quasiparticle transport processes across a superconductor–normal state conductor–superconductor (SNS) junction for varying bias voltage V: (a) $1e$ charge transport for $V > 2\Delta/e$, (b) $(n+1)e$ charge transport for n^{th} order multiple Andreev reflection processes at $0 < V < 2\Delta/e$, and (c) Andreev bound state at $V = 0$ resulting in a supercurrent flow. Filled and open dots resemble electrons and holes, respectively, and ellipses denote Cooper pairs.

reached, which is referred to as multiple Andreev reflection. Thereby an n^{th} order Andreev reflection process opens up at $V = 2\Delta/ne$, with $n \in \mathbb{N}$. The corresponding generation of further quasiparticles leads to additional charge being carried by higher-order Andreev processes, which affects the conductance of the junction. As an example, Fig. 7.5(b) illustrates a second-order Andreev reflection process that transfers a charge of $3e$ via a Cooper pair and a single electron. Finally, at $V = 0$ a bound state is formed that allows to transfer Cooper pairs directly from one superconductor to the other. Hence, one can expect a constant normal-state resistance at high bias, a set of features related to multiple Andreev reflections at values of $2\Delta/ne$, and a sharp increase in the current flow due to the formation of an Andreev bound state close to zero bias.

In order to test for the expected transport signatures we now investigate the evolution of the dynamic conductance dI/dV with the voltage drop across the nanowire junction. Figure 7.6 shows the result. Coming from a large voltage value, we first observe a constant conductance value. At around 280 µV the conductance increases, which can be interpreted as the opening of the first-order Andreev reflection channel at the gap voltage $2\Delta/e$. This is in good agreement with the energy gap calculated from the critical temperature of the contact electrodes (300 µeV). Intuitively, subsequent increases in conductance should thus be observed at values of $1/n \cdot 280\,\mu\text{V}$ as predicted by the OTBK theory, [119] indicated by the gray lines in Fig. 7.6. While the $n = 2$ feature is well matched, we observe shifts for $n \geq 3$.

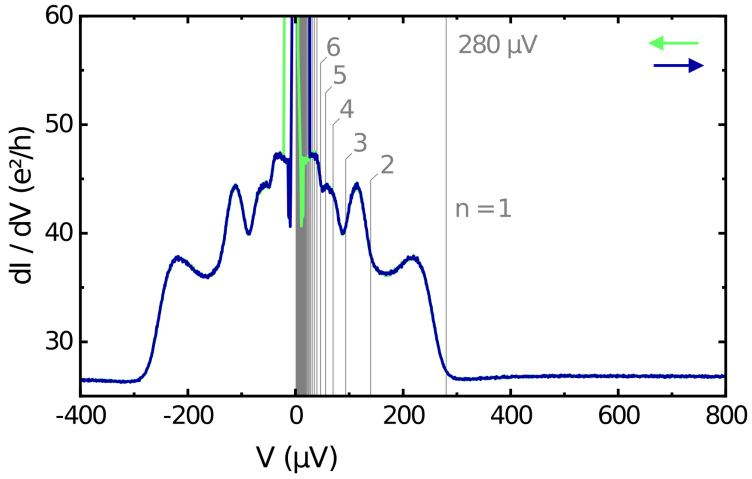

Figure 7.6: Dynamic conductance of a CdTe–HgTe core–shell nanowire depending on the voltage drop across the junction. Arrows indicate the sweep direction. Vertical gray lines mark $1/n$–fractions of the voltage of 280 µV where the outermost feature starts to appear.

Shifts of Andreev reflection-related features from the expected $1/n$ period are a common experimental observation. [121,122] One possible explanation arises from the consideration that transport in semiconductor SNS junctions might not be sufficiently well described in the limit of fully incoherent transport assumed by the OTBK theory, which does not keep track of the quasiparticle phase. Rather, it is reasonable to expect an intermediate regime where the junction length is smaller than the electron phase coherence length (validated by the observation of phase coherent magnetotransport in Section 6.2), but larger than the superconducting coherence length of the induced Cooper pairs. J. C. Cuevas *et al.* [120] showed that in this regime the interplay between Δ_i and Δ – characterized by the ratio L/ξ of junction length and superconducting coherence length – can give rise to a rich variety of the subgap structure as depicted in Fig. 7.7. In order to compare our results to the numerical calculation, we need to classify our sample with respect

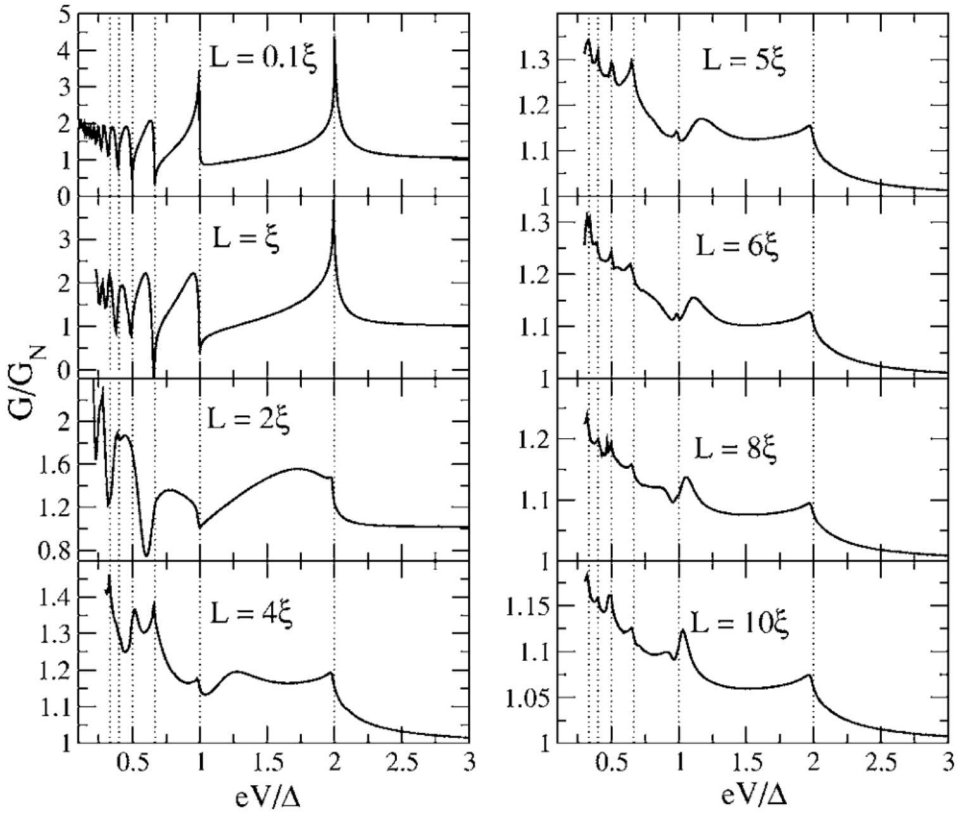

Figure 7.7: Normalized conductance in the intermediate regime of phase coherent transport through a Josephson junction, depending on the ratio L/ξ of junction length and superconducting coherence length. The image is taken from J. C. Cuevas *et al.* [120]

to the L/ξ ratio. This can be done via the excess current. The numerical dependence between the excess current and L/ξ [120] can be approximated for $I_\mathrm{x}R_\mathrm{n} \leq \Delta/e$ quite accurately by the analytical expression

$$\frac{I_\mathrm{x}R_\mathrm{n}}{\Delta/e} = \frac{2.55}{L/\xi + 0.3}\,. \tag{7.3}$$

With the experimental value of $I_\mathrm{x}R_\mathrm{n} = 0.95 \cdot \Delta/e$ for the respective nanowire junction we can use Eq. 7.3 to estimate $L/\xi = 2.4$, taking $\Delta = 0.14\,\mathrm{meV}$ as inferred from the position of the first feature in Fig. 7.6. The calculated subgap structure for the closest value shown in Fig. 7.7, $L/\xi = 2$, is characterized by the following points: The first (outermost) broad maximum is shifted to lower values compared to 2Δ, which can be interpreted as the result of an interplay with the induced gap $2\Delta_\mathrm{i}$ of reduced magnitude $2\Delta > 2\Delta_\mathrm{i} > \Delta$. [120] The second maximum lies between $2\Delta/2e$ and $2\Delta/3e$. The third maximum, which appears to be merged from two individual features, spans between $2\Delta/4e$ and $2\Delta/5e$. After a minimum at $2\Delta/6e$, the fourth maximum appears at a voltage below. Comparing these characteristics to the measurement in Fig. 7.6 shows surprisingly good qualitative agreement. This suggests that our device is described well by phase coherent transport through a semi-diffusive Josephson junction with a length that exceeds the superconducting coherence length by roughly a factor of two.

Magnetic field dependence

In order to characterize the proximity gap we now investigate its dependence on the experimental parameters magnetic field and temperature. First, we discuss the influence of an external magnetic field applied perpendicular to

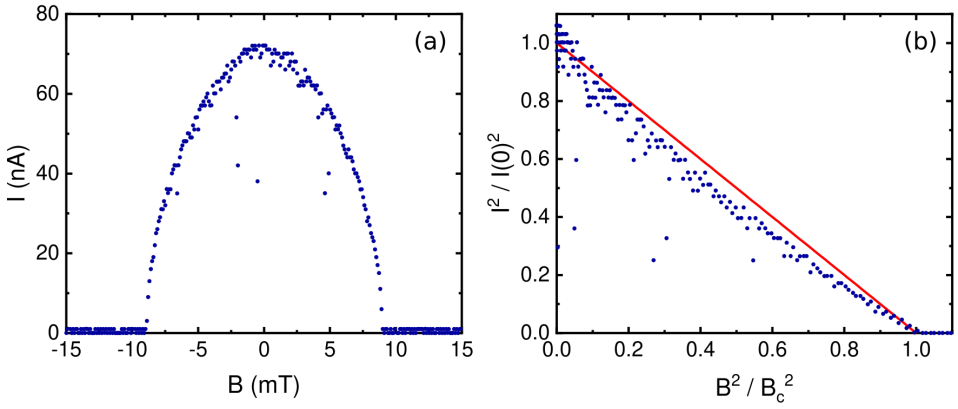

Figure 7.8: (a) Magnetic field dependence of the critical current I_c. (b) Linearized representation of the data with respect to Eq. 7.4, which is indicated as the red line.

the nanowire axis. For pure Al films it was shown that the B-dependence of the superconducting energy gap Δ is well described by the equation

$$\left(\frac{\Delta(B)}{\Delta_0}\right)^2 = 1 - \left(\frac{B}{B_c}\right)^2 \tag{7.4}$$

as long as the sample dimensions are smaller than the effective London penetration depth λ_L, which defines the lengthscale of the exponential suppression of the magnetic field. [123] Figure 7.8 shows the experimental dependence of the critical current with magnetic field applied parallel to the nanowire axis. From Fig. 7.8(a) we can infer that I_c reaches zero at a critical magnetic field of about $\pm 8\,\mathrm{mT}$, which coincides with the value of $B_{c,\parallel} = 10 \pm 2\,\mathrm{mT}$ observed for the superconductivity in the electrodes. Plotting the square of the normalized critical current $[I_c/I_c(0)]^2$ versus the square of the normalized B-field $[B/B_c]^2$ in Fig. 7.8(b) gives a linearized representation of the relation Eq. 7.4. From Fig. 7.8(b) one can infer that the critical current is in good agreement with Eq. 7.4 (red line).

We can further compare this to the magnetic field scaling of the features associated with Andreev reflection. Figure 7.9 shows the B-dependent dynamic conductance dI/dV. The line profile for $B = 0$ in Fig. 7.9(a) highlights the expected position of the $n = 1$–3 Andreev features at zero field in analogy to Fig. 7.6. The color coded map in Fig. 7.9(b) indicates that the voltage

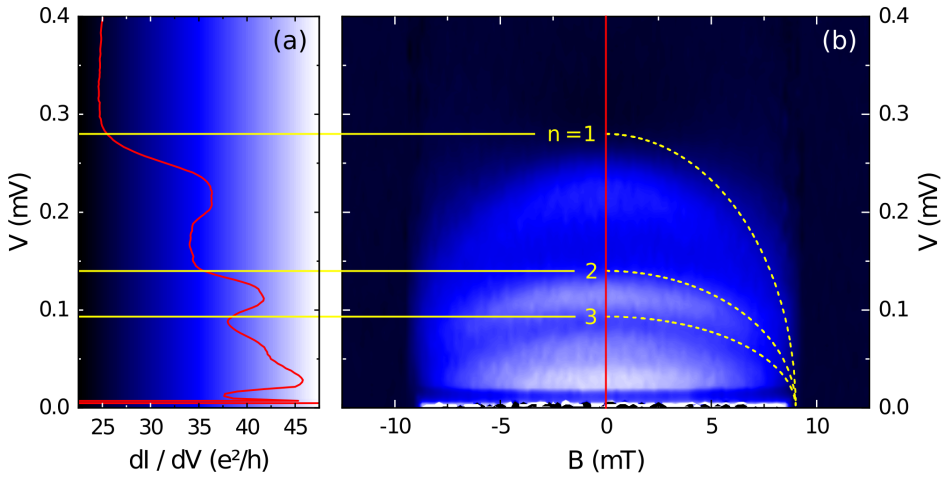

Figure 7.9: Magnetic field dependence of the bias voltage dependent dynamic conductance dI/dV, calculated as the derivative of the VI characteristics for different B-fields. (a) shows a line profile for $B = 0$. The background of (a) indicates the color code for dI/dV in the B-dependent map depicted in (b). Yellow dashed curves resemble a fit with Eq. 7.4 for $1/n \cdot 2\Delta/e$, with $\Delta = 0.14\,\mathrm{meV}$.

position of these features changes with B according to Eq. 7.4, overlaid as the yellow dashed curve, which matches the scaling of the critical current. From this we may conclude that an external magnetic field has a similar effect on the proximity superconductivity compared to the parent superconductor in the contact electrodes.

Temperature dependence

We now turn to the temperature dependence of the induced superconductivity. Figure 7.10 shows the critical current I_c (blue dots) and the retrapping current I_r (light green dots) measured during a warmup of the sample. The temperature in this measurement increased rather countinuously up to 0.64 K – the visible data range in Fig. 7.10 – followed by a jump to about 1.4 K (not shown). The overall trend in Fig. 7.10(a) shows that with increasing temperature the value of I_c and I_r reduces until both are fully suppressed at an extrapolated value of about 0.7 K. Comparing this to the critical temperature $T_c = 1.0\,\mathrm{K}$ of superconductivity in the Al electrodes suggests that the size of the induced gap Δ_i is reduced but still of the order of Δ, as already indicated by the magnitude of the characteristic voltage $I_c R_n$. The hysteretic behavior of the VI curve ($I_c > I_r$) remains up to a relatively high temperature of about 0.6 K. Assuming current heating as the origin, we can thus infer an electron temperature of about $T^\star = 0.56\,\mathrm{K}$ in the dissipative regime, defined by

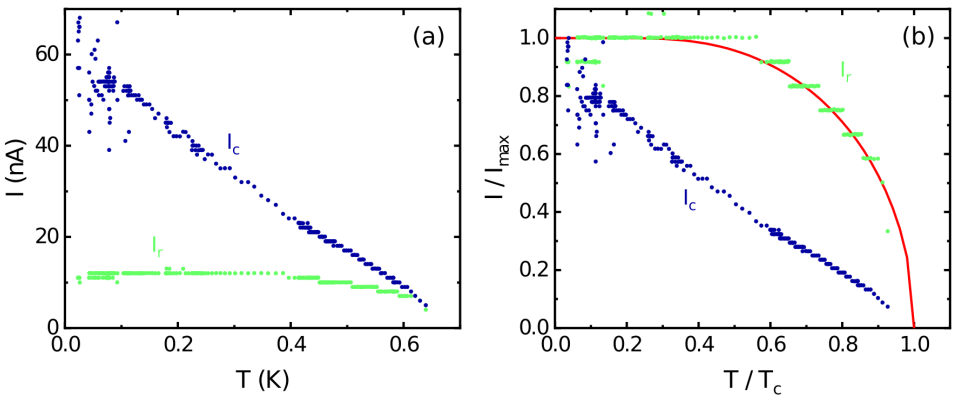

Figure 7.10: (a) Temperature dependence of I_c and I_r. (b) Normalized representation of (a) with respect to the according maximum current value close to base temperature and the extrapolated critical temperature T_c (0.72 K for I_c, 0.68 K for I_r), plotted together with the BCS temperature dependence of the superconducting gap (red line, numerical data taken from B. Mühlschlegel [124]). Steps in the data that are visible particularly in I_r are due to a limited resolution of 1 nA in the VI curves.

$I_c(T^\star) = I_r(0)$. [113] Such a rather high electron temperature seems feasible when considering the low efficiency for heat dissipation due to the poor thermal coupling to the insulating substrate and the low thermal conductance of the superconducting electrodes that extend all the way from the nanowire to the bondpads.

Despite their comparable critical temperature, I_c and I_r differ strongly in the temperature dependence. This is seen very clearly in the normalized representation of the data shown in Fig. 7.10(b). The retrapping current is fairly well described by the BCS temperature dependence of the superconducting gap [red curve in Fig. 7.10(b)], [124] which suggests a strong link to the closing of the superconducting gap in the system. The critical current, however, shows an entirely different dependence and scales almost linearly with temperature.

In order to understand the peculiar temperature dependence of I_c, we need to consider the influence of Andreev bound states on the critical current as described in the following paragraph based on work by H.-J. Kwon *et al.* [125] In a conventional SNS junction with spin–singlet (s-wave) pairing the spectrum of Andreev bound states consists of the two subgap states

$$E_\pm^{(s)}(\varphi) = \pm\Delta\sqrt{1 - \tau\sin^2(\varphi/2)}\,, \tag{7.5}$$

plotted in the upper panel of Fig. 7.11(a). In the ballistic case ($\tau = 1$, black curve) the spectrum is gapless with the bands touching at odd integer multiples of π, whereas for a reduced junction transparency (blue curve) an energy gap evolves that splits the spectrum into ground and excited state.

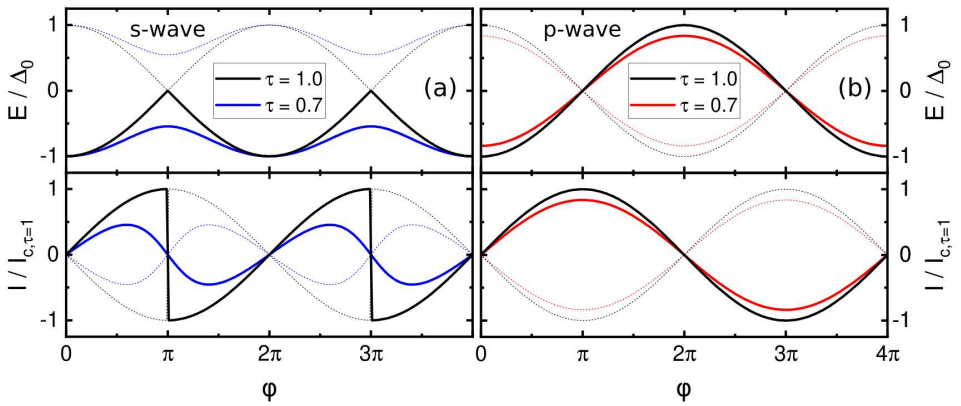

Figure 7.11: Phase evolution of the Andreev bound state spectrum (upper panels) and the associated current (lower panels) of an SNS junction with (a) s-wave and (b) p-wave pairing. Thin and thick curves denote the two different subgap states $E_\pm$, respectively.

The contribution of an Andreev bound state to the current flow can be described by

$$I(\varphi) = -\frac{2e}{\hbar}\frac{\partial E(\varphi)}{\partial \varphi}\tanh\left(\frac{E(\varphi)}{k_{\mathrm{B}}T}\right) . \tag{7.6}$$

Inserting Eq. 7.5 into Eq. 7.6 we can plot the s-wave current–phase relation as shown in the lower panel of Fig. 7.11(a), which is essentially a 2π-periodic function of phase.

For SNS junctions with an unconventional p-wave pairing symmetry, such as expected for superconductivity induced into the surface states of a topological insulator, [82] the situation is fundamentally different. There, the Andreev bound state spectrum consists of the two subgap states

$$E_{\pm}^{(\mathrm{p})}(\varphi) = \pm\Delta\sqrt{\tau}\cos(\varphi/2)\,, \tag{7.7}$$

depicted in the upper panel of Fig. 7.11(b). From this we can calculate via Eq. 7.6 the current–phase relation shown in the lower panel of Fig. 7.11(b). Due to the conservation of fermion parity, the two $E_{\pm}^{(\mathrm{p})}$ subgap states the crossing at $\varphi = \pi$ is protected, contrary to the ballistic case in a conventional material. Hence, the p-wave current–phase relation is expected to be robustly 4π periodic.

In order to calculate the critical current at a given temperature we need to maximize $I(\varphi)$. For the simulation, shown in Fig. 7.12, we use the BCS temperature dependence for $\Delta(T)$ [124] scaled by the value of the

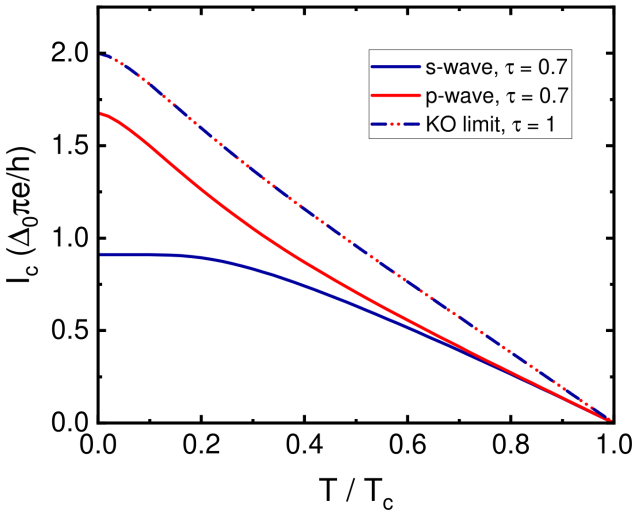

Figure 7.12: Theoretical temperature dependence of the critical current of an s- and p-wave SNS junction for two different Andreev transmission probabilities of $\tau = 0.7$ and 1.

induced pairing potential $\Delta_i = 0.11\,\mathrm{meV}$, which is calculated with the BCS relation Eq. 7.1 from the extrapolated critical temperature of 0.72 K for the suppression of the critical current in Fig. 7.10(a). As an estimate for τ we take the junction transmission of 0.7 derived from the excess current. In a conventional s-wave junction, the blue line in Fig. 7.12, $I_c(T)$ shows a markedly non-linear behavior with a marginal decrease up to a reduced temperature of about 0.2 that changes to a steeper slope at higher temperature. Towards the ballistic limit ($\tau \to 1$, dashed–dotted line), named after I. O. Kulik and A. N. Omel'yanchuk (KO), [126] $I_c(0)$ increases and the curve appears almost linear. In the p-wave case, however, a different behavior is observed. While the KO limit is the same as for a conventional junction, a positive curvature appears for reduced transmission in the intermediate temperature range (cf. red line in Fig. 7.12). Interestingly, a qualitative comparison to the experimental data in Fig. 7.10 indicates that the observed $I_c(T)$ may be explained better by the ballistic or the p-wave case rather than by transport through a conventional (semi-)diffusive SNS junction.

In order to compare the model quantitatively we need to take the possible presence of multiple Andreev bound state modes into account, which would contribute to the current flow in parallel. I_c is then obtained by maximizing the sum of the individual contributions to $I(\varphi)$, assuming the same phase difference for all Andreev bound states. For the given experimental parameters, a single bound state at $T \to 0$ would carry approximately 12 and 22 nA in the s- and p-wave $\tau = 0.7$ regime, respectively, and approximately 27 nA in the KO limit, which is on average a factor of three smaller compared to the experimental value of about $I_c = 66\,\mathrm{nA}$. From this we may indeed conclude multi-modal contributions to the critical current. In order to fit the data quantitatively we need to consider not only the absolute value of the critical current at $T \to 0$, but also the overall temperature dependence. Figure 7.13 shows the results obtained for a pure s-wave and p-wave fit. In both cases we assume that three Andreev bound states contribute with the same average transmission τ. A decent fit with the s-wave model requires to increase τ significantly beyond the experimentally estimated average value in order to account for the general shape of the model curve. The ballistic limit – the best qualitative match based on s-wave pairing – would overestimate the absolute value of I_c, though. Thus, $\tau = 0.9$ could give a reasonable compromize (cf. blue line in Fig. 7.13). Still, the model lacks to describe the positive curvature at intermediate temperature and underestimates the low-temperature value of I_c.

In contrast, the p-wave model (red line in Fig. 7.13) describes the data surprisingly well, both qualitatively and quantitatively – already with the experimentally determined set of parameters (except for the number of Andreev bound states). While the origin of the I_c fluctuations at $T < 0.12\,\mathrm{K}$ is not yet understood, the spontaneous suppression of the supercurrent to a

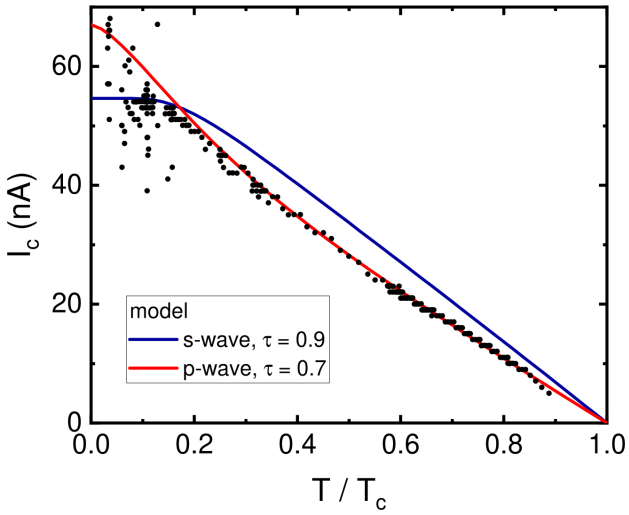

Figure 7.13: Experimental $I_c(T)$ fitted with a quantitative model for s-wave (blue line) and p-wave (red line) transport, assuming the contribution of three Andreev bound states with an average transmission value as denoted.

lower value seems more reasonable than a jump to a value above the expected one, which might further corroborate the validity of the p-wave model that runs along the upper limit of the fluctuating data points.

However, it should be strongly emphasized that the analysis of $I_c(T)$ is based on a simplified model that may or may not be an adequate representation of reality. In particular, it is unclear why a number of three Andreev bound states would occur in a system with probably many more conductive modes.[2] Taking the same average transmission probability for all bound states involved is also most certainly an oversimplification. Further, previous experiments indicate the coexistence of s- and p-wave modes in topological SNS junction based on HgTe thinfilms. [127] Hence, it seems unlikely that in our nanowire junctions only p-wave modes would contribute to the supercurrent, although in principle additional trivial s-wave modes might still be present but with a low transmission probability that effectively does not alter the observed critical current by a meaningful amount. In order to draw more substantial conclusions about an eventual p-wave pairing in the nanowire junctions it might be promising to investigate the dynamic response of the system, which could allow to experimentally confirm the 4π-periodicity of the current–phase relation as reported by J. Wiedenmann *et al.* for HgTe thinfilm SNS junctions. [127] Hence, we study in the following our nanowire junctions under excitation with a microwave signal.

[2] From $R_n = h/(2e^2 N\tau)$ [125] we can estimate approximately $N = 18$ modes.

7.2 Shapiro steps under microwave irradiation

The AC response of an SNS junction is commonly investigated by the coupling to a radio frequency (RF) signal. B. Josephson [110] predicted the occurrence of regions with constant voltage in the voltage–current characteristic of superconducting tunnel junctions at integer multiples of $hf/2e$, depending on the frequency f of the AC excitation, which was experimentally confirmed by S. Shapiro [128] in the following year. The phase-locking effect that leads to these so–called Shapiro steps can intuitively be understood considering the commonly used analogy of a phase particle that moves along a tilted washboard potential, which oscillates with the AC driving frequency. [129] The phase periodicity of the Andreev bound state spectrum has a fundamental influence on the dynamic response of the SNS junction. [130] Hence, the manifestation of the Shapiro steps can provide valuable insight into the nature of the proximity induced superconducting order, and is thus an important approach to probe for topological superconductivity. In particular, it was shown that a 4π-periodic contribution to the supercurrent can result in a suppression of Shapiro steps with odd indices, i.e., only steps at integer multiples of hf/e are expected in that case. [131]

In this section we address the question if, and in which parameter range, we are able to observe Shapiro steps in our nanowire SNS junctions. For this purpose, we analyze the VI characteristics of sample SC-4, a nanowire junction of the same type as discussed in Section 7.1, coupled to an RF signal.

HgTe nanowire shells under microwave irradiation

In order to investigate how microwave irradiation affects the VI characteristic of our nanowire SNS junctions we use the same low-noise measurement setup as for the previous section, but with an additional coaxial RF line fed to the sample chamber through various attenuators that are thermally anchored at different temperature stages of the dilution refrigerator. The open end of the coaxial cable is placed in close proximity to the sample and serves as an antenna for the microwave signal. With this, we achieve decent coupling in the relevant frequency range of the order of gigahertz. The coupling strength is not calibrated; thus, the absolute RF power sensed by the sample varies with the freqency and can be influenced by factors such as the cavity resonances of the sample chamber.

We begin with a frequency of 5.5 GHz, corresponding to a photon energy of 23 µeV, which is sufficiently small to stay well within the coherent energy window $hf < \Delta_i$. [132] Figure 7.14 compares the results obtained for two different values of the RF output power P. At low power, the blue curve in Fig. 7.14(a), we reproduce the characteristics of an undisturbed SNS junction – a pronounced zero–voltage plateau linked to the flow of a supercurrent that

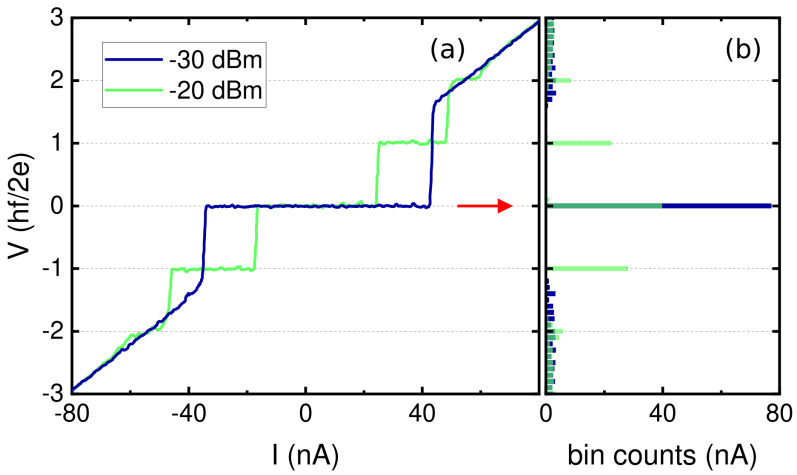

Figure 7.14: (a) Voltage–current characteristic of a nanowire SNS junction under 5.5 GHz microwave illumination with an output signal power of −30 dBm (blue) and −20 dBm (light green). (b) Histogram of the respective voltage bin count. The bin count is a measure of the span of a constant-voltage plateau in the VI characteristic and thus given in units of current.

switches to a resistive state above a certain critical current value. In this case, the power coupled into the junction is not large enough to influence the junction dynamics. At larger power, the light green curve in Fig. 7.14(a), additional voltage plateaus occur at integer multiples of $hf/2e$. From this we can conclude that we are indeed able to observe Shapiro steps in our nanowire junctions. In order to analyze the Shapiro steps further, it is practical to bin the data with respect to the voltage drop across the sample. That way, the Shapiro steps cause a high count rate that is visible as a peak in the bin count plot, Fig. 7.14(b), which allows for a more convenient visualization of the VI data in the following investigation.

Fractional Shapiro steps

The evolution of the Shapiro steps with RF power can be displayed as a color map of the voltage bin count. First, we investigate how the sample reacts to higher RF frequencies. Figure 7.15 shows the bin count at 7.78 GHz. From the power dependent bin count map, Fig. 7.15(a), one can infer pronounced and clear Shapiro steps at integer multiples of $hf/2e$. In addition, indications of steps are visible at half-integer positions in between as pointed out by the arrow. These fractional Shapiro steps are also directly visible in the VI curves, such as shown in Fig. 7.15(b) for an exemplary RF power of −12 dBm. Fractional Shapiro steps are typically observed for higher excitation

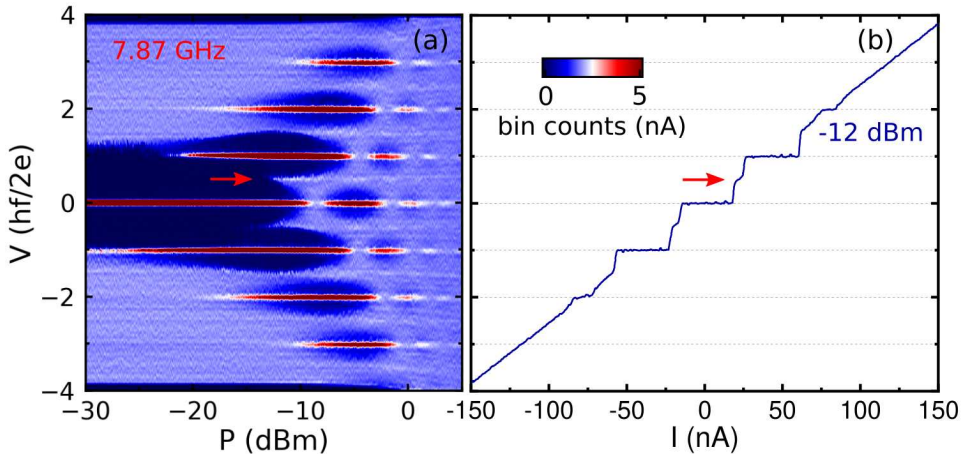

Figure 7.15: (a) RF power dependence of the voltage bin count histogram for $f = 7.87\,\mathrm{GHz}$. For clarity, the color code clips values above 5 nA. (b) Exemplary VI curve at $P = -12\,\mathrm{dBm}$. Arrows point out the position of a half-integer fractional shapiro step at $V = hf/4e$.

frequencies and are in general seen as a fingerprint of a non-sinusodial current–phase relation, which is found for example in sufficiently transparent SNS junctions. [133, 134]

Suppression of Shapiro steps

Now, we turn to lower RF frequencies. Figure 7.16 shows bin count maps for frequencies in the range of 0.9–2.0 GHz. At 2.0 GHz we observe a regular Shapiro step pattern, just the power range where a particular step is visible is reduced compared to 7.78 GHz in Fig. 7.15(a). This becomes even more evident when comparing the plots for 1.2 and 2.0 GHz. Below 1.2 GHz we find that the intensity of the $n = 1$ step for both positive and negative voltage – marked by the arrows in Fig. 7.16 – reduces until it disappears at around 1.025 GHz. Below 0.975 GHz, however, the step begins to reappear until it is back at a similar intensity compared to the $n = 2$ step at 0.9 GHz. The suppression seems to affect only the first bin count maximum at low RF power and does not influence the oscillatory region at higher RF power, the so–called Bessel regime.

A missing first order Shapiro step is an intriguing observation, as it suggests a change in the periodicity of the current–phase relation in the first place. Such an observation has been reported for several material systems so far and can in principle be caused by different effects, which we discuss in the following.

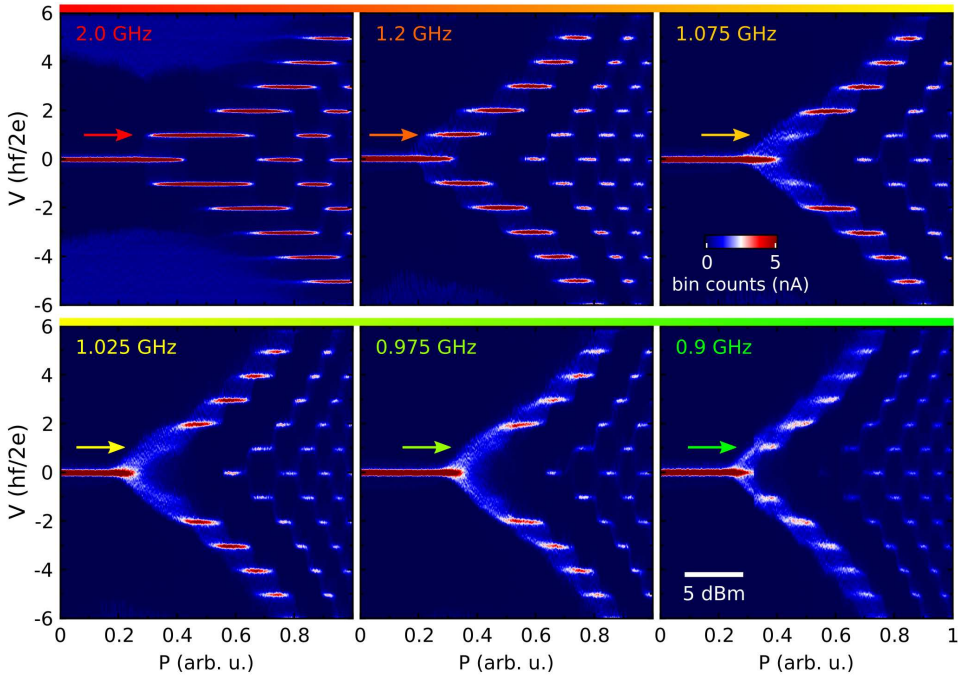

Figure 7.16: RF power dependence of the voltage bin count histogram for frequencies in the range of 0.9–2.0 GHz as denoted. For clarity, the color code clips values above 5 nA. Arrows point out the position of the first-order shapiro step at $V = hf/2e$.

First, missing lower-order Shapiro steps can have a trivial origin in the presence of hysteresis in the VI characteristic. In this case, the voltage can jump directly from zero to about the characteristic voltage $I_c R_n$, which was observed in Nb–Au–Nb junctions. [135] However, the characteristic voltage of our device, about 26 µV, is many times larger than the $n = 2$ Shapiro step voltage of 4 µV for a frequency of about 1 GHz, from which we should expect the suppression of significantly more steps, not just the first one. Further, this effect results in the suppression of steps in only the positive (supercurrent) branch of the VI curve, whereas the negative (retrapping current) branch is unaffected. That is distinctly different to our case, where the first step is missing symmetrically in both the positive and the negative branch (cf. Fig. 7.16). Thus, we can likely exclude a hysteresis-related effect as the origin of the suppressed first Shapiro step.

Then, a missing first step may be the result of a 4π-periodic current–phase relation, which could arise either from an actual 4π-periodic unconventional Andreev spectrum, such as for a topological superconductor, or from Landau–Zener transitions in conventional 2π-periodic bound states. Landau–Zener transitions in this context can be understood as the crossing

between the ground and excited Andreev bound state levels at $\varphi = (2n+1)\pi$ [cf. Fig 7.11(a)], $n \in \mathbb{N}$, which may occur for a sufficiently small excitation gap between the two Andreev levels (i.e., in highly transparent junctions with $\tau \to 1$). [131] At first glance, the quasi-ballistic case appears to be unlikely ours. However, a recent experiment on transparent Al–InAs–Al junctions suggests that already the presence of only few quasi-ballistic modes, which may undergo a Landau–Zener transition, can result in a clear suppression of odd Shapiro steps despite the prescence of a much larger amount of 2π-periodic modes with low transmission. [136] This conclusion is supported by numerical calculations for current-biased SNS junctions, [131] which suggest a predominant influence of 4π-periodic modes on the entire dynamic response in a frequency range of $f_{4\pi} \lesssim 2eI_{4\pi}R_\mathrm{n}$, with $I_{4\pi}$ being the contribution of the 4π-periodic modes to the critical current. It should be noted, that in both cases – parity protected unconventional 4π-periodic bound state spectrum or ballistic 2π-periodic mode that undergoes a Landau-Zener transition – one would expect to see a suppression of odd steps in general, not just of the first order. However, it is known that a finite junction capacitance can lead to a strong quenching of the first order Shapiro resonance only, whereas higher-order steps are less affected. [137] This preferential suppression can explain the common experimental observation of a missing first step only. [138, 139]

Finally, we consider an eventual spurious effect of resonances in our system. In order to do so, we compare in Fig. 7.17 the suppression of the first Shapiro step – quantified as the quotient of the maximum bin count value for first and second step, Q_{12} – to the power dependence of the vanishing

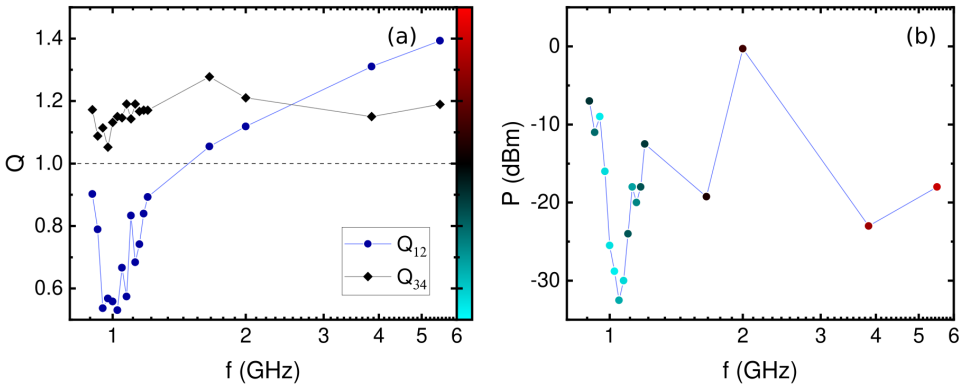

Figure 7.17: (a) Quotients Q_{12} (blue) and Q_{34} (black) between the maximum bin count of first and second, and third and fourth Shapiro step, respectively. The color bar codes the value of Q_{12} in (b). (b) Frequency dependence of the minimum RF power required to suppress the bin count at $V = 0$ (corresponding to the critical current) below a threshold of 2 nA.

supercurrent as a measure of the coupling efficiency for various frequencies investigated. From Fig. 7.17(a) we can infer that at high frequencies Q_{12} (blue dots) is clearly larger than one (dashed line), i.e., the first Shapiro step is more pronounced than the second. The same holds for Q_{34}, the ratio between third and fourth step. Towards lower frequency Q_{12} reduces considerably, reaching a minimum value of about 0.5 at around 1 GHz, whereas Q_{34} remains at approximately the same value. It is now interesting to compare if the suppression of the first step might be related to a resonant coupling to the RF signal. Figure 7.17(b) shows the RF power where the supercurrent bin count is first reduced to below 2 nA, which can be seen as an estimate of the coupling efficiency to the AC drive. The lowest values (i.e., the strongest coupling) are also found close to 1 GHz, which might indicate a resonance within the system for this particular frequency range. However, a closer look at the color code, which resembles the magnitude of Q_{12}, shows that there is no clear correspondence to the suppression of the first Shapiro step. In particular, the lowest values of Q_{12} (below 0.6, light turquoise data points) span over a wide power range of P between -30 and -9 dBm, and the large fluctuation in P at higher frequency does not reflect in Q_{12}. While this is certainly not sufficient to safely exclude any relation between the missing first step and some sort of a resonant coupling, the fact that we observe the missing first step over a wide range of the coupling strength makes it less likely. Thus, a 4π-periodic contribution to the current–phase relation appears to be the more likely origin, which would be in line with the experimental evidence found in three-dimensional HgTe thinfilm SNS junctions. [127] Then, however, the reappearance of the missing Shapiro step at low frequencies (cf. bottom right image in Fig. 7.16) is unexpected, and a possible reason for this is not known so far.

Overall, we were able to induce superconducting pairing in our nanowires. Beyond the characterization of various basic properties we find a behavior that appears to be untypical for a convential SNS junction in both the DC and AC characteristics. These observations could be explained by the presence of topological superconducting pairing – although it is important to emphasize that a trivial origin can not be safely ruled out so far. Hence, the results of this transport investigation provide an important step towards the understanding of the nature of superconducting pairing induced into our HgTe nanowires, but further experiments are required for a conclusive picture.

Overview of Part II

In Part II of this thesis we study the charge transport in our HgTe based core–shell nanowires. The focus lies on a basic characterization of two distinct effects, quantum interference and proximity induced superconductivity. With these effects we aim to probe the main attributes of our samples – the electronic structure of the topological material HgTe on the one hand, and the quantum effects related to the low dimensionality on the other.

In Section 6.1 we study quantum interference effects in the magnetoconductance in order to characterize the quality of the different growth regimes discussed in Part I of this thesis. The clearest and most regular magnetoconductance oscillations are found in ZnTe–CdTe/HgTe core–shell nanowire heterostructures where HgTe is grown in the step-flow regime. The oscillation frequency matches a flux periodicity of h/e over an extensive number of oscillation periods. This is a distinct fingerprint of the Aharonov–Bohm effect that is expected to occur only in samples with a low density of scattering sites. [94] Hence, we conclude that the improvements in the nanowire growth bring a crucial increase of the sample quality for charge transport.

The pronounced magnetoconductance oscillation signal in these optimized nanowires allows us to probe the Aharonov–Bohm effect in more detail, which is discussed in Section 6.2. There, we find two main observations: First, both the oscillation amplitude and the power spectral density of the main oscillation frequency increase with an increasing positive gate voltage (i.e., when shifting the Fermi energy further into the conduction band). And second, the spectral analysis of the oscillation frequency points to a radial distribution of the electronic states that contribute to magnetotransport, which is localized close to the inner surface of the HgTe shell within an average band of the order of 10 nm. On the one side, these observations can be explained as a result of charge transport mediated by bulk states in the HgTe shell. In this case, though, one would expect a broader frequency spectrum that spans the entire equivalent shell thickness of about 35 nm. However, an increase of the defect density at the surface due to oxidization or the lithographic processing could suppress contributions from the outer region. On the other side, the results can be interpreted as the signature of a slightly delocalized surface state at the inner interface to the nanowire core. The missing contribution of the

outer surface state can again be explained by environmental influence on the unprotected outer interface. A reduced oscillation amplitude towards lower gate voltage may result from an increasing probability for scattering with holes from the bulk valence band. Overall, both scenarios offer a plausible explanation for the observed magnetoconductance signal. Anyways, the ZnTe-based nanowire heterostructures so far proved to be a very promising platform for the investigation of the Aharonov–Bohm effect in HgTe.

Further, in Section 7.1 we demonstrate clear evidence for proximity induced superconductivity in our HgTe nanowires, the first important step towards the prospective realization of Majorana bound states in a topological system as a possible alternative to the more common Rashba semiconductor nanowire platform. [102, 140, 141] With careful filtering of the measurement setup we are able to prevent current-noise rounding and a suppression of the supercurrent. This allows for a quantitative investigation of the induced superconductivity. The results suggest that our Al-contacted nanowire devices are relatively clean and lie in between the limits of short and long junctions. Further, they are characterized by a decent transparency of about 0.7, and a junction length that is smaller than the phase coherence length and slightly larger than the superconducting coherence length. Intriguingly, a detailed analysis of the temperature dependence of the supercurrent indicates a significantly better agreement with a primitive model based on either highly transparent modes or on an unconventional pairing potential, compared to the result for a semi-diffusive conventional s-wave junction. A similar observation was made in topological Bi_2Te_3 SNS junctions, where the observed temperature dependence of I_c shows ballistic behavior, despite that the normal state transport is dominated by low-mobility bulk transport. [142] From this, the authors conclude the presence of few high-transparency modes, interpreted as the topological surface states. To test if a similar situation is present in our samples requires further experiments in order to gain a deeper understanding of the nature of the induced superconductivity.

Finally, in Section 7.2 we study the response of our nanowire SNS junctions to the dynamic excitation with a microwave signal. At frequencies of about 0.9 GHz and higher we are able to resolve distinct plateaus of constant voltage in the voltage–current characteristics, the so-called Shapiro steps. For the highest frequency under investigation, 7.87 GHz, we find indications for fractional Shapiro steps at half-integer multiples of the typical voltage spacing $hf/2e$, a common fingerprint of higher harmonics or a non-sinusodial shape in the current–phase relation. The main discovery of this section is the suppression of the first-order Shapiro steps at frequencies around 1 GHz, an intriguing observation that might point towards an underlying 4π-periodic contribution to the current–phase relation, which can in principle be caused by a parity-protected topological state or a high-transparency ballistic state that undergoes a Landau–Zener transition.

Conclusion

Novel appraches to the molecular beam epitaxy of core–shell nanowires in the group II telluride material system were explored in this work. Significant advances in growth spurred the development of a flexible and reliable platform for a charge transport characterization of the topological insulator HgTe in a tubular nanowire geometry. The transport results presented provide an important basis for the design of future studies that strive for the experimental realization of topological charge transport in the quantum wire limit.

Following up on preceding work on CdTe–HgTe core–shell nanowires, [14,45] several major advances were achieved in this thesis:

- The adaptation of a contactless low-temperature thermometry technique to nanowire growth, which proved to be crucial not only for the CdTe core but also for the subsequent developments (Chapter 2),
- the development of a novel selective area growth technique for the position controlled fabrication of ZnTe nanowire arrays as an alternative high-quality material system for the nanowire core (Chapter 3),
- the optimization of radial overgrowth with a CdTe buffer shell and the topological insulator HgTe (Chapter 4),
- and the exploration of charge transport through these nanowires with focus on the characterization of quantum interference effects and proximity induced superconductivity (Chapters 6 and 7).

Self-organized CdTe nanowires come with various challenges for application in charge transport, such as a pronounced tapering, a high density of twin plane defects, and a high area density that can obstruct the quality of growth for both nanowire core and shell. The narrow temperature window for long and straight CdTe nanowires of the order of 1 °C does not allow for an optimization within reasonable effort, and the self organized formation of the growth seeds makes it challenging to adjust the nanowire spacing. Hence, ZnTe was explored as an alternative material for the nanowire core. Further,

the focus was laid on the development of a selective area process, which allows for the full control over the position of each individual nanowire; a technique that is established for III-V semiconductor nanowires but has – with the exception of oxides [22] – not been reported for II-VI materials before. The key aspects of position controlled ZnTe nanowire growth were identified and resolved. This includes, amongst others, the choice of substrate, the surface preparation, and the formation of the growth seeds. A thorough investigation of the growth kinetics in dependence of the spacing between adjacent nanowires allowed to identify a competition limited growth regime for the typical small spacing during self-organized growth. For a larger spacing – readily accessible via the position controlled process – a diffusion limited regime was realized where adjacent nanowires do not compete for adatoms, which is beneficial for the homogeneity and reliability of growth. Precise control of the substrate temperature made it possible to adjust the axial growth rate, the cross-sectional shape, and the yield of vertical nanowires. The optimized nanowires are straight and free-standing with a large aspect ratio and a negligible degree of tapering. An excellent crystal quality is evidenced by a transmission electron microscopy study. This makes our ZnTe nanowire arrays the ideal basis for high-quality radial heterostructures.

CdTe is a common substrate for epitaxial HgTe thinfilms due to its similar lattice constant. The ZnTe nanowires were thus overgrown with a CdTe buffer shell that ensures a spatial separation between lattice mismatch induced defects in the vicinity of the ZnTe interface and the HgTe shell, where charge transport takes place. The efficient relaxation of stress in the nanowire geometry effected a substantial suppression of the dislocation density already at CdTe thicknesses of 30–40 nm. The subsequent HgTe overgrowth is strongly affected by the polarity of the surface facet. Non-polar as well as Hg-terminated facets have a relatively large growth window, whereas an essential influence of the substrate temperature was found for Te-terminated sides. This allows to adjust between different growth regimes: At low temperature the HgTe shell is faceted and has gaps on the Te-terminated sides; in a narrow window at intermediate temperature a step-flow regime leads to a faceted but closed trigonal shell; and at high temperature overgrowth is smooth and rounded. Overall, the HgTe shell has an excellent crystal quality and an epitaxial interface to the CdTe. Further, the geometric phase analysis of transmission electron micrographs revealed the presence of elastic strain in the HgTe lattice, which is known to open a bulk bandgap in three-dimensional HgTe that makes the intrinsic semimetal a topological insulator. [41, 80]

Both ZnTe and CdTe are wide-gap semiconductors and therefore insulating at cryogenic temperatures. Thus, the key properties of these samples related to charge transport lie in the peculiar intrinsic band structure of HgTe, a three-dimensional topological insulator, and the quantization effects that come with the reduced physical dimensions of the nanowires. In order to

probe these characteristics, this work focuses on magnetotransport to reveal the effect of quantum interference in the tubular HgTe shell, and the study of superconducting correlations induced by the proximity effect.

The observation of conductance fluctuations in magnetotransport indicates the presence of phase coherent electronic states in the HgTe shell. Further, the growth regime for core and shell was found to have considerable effect on the uniformity of the magnetoconductance signal. In particular, the optimized ZnTe-based nanowires with the HgTe shell grown in the step-flow regime show distinctly regular quantum oscillations with a magnetic flux periodicity of h/e. These are a clear fingerprint of the Aharonov–Bohm effect, which has a predominant influence in clean samples. [94] Hence, the preceding advances in growth led to the substantial improvement in the nanowire quality for magnetotransport, which opens up an avenue for a more detailed investigation of the Aharonov–Bohm effect in quasi-one-dimensional HgTe.

When contacted by superconducting Al-based electrodes, the CdTe–HgTe core–shell nanowires exhibit a sharp transition to an induced superconducting state at millikelvin temperature. Characteristic quantities such as the critical current, the excess current, and the superconducting gap were characterized. From these, a decent junction transparency of about 0.7 can be inferred, which is in line with the observation of a pronounced subgap structure due to Andreev reflection. Further, a Cooper pair coherence length was derived that is smaller but still of the order of the junction length of about 300 nm.

From two- and three-dimensional thinfilms it is known that HgTe possesses topologically protected surface states. Thus, one could expect them to be present also in the tubular nanowire geometry. But the question is, how – and to what extent – they affect charge transport over an eventual contribution of bulk bands. For this purpose, we study both magnetotransport and induced superconductivity in more detail. First, Aharonov–Bohm type magnetoconductance oscillations only give direct evidence of topological surface state transport if the Fermi energy can be gated through the Dirac point, which is unfortunately not possible for three-dimensional HgTe. Still, conclusions may potentially be drawn from the estimated radial profile of modes that can be inferred from the frequency distribution of magnetoconductance oscillations. So far, this analysis suggests an accumulation of modes close to the inner interface of the shell within an approximate radial extent of about 10 nm, which would neither contradict transport through a partly delocalized surface state, nor can exclude bulk-dominated transport. However, it indicates a suppression of charge transport towards the outer surface, which can be attributed to a reduced electron phase coherence length at the nanowire surface, likely due to lithography-induced damage and oxidization. And second, measurements of the induced superconductivity are predicted to possibly reveal a signature of the topological surface state band structure even on top of a substantial bulk contribution. [131] In this context, the temperature dependence of the

critical current is found to be described best both qualitatively and quantitatively by a basic model that assumes topological p-wave correlations of the Andreev bound state spectrum rather than a conventional s-wave pairing. Further, a remarkable behavior is observed in the microwave response of the superconducting junctions – the suppression of the first order Shapiro steps, which is a sign of a 4π-periodic current–phase relation that is usually realized in topological or ballistic junctions. [127,136] Together, these observations may be explained by topological superconductivity in the surface states on top of a bulk band contribution – although it is important to emphasize that so far a trivial origin can not be safely ruled out. In particular, for the interpretation of the transport results one has to bear in mind the complex tubular geometry of the system, which may have an intricate effect on the charge flow and thus make a definite statement challenging.

To conclude, the advances in nanowire growth allowed to create a versatile high-quality platform for the investigation of charge transport at the interplay between quantum size effects and the peculiar electronic states in HgTe core–shell nanowires. With fabrication well under control, we are now at the beginning of a comprehensive exploration of charge transport in this system and can look forward to upcoming results in future studies. From the current point of view the following approaches seem particularly worthwhile to pursue: First, a protective (Hg,Cd)Te cap could help to retain phase coherence close to the nanowire surface, where it appears suppressed in the current uncapped samples. Preliminary growth tests exhibit a high crystal quality and an epitaxial relation to the HgTe shell, which makes it promising for application. Second, it would be interesting to investigate the Aharonov–Bohm effect in thicker HgTe shells, where the analysis of the contributing oscillation frequencies can be expected to reveal a more notable distinction between modes that are localized at the surface and modes that extend over the entire bulk, which might eventually provide a tool to disentangle surface and bulk contributions in magnetotransport. Third, it would be important to reliably link the missing Shapiro steps to a 4π periodicity of the Andreev bound state spectrum. This can be done by the direct phase-dependent spectroscopy in a gate- and flux-tunable microwave resonator similar to that reported by M. Hays *et al.* [143] And fourth, induced superconductivity at larger magnetic fields might be experimentally accessible with a type-II superconductor as the contact material. This is of particular interest, because it allows to probe the influence of the flux periodic reappearing of the gapless Dirac subband on the properties of the induced supercurrent, which was not possible with the 10 mT-small critical field of Al. In particular, threading half a magnetic flux quantum through the nanowire, which resembles a magnetic flux density of about 0.1 T in a typical sample, is proposed to enable an odd number of surface state modes – a prerequisite for the realization of Majorana bound states [11] – irrespective of the exact location of the Fermi level. [10]

Zusammenfassung

Die vorliegende Arbeit befasst sich mit der Herstellung und Charakterisierung von Nanodraht-Heterostrukturen, die den Topologischen Isolator HgTe enthalten. Bedeutende Fortschritte bei der Probenherstellung ermöglichten die Entwicklung einer flexiblen und zuverlässigen Plattform für Ladungstransportuntersuchungen. Die Ergebnisse dieser Transportuntersuchung bieten eine wichtige Grundlage für die Planung zukünftiger Studien, die den experimentellen Nachweis von topologischem Ladungstransport in quasi-eindimensionalen HgTe-Nanostrukturen zum Ziel haben.

In einer vorangegangenen Arbeit wurden selbstorganisiert mittels VLS-MBE gewachsene CdTe-Nanodrähte als Basis für das radiale Überwachstum mit einer HgTe-Schale verwendet. [14] Die Kontrolle der Substrattemperatur ist dabei der entscheidende Parameter während des CdTe-Wachstums. Um die Qualität und Reproduzierbarkeit des Wachstumsprozesses zu verbessern, wurde ein auf Bandkantenspektroskopie basierendes Thermometrie-Verfahren implementiert und damit eine signifikante Verbesserung der Temperaturkontrolle erzielt. Allerdings zeigte sich, dass die CdTe-Nanodrähte aufgrund ihrer morphologischen Eigenschaften als Grundlage für Transportuntersuchungen nur bedingt geeignet sind. Deshalb wurde einerseits mit ZnTe ein alternatives, besser zu optimierendes Materialsystem herangezogen, und andererseits ein vorstrukturierter Wachstumsprozess angestrebt, der eine präzise Kontrolle von Position, Flächendichte und Durchmesser der Nanodrähte ermöglicht. Im Gegensatz zu III-V Halbleitern ist das vorstrukturierte Nanodrahtwachstum von II-VI Materialien – mit Ausnahme von Oxiden [22] – noch weitestgehend unerforscht. Daher erforderte die Prozessentwicklung von vorstrukturierten ZnTe-Nanodrähten das Identifizieren und Lösen einiger grundlegender Schlüsselaspekte, wozu unter anderem die Wahl des Substrates, die Oberflächenbehandlung, sowie die Präparation des Wachstumskatalysators zählen. Darüber hinaus wurde gezeigt, dass sich in Abhängigkeit von Nanodraht-Flächendichte und Substrattemperatur verschiedene Wachstumsregimes realisieren lassen: Im Gegensatz zu der vergleichsweise hohen Flächendichte des selbstorganisierten Wachstums ermöglicht der vorstrukturierte Ansatz beliebige Nanodrahtabstände. Dadurch konnte ein rein diffusionslimitiertes Wachstumsregime erzielt

werden, bei dem die Konkurrenz benachbarter Nanodrähte um Adatome keine Rolle mehr spielt, was sich positiv auf die Homogenität und Stabilität des Wachstums auswirkt. Die präzise Kontrolle der Substrattemperatur ermöglichte es, die Wachstumsrate, die Querschnittsgeometrie, sowie den Anteil vertikaler Nanodrähte zu optimieren. Die resultierenden Nanodrähte haben ein großes Aspektverhältnis und einen konstanten Durchmesser und zeichnen sich durch eine exzellente Kristallqualität aus, was sie zu einer idealen Grundlage für hochwertige radiale Heterostrukturen macht.

Die ZnTe-Nanodrähte wurden mit einer Pufferschicht aus CdTe überwachsen, einem zu HgTe nahezu gitterangepassten Material, um die defektreiche Grenzfläche zum ZnTe-Kern von der für den Ladungstransport relevanten HgTe-Schale räumlich zu trennen. Die für Nanostrukturen typische effiziente Relaxation von Gitterverspannung bewirkt bereits ab einer CdTe-Schichtdicke von 30–40 nm eine weitestgehende Reduktion der Defektdichte, was trotz der verhältnismäßig großen Gitterfehlanpassung zwischen ZnTe und CdTe für eine gute Kristallqualität an der Oberfläche sorgt. Über die Substrattemperatur und das Cd : Te-Materialflussverhältnis können die bevorzugten Wachstumsfacetten und damit die Morphologie der Oberfläche reguliert werden. Die Polarität der Wachstumsfacette hat einen wesentlichen Einfluss auf das anschließende Überwachstum mit HgTe. Im Gegensatz zu unpolaren oder Hg-terminierten Kristallfacetten weist das Überwachstum von Te-terminierten Oberflächen ein sehr enges Temperaturfenster auf. Dadurch konnten in Abhängigkeit der Substrattemperatur verschiedene Wachstumsregimes realisiert werden: Bei niedriger Temperatur zeigte sich eine starke Facettierung der HgTe-Schale mit Lücken auf den Te-terminierten Seiten; in einem schmalen Bereich mittlerer Temperatur wurde Stepflow-Wachstum mit einer facettierten aber geschlossenen Oberfläche beobachtet; und bei hoher Temperatur wurde ein homogenes, glattes Überwachstum erreicht. Mittels Transmissions-Elektronenmikroskopie wurde eine sehr hohe Kristallqualität sowie ein epitaktisches Verhältnis zum darunterliegenden CdTe nachgewiesen. Desweiteren zeigte eine geometrische Phasenanalyse das Vorhandensein von elastischer Verspannung im HgTe-Kristallgitter, welche in dreidimensionalen HgTe-Kristallen eine Bandlücke in den Volumenzuständen öffnet, die das intrinsische Halbmetall zu einem Topologischen Isolator macht. [41, 80]

Sowohl ZnTe als auch CdTe sind Halbleiter mit großer Bandlücke und verhalten sich daher isolierend bei tiefen Temperaturen. Deshalb liegen die zentralen für den Ladungstransport relevanten Eigenschaften in der speziellen elektronischen Bandstruktur von HgTe sowie in den Quantisierungseffekten aufgrund des geringen Nanodrahtumfangs. Um diese in Transportmessungen zu untersuchen, wurde der Schwerpunkt auf die Charakterisierung der Magnetfeldabhängigkeit, welche auf Quanteninterferenzeffekte rückschließen lässt, sowie die induzierte Supraleitung, die von den topologischen Eigenschaften der Bandstruktur beeinflusst wird, gesetzt.

Das Vorhandensein von Leitwertsfluktuationen in Magnetotransport-Messungen deutet auf phasenkohärenten Ladungstransport hin. Desweiteren zeigt das spezifische Wachstumsregime von Nanodrahtkern und -schale einen starken Einfluss auf die Regelmäßigkeit der Leitwertsfluktuationen. Insbesondere die optimierten ZnTe-basierten Nanodrähte, die im Stepflow-Regime mit einer HgTe-Schale überwachsen wurden, weisen sehr ausgeprägte regelmäßige Quantenoszillationen mit einer Fluss-Periodizität von h/e auf. Diese werden als Charakteristikum für den Aharonov–Bohm-Effekt angesehen, welcher in weitgehend defektfreien Proben auftritt. [94] Das lässt wiederum den Rückschluss auf eine deutliche Verbesserung der Nanodrahtqualität aufgrund der Entwicklungsfortschritte im Probenwachstum zu, was die Möglichkeit eröffnet in diesem System den Aharonov–Bohm-Effekt nun im Detail zu untersuchen.

Durch die Kontaktierung mit supraleitenden Elektroden konnte ein Suprastrom in den Nanodraht induziert werden, was sich in einem sprunghaften Phasenübergang in einen dissipationslosen Zustand bei Millikelvin-Temperaturen äußert. Verschiedene charakteristische Größen wurden bestimmt, darunter der kritische Strom I_c, der Überschuss-Strom I_x und die supraleitende Energielücke Δ. Aus diesen kann eine Kontakt-Transparenz von etwa 0.7 berechnet werden, was in Anbetracht der *ex situ* aufgebrachten Kontaktelektroden einen hohen Wert darstellt. Die verhältnismäßig gute Transparenz deckt sich mit der Beobachtung einer ausgeprägten Struktur des dynamischen Leitwerts dI/dV aufgrund von mehrfachen Andreev-Reflektionen. Desweiteren wurde die Cooperpaar-Kohärenzlänge als geringer, aber noch in der selben Größenordnung des Kontaktabstands von ca. 300 nm liegend abgeschätzt.

In zwei- und dreidimensionalen HgTe-Dünnschichtsystemen wurden topologisch geschützte Rand- bzw. Oberflächenzustände experimentell bereits nachgewiesen. [12,13] Daher kann man erwarten, dass sich diese auch entlang der inneren und äußeren Grenzfäche der quasi-eindimensionalen HgTe-Nanodrahtschale befinden. Allerdings ist fraglich, ob und auf welche Weise diese den Ladungstransport über einen eventuellen Beitrag des Volumenmaterials hinweg beeinflussen. Der Aharonov–Bohm-Effekt auf der einen Seite ermöglicht lediglich einen direkten Rückschluss auf topologischen Ladungstransport, wenn die Fermi-Energie in den Bereich des Dirac-Punktes gebracht werden kann, was in HgTe nicht möglich zu sein scheint. Alternativ könnten entsprechende Informationen eventuell auch aus der radialen Modenverteilung der Ladungszustände, welche zu dem beobachteten Magnetotransport-Signal beitragen, gezogen werden. Eine diesbezügliche Untersuchung deutet darauf hin, dass der überwiegende Beitrag von Moden stammt, die in der Nähe der inneren Grenzfläche mit einer radialen Ausdehnung von etwa 10 nm lokalisiert sind. Bei einer HgTe-Dicke von etwa 35 nm schließt dies allerdings weder einen etwas delokalisierten Oberflächenzustand noch Volumenzustände als Ursache aus. Hier könnte daher der Vergleich mit einer Nanodrahtprobe mit dickerer HgTe-Schale und damit einer klareren Trennung zwischen Vo-

lumen und Oberfläche einen möglichen Anhaltspunkt liefern. Desweiteren zeigt die Modenverteilung eine Unterdrückung von Ladungstransport im Bereich der äußeren Oberfläche des Nanodrahtes, beispielsweise aufgrund von Oxidation und oberflächennahen Schäden am Kristallgitter, die zu einer lokal reduzierten Phasenkohärenzlänge führen können. Dieser Einfluss ließe sich durch eine CdHgTe-Schutzschicht, die direkt im Anschluss an das HgTe-Überwachstum aufgebracht wird, verringern. Der induzierte Suprastrom auf der anderen Seite sollte auch dann einen klaren Einfluss der topologischen Bandstruktur der Oberflächenzustände zeigen, wenn ein beträchtlicher Anteil des Ladungstransports von Volumenzuständen getragen wird. [131] In diesem Zusammenhang ist hervorzuheben, dass zum einen die Temperaturabhängigkeit des kritischen Stroms von einem einfachen Modell unter Annahme einer topologischen p-Wellen-Korrelation sehr gut beschrieben wird, während zur normalen s-Wellen-Korrelation deutliche Abweichungen bestehen. Zum anderen zeigen Messungen an diesen Strukturen eine ungewöhnliche Reaktion auf die Anregung mit Mikrowellenstrahlung: Von den zu erwartenden Shapiro-Plateaus bei ganzzahligen Vielfachen von $V = hf/2e$ in der Spannungs–Strom-Kennlinie ist in einem gewissen Frequenzbereich das jeweils erste Plateau für positive und negative Spannung unterdrückt. Dies kann auf einen 4π-phasenperiodischen Beitrag zum Suprastrom hindeuten, [138] welcher am ehesten auf einen topologischen Zustand zurückzuführen wäre.

Zusammenfassend liefert diese Arbeit einen wichtigen Beitrag zur Realisierung und Charakterisierung von topologischen Nanodrähten, was einen möglichen Ansatzpunkt für die Erzeugung von Majorana-Fermionen in einem Festkörpersystem bietet. Durch eine Reihe von Entwicklungsfortschritten im Bereich des Nanodrahtwachstums wurden signifikante Verbesserungen sowohl in der Probenqualität als auch bei der Zuverlässigkeit und Reproduzierbarkeit des Herstellungsprozesses erzielt. Dies äußert sich insbesondere in den strukturellen Eigenschaften und darüber hinaus auch in der Ausprägung der magnetfeldinduzierten Quanteninterferenzeffekte. Weiterführende Transportuntersuchungen der magnetfeldabhängigen Leitwertoszillationen deuten auf einen multimodalen Ladungstransport in einem phasenkohärenten semi-diffusiven Regime hin. Eine Charakterisierung der induzierten Supraleitung scheint desweiteren einen ersten möglichen Hinweis auf den Beitrag der topologischen Oberflächenzustände zu liefern. Damit bietet diese Arbeit den idealen Ausgangspunkt für die künftige Untersuchung von Ladungstransport in quasi-eindimensionalen Nanostrukturen des topologischen Isolators Quecksilbertellurid.

Appendix

A Growth of self-organized CdTe–HgTe core–shell nanowires

In the following a detailed step-by-step description of the growth procedure for self-organized CdTe nanowires grown onto ZnTe stubs is given. This method is based on work reported by M. Kessel, [14] extended by the substrate thermometry based on band edge spectroscopy discussed in Section 2.1.

Preparation of the growth seeds

For the self-organized VLS growth, a thin layer of Au is thermally dewetted on top of a GaAs substrate. Solid-state diffusion of Ga into the Au results in the formation of eutectic Au–Ga droplets that are liquid at the CdTe growth temperature. However, for reliably working band edge thermometry the droplet formation must be prevented on a part of the substrate. This can be conveniently achieved with a shadow mask during the Au deposition.

Preparation of self-organized Au–Ga droplets

- Mount a Si-doped 2" (111)B GaAs wafer on a substrate holder with In.
- Load sample into the MBE cluster, degas for 10 min at 300 °C.
- Transfer to III-V MBE chamber, increase T_{TC} to 640 °C with +50 K/min until RHEED indicates that the oxide layer is fully removed, then switch off substrate heater.
- Transfer to metal evaporation chamber, deposit 1.0 nm of Au with a rate of 0.01–0.02 nm/s.

CdTe nanowire growth

Precise control of the substrate temperature is most crucial for the CdTe growth. In order to achieve reliable results T_{BE} should be held constant within about ±0.25 °C. Even small deviations in the calibration of the band edge thermometry system – e.g., due to a different substrate doping level of a new batch of wafers – can already impact the growth result. Thus, the required absolute temperatures likely differ from the values given here, but relative changes should remain the same. Measuring T_{BE} at the onset of nanowire growth determined from the appearance of nanowire-specific facets in the RHEED diffraction pattern is therefore a very precise method to calibrate the required offset for the band edge thermometry system.

CdTe nanowires grown onto ZnTe stubs

- Transfer to II-VI MBE chamber, increase T_{TC} to 450 °C with +50 K/min, stay at $\sim$ 450 °C for 10 min.
- Adjust band edge system, reduce T_{BE} to 440 °C, stabilize for $\sim$ 10 min.
- Supply Zn flux at $\sim 1.0 \times 10^{-6}$ torr, wait 60 s, add Te flux at $\sim 1.3 \times 10^{-6}$ torr (Zn : Te ratio of $\sim$ 0.8).
- After 120 s, replace Zn with Cd flux at $\sim 1.6 \times 10^{-6}$ torr (Cd : Te ratio of $\sim$ 1.2), wait 60 s, reduce T_{BE} to 374.0 °C slow enough to avoid undershoot below 373.5 °C.
- As soon as $T_{\mathrm{BE}} = 374.0$ °C is reached, start to increase T_{TC} in steps of 0.2 °C. Adapt the rate of temperature increasing in order to keep T_{BE} stable throughout the next $\sim$ 3 h, after that T_{TC} should be mostly stable for a constant value of T_{TC}.
- Once in a while confirm straight and kink-free nanowire growth in RHEED with reduced beam current.
- After 6–8 h CdTe growth, stop growth by closing the Te shutter and cool to $T_{\mathrm{BE}} \sim 240$ °C in Cd flux.

HgTe shell growth

The substrate temperature during HgTe overgrowth of the CdTe nanowires can be controlled by band edge thermometry only in a very limited way. Due to the small band gap of HgTe the band edge signal can only be used to determine the initial offset between T_{TC} and the substrate temperature before growth. Thus, the total preceding exposure time to Te must be considered when controlling the growth temperature in this step. When the sample has been exposed to Te for more than $\sim$ 3 h, T_{TC} should be kept constant throughout growth. If it has been re-glued onto a new sample holder (i.e., a "reset" of the Te exposure) it is advisable to increase T_{TC} with a temperature ramp of +0.1 °C during HgTe growth.

HgTe radial overgrowth

- Transfer to the Hg containing MBE chamber, increase T_{TC} to 200 °C with +50 K/min.
- Adjust band edge thermometry system, stabilize for 10 min at 177.5 °C (or as desired).
- Adjust the Hg flux to $\sim 3.5 \times 10^{-4}$ torr (Hg : Te ratio of 230), stabilize T_{BE} for additional 10 min, then add Te flux at $\sim 1.5 \times 10^{-6}$ torr.
- Keep the substrate temperature constant for 30 min (or as needed), stop growth by closing the Te shutter and cool to $T_{\mathrm{TC}} \sim 100$ °C in Hg flux, unload sample after chamber was cleared from Hg for $\sim$ 20 min.

B Growth of ZnTe–CdTe/HgTe core–shell nanowire arrays

The following provides a detailed step-by-step description of the final growth procedure for the position-controlled growth of ZnTe nanowire arrays that was developed in this thesis.

MBE growth of virtual ZnTe substrates

Virtual substrates are thick relaxed buffer layers grown onto a wafer of a different material. In this work, mostly ZnTe buffer layers grown on Si-doped (111)B GaAs wafers are used as virtual substrate for the position-controlled growth of ZnTe nanowire arrays. Other virtual substrates can be fabricated in a similar way. It should be noted that this process has not been optimized nor in detail characterized with respect to the crystal quality of the epilayer, because – contrary to thinfilm growth – the small footprint of the nanowires requires a good substrate crystal quality only on a local scale.

ZnTe buffer growth

- Mount a Si-doped 2" (111)B GaAs wafer onto a clamped substrate holder, deoxidize with 60 s ion milling (3.5 sccm Ar; beam 8 mA, 1.0 kV; extractor −0.2 kV).
- Load promptly into the UHV cluster, degas for 10 min at 300 °C.
- Transfer to widegap II-VI MBE chamber, adjust substrate PID values for clamped holders (P: 16, I: 70, D: 12), heat until RHEED indicates the desorption of amorphous residues from the ion milling.
- Stabilize temperature at $T_{\mathrm{BE}} = 330\,^{\circ}\mathrm{C}$, add about $0.8\text{–}1.0 \times 10^{-6}$ torr Zn and $1.2\text{–}1.4 \times 10^{-6}$ torr Te flux (Zn : Te ratio of 0.6–0.8).
- Keep T_{BE} constant for about 1.5 h, stop growth by closing the Te shutter and cool to $T_{\mathrm{BE}} \sim 300\,^{\circ}\mathrm{C}$ in Zn flux.
- Restore previous substrate PID settings for regular substrate holders (P: 100, I: 150, D: 2), bring chamber to standby mode.

Ex situ preparation of the Au disk array

The position-controlled growth method requires several steps of sample preparation, in particular the lithographic patterning of the growth seeds and a subsequent surface cleaning.

Au disk lithography

- Cut a piece of (virtual) substrate, clean with ultrasound (US) in acetone (ACT), rinse with isopropyl alcohol (IPA), blow-dry with N_2.
- Spin-coat sample with a two-layer PMMA resist: *Allresist* AR–P 639.04 (50k 4%) at 3900 rpm and AR–P 649.04 diluted 1 : 1 with ethyllactate (200k 2%) at 5400 rpm; 10 min bakeout at 200 °C after each layer.
- Electron beam dot exposure at 30 kV acceleration voltage, 30 µm aperture and 0.036 µC dot dose, using a $(204.8\,\mu m)^2$ writefield size.
- Develop for 45 s in IPA with 80 kHz US applied, rinse in ultrapure water (UPW), blow-dry thoroughly with N_2.
- 45 s ion milling (1.62 sccm Ar; beam 1.0 kV; extractor −1.0 kV; ion current 10 mA [lower display]), then deposit 27 nm Au without breaking the vacuum.
- Lift–off for ∼ 1 h in ACT at 50 °C, rinse with IPA, blow-dry with N_2.

Surface cleaning

- Basic cleaning after cutting a piece of Au disk array: ACT with short application of 80 kHz US at 50% power, rinse in IPA, blow-dry with N_2.
- Ash organic residues in O_2 plasma for 3 min (flow 5, power 1.2).
- Prepare sample holder with Ga or In glue, prepare HCl dip from 24 ml UPW and 8 ml HCl and vent loadlock of the UHV cluster.
- Etch 1/6 2" Si-doped (111)B GaAs for 90 s in HCl, rinse for 60 s in UPW. Simultaneously etch the pre-patterned substrate for 35 s and rinse for 60 s in UPW. Blow-dry both samples thoroughly with N_2.
- Mount both samples on the sample holder and load promptly into the UHV cluster, degas for 20 min at 200 °C.

In situ preparation of the growth seeds

Gallium is added to the Au disks from an effusion cell in order to achieve a liquid growth seed at the growth temperature.

Supply of Ga

- Transfer to III-V MBE chamber, increase T_{TC} to 200 °C with +50 K/min, and to 250 °C with +20 K/min.
- Stabilize substrate temperature at 250 °C for about 6 min, then repeat 6× the sequence of 20 s Ga supply followed by 120 s delay.

ZnTe nanowire growth

Precise control of the substrate temperature is important for the ZnTe growth, because it influences not only the axial growth rate but also the cross-sectional

shape and the vertical yield. Thus, it is important to confirm prior to growth that the band edge thermometry system is aligned and calibrated accordingly.

ZnTe VLS growth

- Transfer to II-VI MBE chamber, increase T_{TC} to 250 °C with +50 K/min, at 250 °C open supply of Zn flux at ~ 0.8–1.0×10^{-6} torr.
- Increase T_{TC} further to 440 °C with +20 K/min, adjust the band edge thermometry system and start temperature measurement.
- Adjust the substrate temperature to $T_{\mathrm{BE}} = 442$ °C (or as needed), stabilize for 12 min, then add Te flux at ~ 1.0–1.3×10^{-6} torr (Zn : Te ratio of ~ 0.8).
- Keep T_{BE} constant for 4 h (or as needed), stop growth by closing the Zn shutter and cool to $T_{\mathrm{TC}} \sim 300$ °C in Te flux.

CdTe shell growth

The CdTe shell can be grown onto the ZnTe nanowires either still directly in the wide-gap II-VI chamber (typically done), or after the transfer to the Hg-containing chamber. During overgrowth with CdTe the band edge signal begins to degrade at some point, which can falsely suggest a temperature drift. Thus it is important to consider whether a drift in T_{BE} is a real change in the substrate temperature which has to be counteracted, or if it is due to the degrading signal. With ZnTe nanowires grown for more than ~ 3 h it is typically safe to control the substrate temperature via T_{BE} for about 15 min and then continue to grow at a constant value of T_{TC}.

CdTe radial overgrowth

- Increase T_{TC} to 280 °C with +50 K/min, at 280 °C open supply of Te flux at ~ 1.0–1.3×10^{-6} torr.
- Increase T_{TC} further to 330 °C with +20 K/min, adjust the band edge thermometry system and start the measurement.
- Adjust the substrate temperature to $T_{\mathrm{BE}} = 315$ °C, stabilize for 2 min, then add Cd flux at ~ 2.0–2.6×10^{-6} torr (Cd : Te ratio of ~ 2).
- Keep substrate temperature constant for 45 min (or as needed), stop growth by closing the Te shutter and cool to $T_{\mathrm{TC}} \sim 240$ °C in Cd flux.

HgTe shell growth

HgTe overgrowth is achieved as described in the Appendix A for the self-organized CdTe nanowires. The process is still the same if already the CdTe shell was grown in the Hg-containing chamber, with the only difference that the starting point at $T_{\mathrm{TC}} = 200$ °C is approached from higher temperature. This might take a bit longer to reach as the cooldown rate is typically slower than the temperature ramp during warmup, but is usually quicker to stabilize.

C Lithograpy for the integration into electronic circuits

In the following we summarize the detailed lithography process for the fabrication of electrical contacts to the nanowires. Evaporated and sputtered contact materials require different processing, which is indicated at the corresponding positions.

Preparation of the coordinate system

For contacting, the nanowires are moved from the as-grown ensemble to a new substrate, typically by mechanical stamp transfer. A precise determination of the position of the dropcasted nanowires requires a pre-defined coordinate system on the lithography substrate. Instead of mechanical transfer, dielectrophoresis can be used with a nanowire suspension in order to localize and align the nanowires at an electrode as discussed in Ref. [14]. In this case, the electrode is patterned together with the coordinate system.

Preparation of the coordinate system

- Cut a degenerately doped Si substrate to the desired size ($1 \times 1\,\mathrm{cm}^2$ is suitable for the simultaneous fabrication of nine transport devices). Clean with US in ACT, rinse with IPA, blow-dry with N_2.
- Spin-coat sample with a two-layer PMMA resist: *Allresist* AR–P 669.06 (600k 6%) at 6000 rpm and AR–P 679.03 (950k 3%) at 6000 rpm; 10 min bakeout at 80 °C after each layer.
- Electron beam exposure at 30 kV acceleration voltage, 20 µm aperture and $500\,\mu\mathrm{C/cm}^2$ area dose, using a $(204.8\,\mu\mathrm{m})^2$ writefield size. The optional dielectrophoresis electrode is patterned with 60 µm aperture and $380\,\mu\mathrm{C/cm}^2$ area dose, using a $(819.2\,\mu\mathrm{m})^2$ writefield aligned to the previous one.
- Develop for 80 s in a 1 : 1 mixture of *Allresist* AR 600–56 and IPA followed by 70 s in IPA with each 3 s of 80 kHz US applied, rinse in UPW, blow-dry thoroughly with N_2.
- 20 s ion milling (1.62 sccm Ar; beam 1.0 kV; extractor −1.0 kV; ion current 10 mA [lower display]), followed by deposition of 5 nm Ti and 20 nm Au.
- Lift–off for ~ 1 h in ACT at 50 °C, rinse with IPA, blow-dry with N_2.

Transfer of the nanowires

Different transfer techniques can be used depending on the purpose of the transport device and the areal density of the as-grown nanowire ensemble. The mechanical transfer by stamping on the one hand is quick and flexible, but comes with limited control over position, density and orientation of the dropcasted nanowires. Dropcasting a nanowire suspension onto an electrode

with an applied AC voltage on the other hand allows to localize and align nanowires to the electrode with the effect of dielectrophoresis. However, this techique is significantly less efficient with respect to the amount of transferred nanowires from a respective piece of the as-grown ensemble, and is thus less feasible for the position controlled nanowire arrays with an about two orders of magnitude lower areal density compared to self-organized growth, thus we describe here only the mechanical transfer. For instructions on dielectrophoresis please refer to Refs. [14,45].

Mechanical stamp transfer

- Cut a piece of the desired as-grown nanowire ensemble with a size of about $2 \times 2\,\mathrm{mm}^2$, clean by blowing with N_2.
- Place the sample upside down on the lithography substrate at the approximate position of the first coordinate system and tap gently on the backside, e.g., with tweezers in order to break off the nanowires. Tapping under an angle of 45° to the surface gives the transferred nanowires to some extent a preferential orientation on the substrate.
- Check the result under an optical microscope and repeat if necessary, else proceed with the next coordinate system.

Contact electrode lithography

Contrary to the evaporated contact materials that are discussed in this thesis, sputtered Nb and MoRe as type-II superconductors could provide an interesting alternative for experiments involving induced superconductivity. However, they seem to apply a significant amount of strain on the sample, especially large structures such as bondpads (cf. Ref. [45]). This can be mitigated to some extent with a two-step process for inner and outer part of the contacts, which is not necessary for evaporated contacts.

Evaporated contacts

- Spin-coat sample with a two-layer PMMA resist: *Allresist* AR–P 669.06 (600k 6%) at 6000 rpm and AR–P 679.03 (950k 3%) at 6000 rpm; 10 min bakeout at 80 °C after each layer.
- Take optical images at 50x magnification and design the contacts for the selected nanowires.
- Electron beam exposure of the inner contact area at 30 kV acceleration voltage, 20 µm aperture and $500\,\mu\mathrm{C/cm}^2$ area dose, using a $(204.8\,\mu\mathrm{m})^2$ writefield size. The outer area is patterned with 60 µm aperture and $380\,\mu\mathrm{C/cm}^2$ area dose, using a $(819.2\,\mu\mathrm{m})^2$ writefield aligned to the previous one.
- Store the sample overnight in N_2 atmosphere in order to stabilize the resist (proved to be very important!).
- Develop for 80 s in a 1 : 1 mixture of *Allresist* AR 600–56 and IPA followed

by 70 s in IPA with each 3 s of 80 kHz US applied, rinse in UPW, blow-dry thoroughly with N_2.

- 8 s ion milling (1.62 sccm Ar; beam 1.0 kV; extractor −1.0 kV; ion current 10 mA [lower display]), followed by the deposition of the desired materials, e.g., Ti contacts (290 nm Ti and 30 nm Au) or Al contacts (5 nm Ti, 280 nm Al, 5 nm Ti and 30 nm Au).
- Lift–off for ∼ 1 h in ACT at 50 °C, rinse with IPA, blow-dry with N_2.

Alternative: sputtered contacts

- Spin-coat sample with a two-layer PMMA resist: *Allresist* AR–P 669.04 (600k 4%) at 4000 rpm and AR–P 679.02 (950k 2%) at 4000 rpm; 10 min bakeout at 80 °C after each layer.
- Take optical images at 50x magnification and design the contacts for the selected nanowires; use a separate layer for the very inner part of the contact.
- Electron beam exposure of the inner contact area at 30 kV acceleration voltage, 20 µm aperture and 500 $\mu C/cm^2$ area dose, using a $(204.8\,\mu m)^2$ writefield size.
- Store the sample overnight in N_2 atmosphere in order to stabilize the resist (important!).
- Develop for 45 s in IPA with applied US, rinse in UPW, blow-dry thoroughly with N_2.
- 8 s ion milling (1.62 sccm Ar; beam 1.0 kV; extractor −1.0 kV; ion current 10 mA [lower display]), followed by the deposition of the desired contact material, e.g., Nb contacts (5 nm Ti and 150 nm sputtered Nb).
- Lift–off for ∼ 1 h in ACT at 50 °C, rinse with IPA, blow-dry with N_2.
- Spin-coat sample with a two-layer PMMA resist: *Allresist* AR–P 669.06 (600k 6%) at 6000 rpm and AR–P 679.03 (950k 3%) at 6000 rpm; 10 min bakeout at 80 °C after each layer.
- Electron beam exposure of the outer contact area at 60 µm aperture and 380 $\mu C/cm^2$ area dose, using a $(819.2\,\mu m)^2$ writefield and the second set of contact markers.
- Store the sample overnight in N_2 atmosphere in order to stabilize the resist (important!).
- Develop for 80 s in a 1 : 1 mixture of *Allresist* AR 600–56 and IPA followed by 70 s in IPA with each 3 s of 80 kHz US applied, rinse in UPW, blow-dry thoroughly with N_2.
- 20 s ion milling (1.62 sccm Ar; beam 1.0 kV; extractor −1.0 kV; ion current 10 mA [lower display]), followed by the deposition of the outer contacts (50 nm Ti and 50 nm Au).
- Lift–off for ∼ 1 h in ACT at 50 °C, rinse with IPA, blow-dry with N_2.

Top gate lithography

The top gate provides a significantly larger gate efficiency and a higher stability compared to the integral back gate, as well as protection from environmental influence.

Top gate

- Spin-coat sample with a two-layer PMMA resist: *Allresist* AR–P 669.06 (600k 6%) at 6000 rpm and AR–P 679.03 (950k 3%) at 6000 rpm; 10 min bakeout at 80 °C after each layer.
- Design the top gate electrodes for the previously contacted nanowires.
- Electron beam exposure with 60 µm aperture and 380 $\mu C/cm^2$ area dose, using a $(819.2\,\mu m)^2$ writefield and the second set of contact markers.
- Store the sample overnight in N_2 atmosphere for resist stabilization.
- Develop for 80 s in a 1 : 1 mixture of *Allresist* AR 600–56 and IPA followed by 70 s in IPA with each 3 s of 80 kHz US applied, rinse in UPW, blow-dry thoroughly with N_2.
- 3 s reactive oxygen ion etching (program *miniclean*), followed by atomic layer deposition of 120 cycles HfO_2, and the gate electrode of 200 nm Ti at $(0, \pm 10)^\circ$ and 50 nm Au.
- Cleave wafer into individual $\sim (3\,mm)^2$ sample pieces.
- Lift–off for $\sim$ 1 h in ACT at 50 °C, rinse with IPA, blow-dry with N_2.

D Supplementary data

Strain at the CdTe–HgTe interface

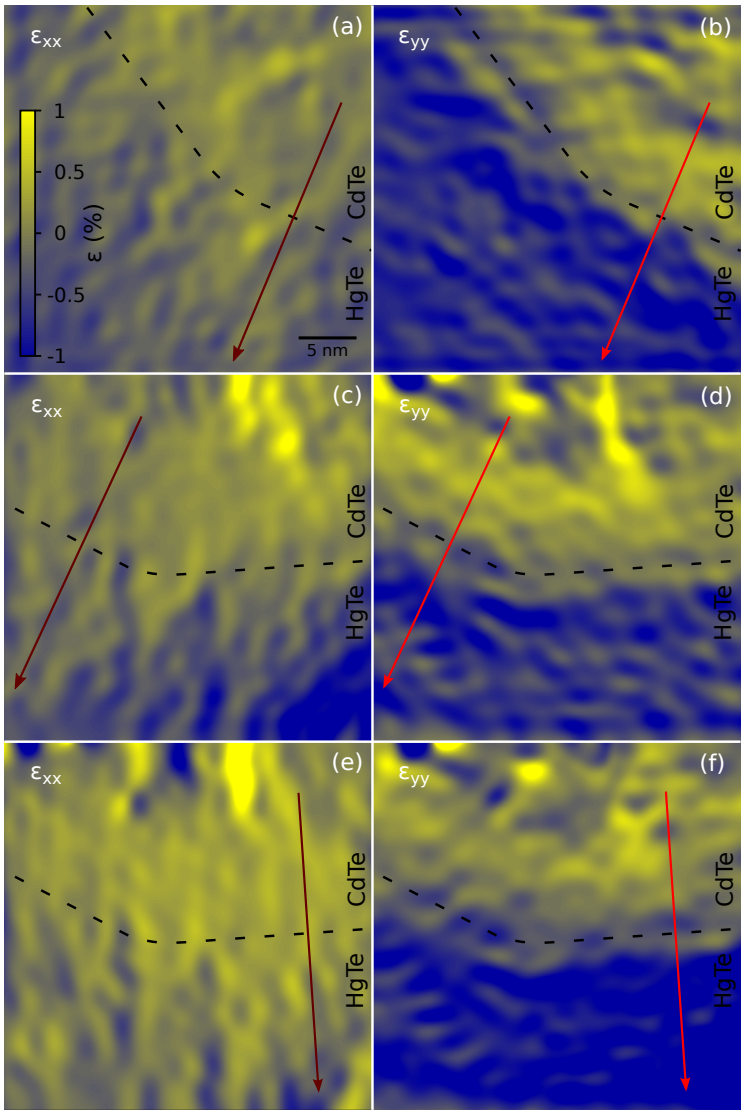

Figure D.1: Strain tensor maps for the components ε_{xx} (left-hand column) and ε_{yy} (right-hand column) perpendicular and parallel to the crystal direction indicated by the arrow, respectively, obtained by GPA of HAADF STEM lattice images. The approximate position of the CdTe–HgTe interface indicated by the dashed line is also inferred from the respective STEM image. (a) and (b) are based on the same micrograph as Fig. 4.10, whereas (c)–(f) show the result from a different nanowire.

Figure D.1 shows color coded maps of the strain tensor obtained from a geometrical phase analysis of scan distortion and stage drift corrected HAADF STEM images of the atomic lattice at the core–shell interface of a CdTe–HgTe nanowire as an addition to the data shown in Fig. 4.10. In all cases, the in-plane component ε_{xx} of the strain tensor indicates an approximately constant lattice parameter across the respective interface [along the arrow in Figs. D.1(a),(c),(e)], whereas the out-of-plane component ε_{yy} shows a clear step [cf. Figs. D.1(b),(d),(f)]. This indicates the presence of a significant amount of elastic strain at the CdTe–HgTe interface.

List of transport device parameters

Table D.1 lists the transport parameters inferred from VI characteristics for the different nanowire SNS junctions discussed in this thesis.

	full sample name	I_c (nA)	I_r (nA)	I_x (nA)	R_n (kΩ)	I_cR_n (μV)
SC-1	QW36-S09-M6, wire b	67	12	131	1.014	68
SC-2	QW36-S09-M6, wire a	53	10	118	0.993	53
SC-3	QW36-S09-M5, wire a	(15)*	15	111	0.773	(12)*
SC-4	QW89-S33-M5, wire a	53	38	129	0.514	27

Table D.1: Transport parameters of nanowire junctions with superconducting electrodes. The junction SC-3 was measured in a noise-limited setup, thus the values indicated by a star * are likely suppressed by a significant amount and thus need to be considered as unreliable.

List of publications

- M. Kessel, **J. Hajer**, G. Karczewski, C. Schumacher, C. Brüne, H. Buhmann, and L. W. Molenkamp, "CdTe–HgTe core–shell nanowire growth controlled by RHEED," *Physical Review Materials* **1**, 023401 (2017).

- **J. Hajer**, M. Kessel, C. Brüne, M. P. Stehno, H. Buhmann, and L. W. Molenkamp, "Proximity induced superconductivity in CdTe–HgTe core–shell nanowires," *Nano Letters* **19**, 4078–4082 (2019).

- R. Schlereth, **J. Hajer**, L. Fürst, S. Schreyeck, C. Brüne, H. Buhmann, and L. W. Molenkamp, "Band edge thermometry for the MBE growth of (Hg,Cd)Te–based materials," *Journal of Crystal Growth* **537**, 125602 (2020).

- **J. Hajer**, W. Mantei, M. Kessel, C. Brüne, S. Wenner, A. T. J. van Helvoort, H. Buhmann, and L. W. Molenkamp, "Selective area grown ZnTe nanowires as the basis for quasi-one-dimensional CdTe–HgTe multishell heterostructures," *Physical Review Materials* **4**, 066001 (2020).

Bibliography

[1] R. P. Feynman, "There's plenty of room at the bottom", *California Institute of Technology, Engineering and Science magazine* (1960). → p. 5.

[2] W. P. McCray, "MBE deserves a place in the history books", *Nature Nanotechnology* **2**, 5, p. 259 (2007). → p. 5.

[3] M. Feldman, editor, "Nanolithography: The Art of Fabricating Nanoelectronic and Nanophotonic Devices and Systems", Woodhead publishing, 2014. → p. 5.

[4] C. W. Shong, C. H. Sow, and A. T. S. Wee, "Science at the nanoscale: an introductory textbook", Pan Stanford Publishing, 2010. → p. 5.

[5] Nobel Media AB, "Press release: The Nobel Prize in Physics 2016", Accessed: 2020-04-19. → p. 5.

[6] S. M. Bhattacharjee, M. Mj, and A. Bandyopadhyay, "Topology and Condensed Matter Physics", volume 19, Springer, 2017. → p. 5.

[7] J. E. Moore, "The birth of topological insulators", *Nature* **464**, 7286, p. 194 (2010). → p. 5.

[8] M. Z. Hasan and C. L. Kane, "Colloquium: topological insulators", *Reviews of Modern Physics* **82**, 4, p. 3045 (2010). → p. 5.

[9] R. Egger, A. Zazunov, and A. L. Yeyati, "Helical Luttinger liquid in topological insulator nanowires", *Physical Review Letters* **105**, 13, p. 136403 (2010). → p. 6.

[10] A. Cook and M. Franz, "Majorana fermions in a topological-insulator nanowire proximity-coupled to an s-wave superconductor", *Physical Review B* **84**, 20, p. 201105 (2011). → pp. 6 and 130.

[11] J. Alicea, "New directions in the pursuit of Majorana fermions in solid state systems", *Reports on Progress in Physics* **75**, 7, p. 076501 (2012). → pp. 6, 103, and 130.

[12] C. Brüne, C. X. Liu, E. G. Novik, E. M. Hankiewicz, H. Buhmann, Y. L. Chen, X. L. Qi, Z. X. Shen, S. C. Zhang, and L. W. Molenkamp, "Quantum Hall effect from the topological surface states of strained bulk HgTe", *Physical Review Letters* **106**, 12, p. 126803 (2011). → pp. 6, 18, 54, 69, 76, and 133.

[13] M. König, S. Wiedmann, C. Brüne, A. Roth, H. Buhmann, L. W. Molenkamp, X.-L. Qi, and S.-C. Zhang, "Quantum spin Hall insulator state in HgTe quantum wells", *Science* **318**, 5851, p. 766 (2007). → pp. 6 and 133.

[14] M. Kessel, "HgTe shells on CdTe nanowires: A low-dimensional topological insulator from crystal growth to quantum transport", PhD thesis, Universität Würzburg, 2016. → pp. 6, 18, 19, 21, 22, 31, 33, 56, 61, 63, 81, 83, 89, 105, 127, 131, 136, 141, and 142.

[15] R. S. Wagner and W. C. Ellis, "Vapor-liquid-solid mechanism of single crystal growth", *Applied Physics Letters* **4**, 5, p. 89 (1964). → pp. 6 and 12.

[16] R. Haakenaasen, E. Selvig, S. Foss, L. Trosdahl-Iversen, and J. Taftø, "Segmented nanowires of HgTe and Te grown by molecular beam epitaxy", *Applied Physics Letters* **92**, 13, p. 133108 (2008). → pp. 6 and 18.

[17] M. Kessel, L. Lunczer, N. Tarakina, C. Schumacher, H. Buhmann, and L. W. Molenkamp, "Residual strain in free-standing CdTe nanowires overgrown with HgTe", *Applied Physics Letters* **114**, 15, p. 153104 (2019). → pp. 6, 19, 21, 33, 65, 67, and 68.

[18] L. Liu and W. Leung, "Transport property of zero-gap semiconductors under tensile stress", *Physical Review B* **12**, 6, p. 2336 (1975). → p. 6.

[19] M. Kessel, J. Hajer, G. Karczewski, C. Schumacher, C. Brüne, H. Buhmann, and L. W. Molenkamp, "CdTe-HgTe core-shell nanowire growth controlled by RHEED", *Physical Review Materials* **1**, p. 023401 (2017), . → pp. 6, 11, 18, 19, 21, 25, 28, 30, 33, 56, 61, and 147.

[20] M. A. Herman and H. Sitter, "Molecular Beam Epitaxy: Fundamentals and Current Status", volume 7 of *Springer Series in Materials Science*, Springer-Verlag, Berlin Heidelberg, 1996. → pp. 7 and 12.

[21] M. Henini, "Molecular beam epitaxy: from research to mass production", Newnes, 2012. → pp. 7 and 12.

[22] V. Consonni, E. Sarigiannidou, E. Appert, A. Bocheux, S. Guillemin, F. Donatini, I.-C. Robin, J. Kioseoglou, and F. Robaut, "Selective area growth of well-ordered ZnO nanowire arrays with controllable polarity", *ACS Nano* **8**, 5, p. 4761 (2014). → pp. 7, 128, and 131.

[23] P. Leubner, "Strain-engineering of the Topological Insulator HgTe", PhD thesis, Julius-Maximilians-Universität Würzburg, 2017. → pp. 12 and 18.

[24] C. Ames, "Molecular Beam Epitaxy of 2D and 3D HgTe, a Topological Insulator", PhD thesis, Julius-Maximilians-Universität Würzburg, 2015. → p. 12.

[25] T. Hamano, H. Hirayama, and Y. Aoyagi, "New technique for fabrication of two-dimensional photonic bandgap crystals by selective epitaxy", *Japanese Journal of Applied Physics* **36**, 3A, p. L286 (1997). → p. 12.

[26] P. J. Poole, J. Lefebvre, and J. Fraser, "Spatially controlled, nanoparticle-free growth of InP nanowires", *Applied Physics Letters* **83**, 10, p. 2055 (2003). → p. 12.

[27] A. I. Persson, M. W. Larsson, S. Stenström, B. J. Ohlsson, L. Samuelson, and L. R. Wallenberg, "Solid-phase diffusion mechanism for GaAs nanowire growth", *Nature Materials* **3**, 10, p. 677 (2004). → p. 12.

[28] K. A. Dick, K. Deppert, T. Mårtensson, B. Mandl, L. Samuelson, and W. Seifert, "Failure of the vapor–liquid–solid mechanism in Au-assisted MOVPE growth of InAs nanowires", *Nano Letters* **5**, 4, p. 761 (2005). → p. 12.

[29] F. Glas, J.-C. Harmand, and G. Patriarche, "Why does wurtzite form in nanowires of III-V zinc blende semiconductors?", *Physical Review Letters* **99**, 14, p. 146101 (2007). → p. 13.

[30] V. G. Dubrovskii and A. D. Bol'shakov, "Surface energy and modes of catalytic growth of semiconductor nanowhiskers", *Technical Physics Letters* **38**, 4, p. 311 (2012). → p. 13.

[31] V. G. Dubrovskii, "Nucleation theory and growth of nanostructures", Springer, 2014. → pp. 14, 15, 17, 33, 46, and 64.

[32] F. Glas, "Critical dimensions for the plastic relaxation of strained axial heterostructures in free-standing nanowires", *Physical Review B* **74**, 12, p. 121302 (2006). → pp. 14 and 35.

[33] G. E. Cirlin, V. G. Dubrovskii, I. P. Soshnikov, N. V. Sibirev, Y. B. Samsonenko, A. D. Bouravleuv, J. C. Harmand, and F. Glas, "Critical diameters and temperature domains for MBE growth of III–V nanowires on lattice mismatched substrates", *Physica Status Solidi - Rapid Research Letters* **3**, 4, p. 112 (2009). → p. 15.

[34] L. C. Chuang, M. Moewe, C. Chase, N. P. Kobayashi, C. Chang-Hasnain, and S. Crankshaw, "Critical diameter for III-V nanowires grown on lattice-mismatched substrates", *Applied Physics Letters* **90**, 4, p. 043115 (2007). → p. 15.

[35] S. A. Dayeh, W. Tang, F. Boioli, K. L. Kavanagh, H. Zheng, J. Wang, N. H. Mack, G. Swadener, J. Y. Huang, L. Miglio, K.-N. Tu, and S. T. Picraux, "Direct measurement of coherency limits for strain relaxation in heteroepitaxial core/shell nanowires", *Nano Letters* **13**, 5, p. 1869 (2013). → p. 16.

[36] S. A. Fortuna and X. Li, "Metal-catalyzed semiconductor nanowires: a review on the control of growth directions", *Semiconductor Science and Technology* **25**, 2, p. 024005 (2010). → pp. 18, 19, and 34.

[37] R. J. Koestner and H. F. Schaake, "Kinetics of molecular-beam epitaxial HgCdTe growth", *Journal of Vacuum Science & Technology A* **6**, 4, p. 2834 (1988). → pp. 18 and 61.

[38] E. Selvig, S. Hadzialic, T. Skauli, H. Steen, V. Hansen, L. Trosdahl-Iversen, A. D. van Rheenen, T. Lorentzen, and R. Haakenaasen, "Growth of HgTe nanowires", *Physica Scripta* **2006**, T126, p. 115 (2006). → p. 18.

[39] C. Thomas, X. Baudry, J.-P. Barnes, M. Veillerot, P.-H. Jouneau, S. Pouget, O. Crauste, T. Meunier, L. P. Lévy, and P. Ballet, "MBE growth and interfaces characterizations of strained HgTe/CdTe topological insulators", *Journal of Crystal Growth* **425**, p. 195 (2015). → p. 18.

[40] P. Ballet, C. Thomas, X. Baudry, C. Bouvier, O. Crauste, T. Meunier, G. Badano, M. Veillerot, J. P. Barnes, P. H. Jouneau, and L. P. Levy, "MBE growth of strained HgTe/CdTe topological insulator structures", *Journal of Electronic Materials* **43**, 8, p. 2955 (2014). → p. 18.

[41] H. Zhao, X. Chen, J. Lu, H. Shu, and W. Lu, "Band gap tuning in HgTe through uniaxial strains", *Solid State Communications* **166**, p. 1 (2013). → pp. 18, 69, 128, and 132.

[42] E. Janik, J. Sadowski, P. Dłużewski, S. Kret, L. T. Baczewski, A. Petroutchik, E. Lusakowska, J. Wrobel, W. Zaleszczyk, G. Karczewski, T. Wojtowicz, and A. Presz, "ZnTe nanowires grown on GaAs (100) substrates by molecular beam epitaxy", *Applied Physics Letters* **89**, 13 (2006). → pp. 18 and 38.

[43] T. Wojtowicz, E. Janik, W. Zaleszczyk, J. Sadowski, G. Karczewski, P. Dłużewski, S. Kret, W. Szuszkiewicz, E. Dynowska, J. Domagala, M. Aleszkiewicz, L. T. Baczewski, A. Petroutchik, A. Presz, W. Pacuski, A. Golnik, P. Kossacki, J. F. Morhange, H. Kirmse, W. Neumann, and W. Caliebe, "MBE Growth and Properties of ZnTe- and CdTe-Based Nanowires", *Journal of the Korean Physical Society* **53**, 5, p. 3055 (2008). → pp. 18 and 38.

[44] P. Dłużewski, E. Janik, S. Kret, W. Zaleszczyk, D. Tang, G. Karczewski, and T. Wojtowicz, "TEM characterization of MBE grown CdTe/ZnTe axial nanowires", *Journal of Microscopy* **237**, 3, p. 337 (2010). → p. 18.

[45] J. Hajer, "Proximity Induced Superconductivity and Magnetoconductance Oscillations in CdTe–HgTe Core–Shell Nanowires", Master's thesis, Julius-Maximilians-Universität Würzburg, 2016. → pp. 19, 83, 89, 105, 127, and 142.

[46] D. Car, J. Wang, M. A. Verheijen, E. P. A. M. Bakkers, and S. R. Plissard, "Rationally designed single-crystalline nanowire networks", *Advanced Materials* **26**, 28, p. 4875 (2014). → p. 19.

[47] O. Madelung, editor, "Semiconductors - Basic Data", Springer, 1996. → pp. 20, 35, 41, 42, and 54.

[48] R. Schlereth, J. Hajer, L. Fürst, S. Schreyeck, H. Buhmann, and L. W. Molenkamp, "Band edge thermometry for the MBE growth of (Hg, Cd) Te-based materials", *Journal of Crystal Growth* **537C**, p. 125602 (2020). → pp. 23, 25, 29, and 147.

[49] R. Schlereth, "New techniques and improvements in the MBE growth of Hg-containing narrow gap semiconductors", PhD thesis, Julius-Maximilians-Universität Würzburg, 2020. → p. 25.

[50] Y. P. Varshni, "Temperature dependence of the energy gap in semiconductors", *Physica* **34**, 1, p. 149 (1967). → p. 25.

[51] M. B. Denton, W. L. Johnson, and M. D. Sirkis, "Method of wafer band-edge measurement using transmission spectroscopy and a process for controlling the temperature uniformity of a wafer", patent number US 6,891,124 B2, (2005). → p. 26.

[52] L. Peters, L. Phaneuf, L. W. Kapitan, and W. M. Theis, "Noncontact doping level determination in GaAs using photoreflectance spectroscopy", *Journal of Applied Physics* **62**, 11, p. 4558 (1987). → p. 26.

[53] W. E. Hoke, D. Barlett, T. D. Kennedy, B. Wissman, and J. J. Mosca, "Short wavelength band edge thermometry during molecular beam epitaxial growth of GaN on SiC substrates and detected adatom self-heating effects", *Journal of Vacuum Science & Technology B* **28**, 3, p. C3F5 (2010). → p. 26.

[54] R. Zhao, M. J. Cich, P. Specht, and E. R. Weber, "In situ diffuse reflectance spectroscopy investigation of low-temperature-grown GaAs", *Applied Physics Letters* **80**, 12, p. 2060 (2002). → p. 26.

[55] R. Gu, C. Shen, Y. Guo, W. Wang, X. Fu, and L. Chen, "In situ thickness and temperature measurements of CdTe grown by molecular beam epitaxy on GaAs substrate", *Journal of Vacuum Science & Technology B* **30**, 4, p. 041203 (2012). → p. 26.

[56] V. G. Dubrovskii, N. V. Sibirev, G. E. Cirlin, I. P. Soshnikov, W. H. Chen, R. Larde, E. Cadel, P. Pareige, T. Xu, B. Grandidier, J.-P. Nys, D. Stievenard, M. Moewe, L. C. Chuang, and C. Chang-Hasnain, "Gibbs-Thomson and diffusion-induced contributions to the growth rate of Si, InP, and GaAs nanowires", *Physical Review B* **79**, p. 205316 (2009). → p. 31.

[57] H. Küpers, R. B. Lewis, A. Tahraoui, M. Matalla, O. Krüger, F. Bastiman, H. Riechert, and L. Geelhaar, "Diameter evolution of selective area grown Ga-assisted GaAs nanowires", *Nano Research* **11**, 5, p. 2885 (2018). → p. 32.

[58] R. Bakke, "Structural characterization of CdTe semiconductor nanowires", Master's project, NTNU Trondheim, 2020. → p. 33.

[59] K. Tomioka, T. Tanaka, S. Hara, K. Hiruma, and T. Fukui, "III–V nanowires on Si substrate: selective-area growth and device applications", *IEEE Journal of Selected Topics in Quantum Electronics* **17**, 4, p. 1112 (2010). → p. 35.

[60] J. Hajer, W. Mantei, M. Kessel, C. Brüne, S. Wenner, A. T. J. van Helvoort, H. Buhmann, and L. W. Molenkamp, "Selective area grown ZnTe nanowires as the basis for quasi-one-dimensional CdTe-HgTe multishell heterostructures", *Physical Review Materials* **4**, 6, p. 066001 (2020), . → pp. 37 and 147.

[61] B. Mandl, A. W. Dey, J. Stangl, M. Cantoro, L.-E. Wernersson, G. Bauer, L. Samuelson, K. Deppert, and

C. Thelander, "Self-seeded, position-controlled InAs nanowire growth on Si: A growth parameter study", *Journal of Crystal Growth* **334**, 1, p. 51 (2011). → p. 38.

[62] P. Mohan, J. Motohisa, and T. Fukui, "Controlled growth of highly uniform, axial/radial direction-defined, individually addressable InP nanowire arrays", *Nanotechnology* **16**, 12, p. 2903 (2005). → p. 38.

[63] J. Noborisaka, J. Motohisa, and T. Fukui, "Catalyst-free growth of GaAs nanowires by selective-area metalorganic vapor-phase epitaxy", *Applied Physics Letters* **86**, 21, p. 213102 (2005). → p. 38.

[64] P. Wojnar, J. Płachta, W. Zaleszczyk, S. Kret, A. M. Sanchez, R. Rudniewski, K. Raczkowska, M. Szymura, G. Karczewski, L. T. Baczewski, A. Pietruczik, T. Wojtowicz, and J. Kossut, "Coexistence of optically active radial and axial CdTe insertions in single ZnTe nanowire", *Nanoscale* **8**, 10, p. 5720 (2016). → p. 38.

[65] H. Okamoto and T. B. Massalski, "The Au–Zn (gold–zinc) system", *Bulletin of Alloy Phase Diagrams* **10**, 1, p. 59 (1989). → pp. 39 and 49.

[66] H. Okamoto and T. B. Massalski, "The Au–Te (gold–tellurium) system", *Bulletin of Alloy Phase Diagrams* **5**, 2, p. 172 (1984). → pp. 39 and 49.

[67] R. P. Elliott and F. A. Shunk, "The Au–Ga (gold–gallium) system", *Bulletin of Alloy Phase Diagrams* **2**, 3, p. 356 (1981). → pp. 39 and 49.

[68] M. Bafleur, A. Munoz-Yague, and A. Rocher, "Microtwinning and growth defects in GaAs MBE layers", *Journal of Crystal Growth* **59**, 3, p. 531 (1982). → p. 42.

[69] P. Madras, E. Dailey, and J. Drucker, "Kinetically induced kinking of vapor- liquid- solid grown epitaxial Si nanowires", *Nano Letters* **9**, 11, p. 3826 (2009). → p. 46.

[70] S. Hertenberger, D. Rudolph, M. Bichler, J. J. Finley, G. Abstreiter, and G. Koblmüller, "Growth kinetics in position-controlled and catalyst-free InAs nanowire arrays on Si (111) grown by selective area molecular beam epitaxy", *Journal of Applied Physics* **108**, 11, p. 114316 (2010). → p. 47.

[71] E. Janik, P. Dłużewski, S. Kret, A. Presz, H. Kirmse, W. Neumann, W. Zaleszczyk, L. T. Baczewski, A. Petroutchik, E. Dynowska, J. Sadowski, W. Caliebe, G. Karczewski, and T. Wojtowicz, "Catalytic growth of ZnTe nanowires by molecular

beam epitaxy: structural studies", *Nanotechnology* **18**, 47, p. 475606 (2007). → p. 50.

[72] P. Caroff, J. Bolinsson, and J. Johansson, "Crystal Phases in III–V Nanowires: From Random Toward Engineered Polytypism", *IEEE Journal of Selected Topics in Quantum Electronics* **17**, 4, p. 829 (2011). → p. 50.

[73] S. Oehling, M. Ehinger, W. Spahn, A. Waag, C. R. Becker, and G. Landwehr, "Mechanisms of molecular beam epitaxial growth of (001) HgTe", *Journal of Applied Physics* **79**, 2, p. 748 (1996). → pp. 61 and 63.

[74] G. Ehrlich and F. G. Hudda, "Atomic view of surface self-diffusion: tungsten on tungsten", *The Journal of Chemical Physics* **44**, 3, p. 1039 (1966). → p. 62.

[75] R. L. Schwoebel and E. J. Shipsey, "Step motion on crystal surfaces", *Journal of Applied Physics* **37**, 10, p. 3682 (1966). → p. 62.

[76] M. J. Hÿtch, E. Snoeck, and R. Kilaas, "Quantitative measurement of displacement and strain fields from HREM micrographs", *Ultramicroscopy* **74**, 3, p. 131 (1998). → p. 65.

[77] H. Peng, K. Lai, D. Kong, S. Meister, Y. Chen, X.-L. Qi, S.-C. Zhang, Z.-X. Shen, and Y. Cui, "Aharonov-Bohm interference in topological insulator nanoribbons", *Nature Materials* **9**, 3, p. 225 (2010). → p. 69.

[78] P. Leubner, L. Lunczer, C. Brüne, H. Buhmann, and L. W. Molenkamp, "Strain engineering of the band gap of HgTe quantum wells using superlattice virtual substrates", *Physical Review Letters* **117**, 8, p. 086403 (2016). → p. 69.

[79] X. Dai, T. L. Hughes, X.-L. Qi, Z. Fang, and S.-C. Zhang, "Helical edge and surface states in HgTe quantum wells and bulk insulators", *Physical Review B* **77**, 12, p. 125319 (2008). → p. 69.

[80] L. Fu and C. L. Kane, "Topological insulators with inversion symmetry", *Physical Review B* **76**, 4, p. 045302 (2007). → pp. 69, 128, and 132.

[81] B. A. Bernevig, T. L. Hughes, and S.-C. Zhang, "Quantum spin Hall effect and topological phase transition in HgTe quantum wells", *Science* **314**, 5806, p. 1757 (2006). → pp. 75 and 76.

[82] L. Fu and C. L. Kane, "Superconducting proximity effect and Majorana fermions at the surface of a topological insulator", *Physical Review Letters* **100**, 9, p. 096407 (2008). → pp. 75, 101, 103, and 115.

[83] J. H. Bardarson, P. W. Brouwer, and J. E. Moore, "Aharonov-Bohm oscillations in disordered topological insulator nanowires", *Physical Review Letters* **105**, 15, p. 156803 (2010). → p. 76.

[84] M. V. Berry, "Quantal phase factors accompanying adiabatic changes", *Proceedings of the Royal Society of London. Series A, Mathematical and Physical Sciences* **392**, 1802, p. 45 (1984). → p. 77.

[85] Y. Zhang, Y. Ran, and A. Vishwanath, "topological insulators in three dimensions from spontaneous symmetry breaking", *Physical Review B* **79**, 24, p. 245331 (2009). → p. 77.

[86] Y. Aharonov and D. Bohm, "Significance of Electromagnetic Potentials in the Quantum Theory", *Physical Review* **115**, p. 485 (1959). → pp. 78 and 86.

[87] B. L. Altshuler, A. G. Aronov, and B. Z. Spivak, "The Aaronov-Bohm effect in disordered conductors", *Pis'ma v Zhurnal Èksperimental'noi i Teoreticheskoi Fiziki* **33**, 2, p. 101 (1981), [*JETP Letters* **33**, 2 (1981)]. → pp. 79, 86, and 87.

[88] J. Brehm, "Nanometer Lithographie an Quasi-1D HgTe Heterostrukturen", Master's thesis, Julius-Maximilians-Universität Würzburg, 2014. → p. 81.

[89] H. A. Pohl, "The motion and precipitation of suspensoids in divergent electric fields", *Journal of Applied Physics* **22**, 7, p. 869 (1951). → p. 81.

[90] J. Hajer, "II-VI Nanodrähte – Herstellung durch VLS-MBE und Manipulation mittels Dielektrophorese", Bachelor's thesis, Julius-Maximilians-Universität Würzburg, 2014. → p. 81.

[91] S. Krüger, "Radiale HgTe-CdTe Nanodrähte – Manipulation und Charakterisierung", Bachelor's thesis, Julius-Maximilians-Universität Würzburg, 2015. → p. 81.

[92] V. Lordi, P. Erhart, and D. Åberg, "Charge carrier scattering by defects in semiconductors", *Physical Review B* **81**, 23, p. 235204 (2010). → p. 86.

[93] P. A. Lee and A. D. Stone, "Universal conductance fluctuations in metals", *Physical Review Letters* **55**, p. 1622 (1985). → pp. 86 and 87.

[94] S. Washburn and R. A. Webb, "Aharonov-Bohm effect in normal metal quantum coherence and transport", *Advances in Physics* **35**, 4, p. 375 (1986). → pp. 86, 87, 125, 129, and 133.

[95] T. Ihn, "Oscillations in the ribbons", *Nature Materials* **9**, 3, p. 187 (2010). → p. 87.

[96] M. T. Elm, P. Uredat, J. Binder, L. Ostheim, M. Schäfer, P. Hille, J. Müssener, J. Schörmann, M. Eickhoff, and P. J. Klar, "Doping-induced universal conductance fluctuations in GaN nanowires", *Nano Letters* **15**, 12, p. 7822 (2015). → p. 88.

[97] G. D. Wilk, R. M. Wallace, and J. M. Anthony, "High-κ gate dielectrics: Current status and materials properties considerations", *Journal of Applied Physics* **89**, 10, p. 5243 (2001). → p. 93.

[98] W. Chen, Q.-Q. Sun, M. Xu, S.-J. Ding, D. W. Zhang, and L.-K. Wang, "Atomic layer deposition of hafnium oxide from tetrakis (ethylmethylamino) hafnium and water precursors", *The Journal of Physical Chemistry C* **111**, 17, p. 6495 (2007). → p. 94.

[99] A. Inhofer, S. Tchoumakov, B. A. Assaf, G. Feve, J.-M. Berroir, V. Jouffrey, D. Carpentier, M. O. Goerbig, B. Plaçais, K. Bendias, D. M. Mahler, E. Bocquillon, R. Schlereth, C. Brüne, H. Buhmann, and L. W. Molenkamp, "Observation of Volkov-Pankratov states in topological HgTe heterojunctions using high-frequency compressibility", *Physical Review B* **96**, 19, p. 195104 (2017). → p. 94.

[100] L.-X. Wang, C.-Z. Li, D.-P. Yu, and Z.-M. Liao, "Aharonov–Bohm oscillations in Dirac semimetal Cd_3As_2 nanowires", *Nature Communications* **7**, p. 10769 (2016). → p. 98.

[101] Ö. Gül, N. Demarina, C. Blömers, T. Rieger, H. Lüth, M. I. Lepsa, D. Grützmacher, and T. Schäpers, "Flux periodic magnetoconductance oscillations in GaAs/InAs core/shell nanowires", *Physical Review B* **89**, 4, p. 045417 (2014). → p. 98.

[102] R. M. Lutchyn, J. D. Sau, and S. D. Sarma, "Majorana fermions and a topological phase transition in semiconductor-superconductor heterostructures", *Physical Review Letters* **105**, 7, p. 077001 (2010). → pp. 101 and 126.

[103] T.-P. Choy, J. M. Edge, A. R. Akhmerov, and C. W. J. Beenakker, "Majorana fermions emerging from magnetic nanoparticles on a superconductor without spin-orbit coupling", *Physical Review B* **84**, 19, p. 195442 (2011). → p. 101.

[104] J. Hajer, M. Kessel, C. Brüne, M. P. Stehno, H. Buhmann, and L. W. Molenkamp, "Proximity-Induced Superconductivity in CdTe–HgTe Core–Shell Nanowires", *Nano Letters* **19**, 6, p. 4078 (2019). → pp. 101 and 147.

[105] D. van Delft and P. Kes, "The discovery of superconductivity", *Physics Today* **63**, 9, p. 38 (2010). → p. 102.

[106] W. Meissner and R. Ochsenfeld, "Ein neuer Effekt bei Eintritt der Supraleitfähigkeit", *Naturwissenschaften* **21**, 44, p. 787 (1933). → p. 102.

[107] J. Bardeen, L. N. Cooper, and J. R. Schrieffer, "Microscopic theory of superconductivity", *Physical Review* **106**, 1, p. 162 (1957). → pp. 102 and 104.

[108] J. Bardeen, L. N. Cooper, and J. R. Schrieffer, "Theory of superconductivity", *Physical Review* **108**, 5, p. 1175 (1957). → p. 102.

[109] R. Holm and W. Meissner, "Messungen mit Hilfe von flüssigem Helium. XIII", *Zeitschrift für Physik* **74**, 11-12, p. 715 (1932). → p. 103.

[110] B. D. Josephson, "Possible new effects in superconductive tunnelling", *Physics Letters* **1**, 7, p. 251 (1962). → pp. 103 and 118.

[111] M. Sato and Y. Ando, "Topological superconductors: a review", *Reports on Progress in Physics* **80**, 7, p. 076501 (2017). → p. 103.

[112] C. Reale, "Thickness and temperature dependence of the critical magnetic field of thin superconducting films of the aluminium group metals", *Acta Physica Academiae Scientiarum Hungaricae* **37**, 1-2, p. 53 (1974). → p. 103.

[113] H. Courtois, M. Meschke, J. T. Peltonen, and J. P. Pekola, "Origin of hysteresis in a proximity Josephson junction", *Physical Review Letters* **101**, 6, p. 067002 (2008). → pp. 106 and 114.

[114] D. S. Antonenko and M. A. Skvortsov, "Quantum decay of the supercurrent and intrinsic capacitance of Josephson junctions beyond the tunnel limit", *Physical Review B* **21**, p. 214513 (2015). → p. 106.

[115] P. Dubos, H. Courtois, B. Pannetier, F. K. Wilhelm, A. D. Zaikin, and G. Schön, "Josephson critical current in a long mesoscopic SNS junction", *Physical Review B* **63**, 6, p. 064502 (2001). → p. 106.

[116] M. Octavio, M. Tinkham, G. E. Blonder, and T. M. Klapwijk, "Subharmonic energy-gap structure in superconducting constrictions", *Physical Review B* **27**, 11, p. 6739 (1983). → p. 107.

[117] G. Niebler, G. Cuniberti, and T. Novotnỳ, "Analytical calculation of the excess current in the Octavio–Tinkham–Blonder–Klapwijk theory", *Superconductor Science and Technology* **22**, 8, p. 085016 (2009). → p. 107.

[118] T. M. Klapwijk, G. E. Blonder, and M. Tinkham, "Explanation of subharmonic energy gap structure in superconducting contacts", *Physica B+C* **109**, p. 1657 (1982). → p. 108.

[119] K. Flensberg, J. B. Hansen, and M. Octavio, "Subharmonic energy-gap structure in superconducting weak links", *Physical Review B* **38**, 13, p. 8707 (1988). → p. 109.

[120] J. C. Cuevas, J. Hammer, J. Kopu, J. K. Viljas, and M. Eschrig, "Proximity effect and multiple Andreev reflections in diffusive superconductor–normal-metal–superconductor junctions", *Physical Review B* **73**, p. 184505 (2006). → pp. 110 and 111.

[121] J. Xiang, A. Vidan, M. Tinkham, R. M. Westervelt, and C. M. Lieber, "Ge/Si nanowire mesoscopic Josephson junctions", *Nature Nanotechnology* **1**, 3, p. 208 (2006). → p. 110.

[122] M. Kjærgaard, H. J. Suominen, M. P. Nowak, A. R. Akhmerov, J. Shabani, C. J. Palmstrøm, F. Nichele, and C. M. Marcus, "Transparent Semiconductor-Superconductor Interface and Induced Gap in an Epitaxial Heterostructure Josephson Junction", *Physical Review Applied* **7**, 3, p. 034029 (2017). → p. 110.

[123] Douglass Jr., D. H., "Direct Experimental Measurement of the Magnetic Field Dependence of the Superconducting Energy Gap of Aluminum", *Physical Review Letters* **7**, 1, p. 14 (1961). → p. 112.

[124] B. Mühlschlegel, "Die thermodynamischen Funktionen des Supraleiters", *Zeitschrift für Physik* **155**, 3, p. 313 (1959). → pp. 113, 114, and 115.

[125] H.-J. Kwon, V. M. Yakovenko, and K. Sengupta, "Fractional ac Josephson effect in unconventional superconductors", *Low Temperature Physics* **30**, 7, p. 613 (2004). → pp. 114 and 117.

[126] I. O. Kulik and A. N. Omel'yanchuk, "Properties of superconducting microbridges in the pure limit", *Soviet Journal of Low Temperature Physics (Engl. Transl.)* **3**, 7 (1977). → p. 116.

[127] J. Wiedenmann, E. Bocquillon, R. S. Deacon, S. Hartinger, O. Herrmann, T. M. Klapwijk, L. Maier, C. Ames, C. Brüne, C. Gould, A. Oiwa, K. Ishibashi, S. Tarucha, H. Buhmann, and L. W. Molenkamp, "4 π-periodic Josephson supercurrent in HgTe-based topological Josephson junctions", *Nature Communications* **7**, 1, p. 1 (2016). → pp. 117, 123, and 130.

[128] S. Shapiro, "Josephson currents in superconducting tunneling: The effect of microwaves and other observations", *Physical Review Letters* **11**, 2, p. 80 (1963). → p. 118.

[129] K. K. Likharev, "Dynamics of Josephson junctions and circuits", Gordon and Breach science publishers, 1986. → p. 118.

[130] M. Tinkham, "Introduction to superconductivity", Courier Corporation, 1996. → p. 118.

[131] F. Dominguez, F. Hassler, and G. Platero, "Dynamical detection of Majorana fermions in current-biased nanowires", *Physical Review B* **86**, 14, p. 140503 (2012). → pp. 118, 122, 129, and 134.

[132] P. Dubos, H. Courtois, O. Buisson, and B. Pannetier, "Coherent low-energy charge transport in a diffusive SNS junction", *Physical Review Letters* **87**, 20, p. 206801 (2001). → p. 118.

[133] M. Chauvin, P. Vom Stein, H. Pothier, P. Joyez, M. E. Huber, D. Esteve, and C. Urbina, "Superconducting atomic contacts under microwave irradiation", *Physical Review Letters* **97**, 6, p. 067006 (2006). → p. 120.

[134] B. Raes, N. Tubsrinuan, R. Sreedhar, D. S. Guala, R. Panghotra, H. Dausy, C. C. de Souza Silva, and J. Van de Vondel, "Fractional Shapiro steps in resistively shunted Josephson junctions as a fingerprint of a skewed current-phase relationship", *Physical Review B* **102**, 5, p. 054507 (2020). → p. 120.

[135] A. De Cecco, K. Le Calvez, B. Sacépé, C. B. Winkelmann, and H. Courtois, "Interplay between electron overheating and ac Josephson effect", *Physical Review B* **93**, 18, p. 180505 (2016). → p. 121.

[136] M. C. Dartiailh, J. J. Cuozzo, B. H. Elfeky, W. Mayer, J. Yuan, K. S. Wickramasinghe, E. Rossi, and J. Shabani, "Missing Shapiro steps in topologically trivial Josephson junction on InAs quantum well", *Nature Communications* **12**, 1, p. 1 (2021). → pp. 122 and 130.

[137] J. Picó-Cortés, F. Domínguez, and G. Platero, "Signatures of a 4 π-periodic supercurrent in the voltage response of capacitively shunted topological Josephson junctions", *Physical Review B* **96**, 12, p. 125438 (2017). → p. 122.

[138] J. Wiedenmann, "Induced topological superconductivity in HgTe based nanostructures", PhD thesis, Julius-Maximilians-Universität Würzburg, 2018. → pp. 122 and 134.

[139] A.-Q. Wang, C.-Z. Li, C. Li, Z.-M. Liao, A. Brinkman, and D.-P. Yu, "4 π-Periodic Supercurrent from Surface States in Cd_3As_2 Nanowire-Based Josephson Junctions", *Physical Review Letters* **121**, 23, p. 237701 (2018). → p. 122.

[140] Y. Oreg, G. Refael, and F. von Oppen, "Helical liquids and Majorana bound states in quantum wires", *Physical Review Letters* **105**, 17, p. 177002 (2010). → p. 126.

[141] V. Mourik, K. Zuo, S. M. Frolov, S. R. Plissard, E. P. A. M. Bakkers, and L. P. Kouwenhoven, "Signatures of Majorana fermions in hybrid superconductor-semiconductor nanowire devices", *Science* **336**, 6084, p. 1003 (2012). → p. 126.

[142] M. Veldhorst, M. Snelder, M. Hoek, T. Gang, V. K. Guduru, X. L. Wang, U. Zeitler, W. G. van der Wiel, A. A. Golubov, H. Hilgenkamp, and A. Brinkman, "Josephson supercurrent through a topological insulator surface state", *Nature materials* **11**, 5, p. 417 (2012). → p. 126.

[143] M. Hays, G. De Lange, K. Serniak, D. J. van Woerkom, D. Bouman, P. Krogstrup, J. Nygård, A. Geresdi, and M. H. Devoret, "Direct microwave measurement of Andreev-bound-state dynamics in a semiconductor-nanowire Josephson junction", *Physical Review Letters* **121**, 4, p. 047001 (2018). → p. 130.

Acknowledgments

This thesis would not have been possible without all the people who contributed directly or indirectly to the success of this thesis:

Thank you, Laurens, for giving me the opportunity of a PhD position at your chair. I really enjoyed the possibilities a lab with such a broad set of excellent equipment and knowhow can offer.

Hartmut, thank you a lot for supervising my thesis! I really appreciate the guidance, but also the freedom in research you gave me.

Prof. Reinert, I appreciate you being the second referee of this thesis.

Max, thank you for teaching me so much about all different aspects regarding nanowires throughout my masters project, from your expertise I profited hugely during my PhD.

Special thanks goes to the entire MBE team for the warm and collegial atmosphere. I would especially like to mention Lena, Lukas, Steffen, Grzegorz, Raimund, Boby and Alwyn – thank you for the constant support, plenty of fruitful discussions, the mutual help with the MBE chamber openings, and the relaxing coffee breaks and chats in between. A huge thank you goes to Luke for the development of our excellent new MBE control software that made my hours-long growth runs so much more enjoyable. Carmen and Petra, thank you for the countless molyblocks you prepared, and especially for all the organization and work in the "background" that is all to easily overseen or taken for granted. Martin, thank you for the outstanding job you did in order to keep the entire MBE cluster running so smoothly. I am also really grateful for the time you always readily took for sharing your expertise on the repair and maintenance of the MBE chambers.

I also thank the cleanroom and litho team for all the support. Volkmar, thanks a lot for keeping the entire cleanroom running, for building and constantly improving all the different processing chambers, for the super-quick repairs, and for your profound answers to all different technical questions. Tanja and Joe, I appreciate your organizational work in the yellowroom, as well as your valuable advice and suggestions on how to debug and optimize my sample fabrication. And Simon, thank you for all the time and effort you put into the building and perfecting of the low-temperature ALD.

Further, I thank all the colleagues who supported me with my transport measurements. In particular, I would like to mention Budi, Saquib and Mohamed; I really appreciate that you always found time to explain me details in the operation of the various cryostats, as well as your helping hands with troubleshooting issues with the measurement setups. Jonas and Michael, thank you for valuable discussions on the Aharonov–Bohm effect. Wouter, thank you for your great $\vec{k} \cdot \vec{p}$ band structure simulation software. Martin, I appreciate a lot the effort you took to support me setting up the superconductivity measurements, and for many discussions on the interpretation of the results we got. Jonas, Sandeep and Amandeep, thank you as well for your help with the operation of the superconductivity dilution fridges. In this context I would also like to thank Cornelius and Robert for the steady supply with liquid helium and nitrogen, as well as the electrical and mechanical workshop for their kind help and quick repairs.

Then, I thank the TEM team at the NTNU in Trondheim, Norway. Ton, thank you for your support getting this collaboration started, and for your advice and feedback. Sigurd, you did a wonderful job with the FIB and the imaging. I really enjoyed joining you at the TEM for two of the imaging sessions. And Ragna, thank you a lot for your detailed structural analysis of the nanowires during your masters project. The TEM investigation of the nanowire cross-sections recieved funding from the European Union Horizon 2020 research programme (grant No. 823717 – ESTEEM3), which I appreciate.

For their support with all sorts of organizational matters I thank Angelika, Toby and Charles. Claus, Madder and Luke, thank you for the IT administration. In this context, I would also like to acknowledge the financial support of the Deutsche Forschungsgemeinschaft (SPP 1666 and SFB 1170) and the Elitenetzwerk Bayern (IDK TOIS).

During my time at EP3, I was supported by several bachelor and master students: Willi, it was a great pleasure to start my PhD right away with you. I really appreciate your great motivation and effort on the search for a possible way to achieve selective area growth. Marten, thank you a lot for your help with the development and improvement of the nanowire lithography. And Czcibor, I am really glad that you decided to join me on the nanowire project although it was not clear in the beginning for how long I would be there to support you. I very much enjoyed working with you on the optimization of growth and the magnetotransport, as well as our countless hours of discussions. I am sure that with you the project is in best hands!

Finally, a big thank you goes to my office mates and all other colleagues at EP3, as well as to my friends, family and my girlfriend, who supported me during my PhD and contributed to this wonderful time!